UNIVERSITY OF MISKOLC
FACULTY OF MECHANICAL ENGINEERING AND INFORMATICS

COMPLEX EVALUATION OF RESISTANCE SPOT WELDING TECHNOLOGIES FOR DUAL-PHASE AND MARTENSITIC STEELS

PHD THESES

Prepared by

Sahm alden Anis Mohammad Abd al al
Civil Engineering (BSc),
Infrastructure Engineering (MSc)

ISTVÁN SÁLYI DOCTORAL SCHOOL OF MECHANICAL ENGINEERING SCIENCES
ENGINEERING MATERIALS SCIENCE, PRODUCTION SYSTEMS, AND PROCESSES
MATERIALS ENGINEERING AND MECHANICAL TECHNOLOGY

Head of Doctoral School

Prof. Dr. Gabriella Vadászné Bognár
DSc, Full Professor

Head of Topic Group

Prof. Dr. János Lukács
CSc, PhD, Full Professor

Scientific Supervisor

Dr. Ákos Meilinger
PhD, Associate Professor

Scientific Cosupervisor

Prof. Dr. Marcell Gáspár
PhD, Full Professor

Miskolc
2025

SUPERVISOR'S RECOMMENDATIONS

Abd Al Al Sahm Alden Anis Mohammad was born in 1987 in Amman, Jordan. He graduated in Highway and Bridge Engineering (Civil Engineering) BSc at Al-Balqa Applied University (Jordan) in 2011. During his studies he passed academic courses in the field of finite element analysis (FEA), construction software, management training and ASME training in welding inspection. After graduation he worked three years in the industry at Global Smart Co. (Amman, Jordan), and later 4 years in Amsterdam Contracting Co. (Amsterdam, Netherlands) in the field of fabrication and welding of steel structures. Then he moved to Hungary and graduated in Infrastructure Engineering MSc at Széchenyi István University with excellent grade (4.85/5). He started his PhD in 2021 within the Stipendium Hungaricum Scholarship Programme at the University of Miskolc in the field of Complex Evaluation of Resistance Spot Welding Technologies for Dual-Phase and Martensitic Steels. He joined to a prospective research field of the Institute of Material Science and Technology in which the organization has decades of experience.

His previous studies mostly focused on the design of different steel structures; however, he gained useful experiences in the field of production, especially in welding, during his industrial experience as a fabrication engineer and quality controller. Therefore, it was decided to develop his skills in the field of welding, which determined his course selection strategy in the doctoral school. Besides the conventional learning, he did an extensive international literature review about the resistance spot welding of advanced high strength steels (dual-phase steels, martensitic steels) including the examination of spot-welded joints. In 2023 he successfully passed the complex exam with 100% evaluation for the theoretical part and 100% evaluation for the dissertation part. He has 18 publications including six journal papers from which four are international and one is Q1 ranked having impact factor. He was the initiator of more publications, and he prepared the manuscripts with a high degree of independence.

Besides his PhD research he has joined to the life of the Institute as a full value colleague. He performed outstanding work in the establishment of the Advanced Materials and Arc Welding Processes (AMAP) Laboratory within the cooperation of the Munich University of Applied Sciences and our Institute. He designed the layout of the laboratory and participated in the instalment of the equipment. He has been actively contributing to more international and national projects in the field of education and research. Within the D-EWI Erasmus+ project he developed e-learning educational materials for the European Welding Inspector (EWI) postgraduate training, in the HINTS Erasmus+ project he participated in the project planning. He participated in the Flumen 2 Gas Transmission Stream project in the field of hydrogen resistant sealings and gaskets of the planned mobile gas transmission station. Furthermore, he has been working in course material development in the Centre of Vocational Excellence in Welding and Non-Destructive Testing (COVE-WENDT) Erasmus project about digitalization and green welding industry.

He actively participates in the professional public life as the member of the Jordan Green Building Council, Jordanian Constructions Contractors Association, American Society of Mechanical Engineering (ASME) and the Hungarian Welding Society (MAHEG). He has good language skills and computer skills. He has experience in multitasking and problem solving. Furthermore, his leadership and coordination skills can be highlighted

Based on his previous four-year persistent scientific activity he is highly recommended for obtaining the PhD degree.

Miskolc, 11th March 2025

Dr. Ákos Meilinger supervisor	Prof. Dr. Marcell Gáspár co-supervisor

LIST OF SYMBOLS AND ABBREVIATIONS

GREEK LETTERS

ΔL	Load range	kN
α	Ferrite	N/A
γ	Austenite	N/A
λ	Thermal conductivity	W/mm·K
α'	Martensite	N/A
θ	Measured angle	Degree
τ	Shear stress	MPa
σ	Tensile stress	MPa
∅	Diameter	mm
ρ	Electrical resistivity	Ω·m
∡	Angle	Degree
Δσ	Stress range	MPa

LATIN LETTERS

A	Elongation	%
AC	Alternating current	A
AHSS	Advanced high-strength steels	N/A
AWS	American welding society	N/A
BM	Base material	N/A
BIW	Body in white	
CAD	Computer-aided design	N/A
CCT	Continuous cooling transformation	N/A
Ceq	Carbon equivalent number	%
CGHAZ	Coarse-grained heat-affected zone	N/A
CuCrZr	Copper chromium zirconium	N/A
CTS	Cross-tension strength	kN
D	Diameter	mm
D90%	Effective grain size at 90% in the cumulative size distribution	µm
DC	Direct current	A
DP	Dual-phase	N/A
dp	Partial plug diameter	mm
DPF	Double-sided pullout failure	N/A
DPW	2-pulse weld	N/A

EBSD	Electron backscatter diffraction	N/A
ECD	Equivalent circular diameter	µm
EDX	Energy-dispersive X-ray diffraction	N/A
FEA	Finite element analysis	N/A
FEM	Finite element modelling	N/A
FESEM	Field-emission scanning electron microscope	N/A
FGHAZ	Fine-grained heat-affected zone	N/A
FM	Fresh martensite	N/A
FTM	Fully tempered martensite	N/A
FZ	Fusion zone	N/A
FZ2	Inner fusion zone	N/A
HAGBs	High-angle grain boundaries	Degree
HAZ	Heat-affected zone	N/A
HCF	High cycle fatigue	Cycle
HV	Vickers Hardness	-
ICHAZ	Intercritical heat-affected zone	N/A
IF	Interfacial failure	N/A
IPF	Inverse pole figure	N/A
IQ	Image quality	N/A
Iw	Welding current	A
LAGBs	Low-angle grain boundaries	Degree
LCF	Low-cycle fatigue	Cycle
L-D	Load-displacement	N/A
L-N	Load-Number of cycle	N/A
LOM	Light optical microscopy	N/A
Mf	Martensite finish	°C
Ms	Martensite start	°C
MS	Martensitic steel	N/A
MVF	Martensite volume fraction	%
OM	Optical microscopy	N/A
PAGs	Prior austenite grains	µm
PF	Pullout failure	N/A
PIF	Partial interfacial failure	N/A
P_{max}	Peak load	kN
PTM	Partially tempered martensite	N/A
Q&P	Quenching & partitioning	N/A
r	Radius	mm
R&D	Research and development	N/A
Rex-zone	Recrystallized zone or outer fusion zone	N/A
Rm	Tensile strength	MPa
Rp0.2	Yield strength	MPa
RSW	Resistance spot welding	N/A
SCHAZ	Subcritical heat-affected zone	N/A
SD	Standard deviation	N/A

SDc	Coefficient of standard deviation	N/A
SEM	Scanning electron microscopy	N/A
SPW	Single pulse weld	N/A
t	Sheet thickness	mm
$t_{8/5}$	Cooling time from 800°C to 500°C	ms
TBF	TRIP-aided bainitic ferrite	N/A
TC	Thermocouple	N/A
TM	Tempered martensite	N/A
TRIP	Transformation-induced plasticity	N/A
TSS	Tensile shear strength	kN
T-S	Tensile-shear test	N/A
TTT	Time-temperature-transformation	N/A
TWIP	Twinning-induced plasticity	N/A
UCHAZ	Upper critical heat-affected zone	N/A
UHSS	Ultra-high strength steel	N/A
UTS	Ultimate tensile strength	Mpa
W	Width of sheet	mm
W_{max}	Failure energy	N/A
		J

SUBSCRIPTS

Ang. mis.	angular misalignment	Degree
Avg.	Average	N/A
Dev.	Deviation	N/A
Disp.	Displacement	mm
Eff.	Effective	N/A
Max.	Maximum	N/A
Par. mis.	Parallel misalignment	mm
SL. disp.	Sliding line displacement	mm
SW. disp.	Spot-weld displacement	mm

1. INTRODUCTION

Europe's automotive industry has embraced Advanced High-Strength Steels (AHSS) for several compelling reasons. The stringent fuel efficiency and emissions regulations in Europe have driven automakers to seek lightweight materials that can significantly reduce vehicle weight [1][2]. AHSS combines higher strength, good ductility, and excellent energy absorption [3][4]. By using AHSS, manufacturers can achieve weight reductions of up to 35-40% compared to traditional steel, resulting in improved fuel economy and lower greenhouse gas emissions over a vehicle's lifespan [1]. Additionally, Europe's rigorous safety standards are well-served by AHSS, which offers excellent crash performance and energy absorption capabilities without compromising on weight reduction [2][5]. The cost-effectiveness of AHSS compared to alternatives like aluminum or carbon fiber makes it an attractive option for European automakers operating in a highly competitive market [6]. This continuous advancement has made AHSS particularly valuable in the production of electric vehicles, where its strength-to-weight ratio helps offset battery weight and extend vehicle range [7].

Figure 1.1 shows a schematic drawing for different grades of steel used in the Volvo XC90 body structure, as an example.

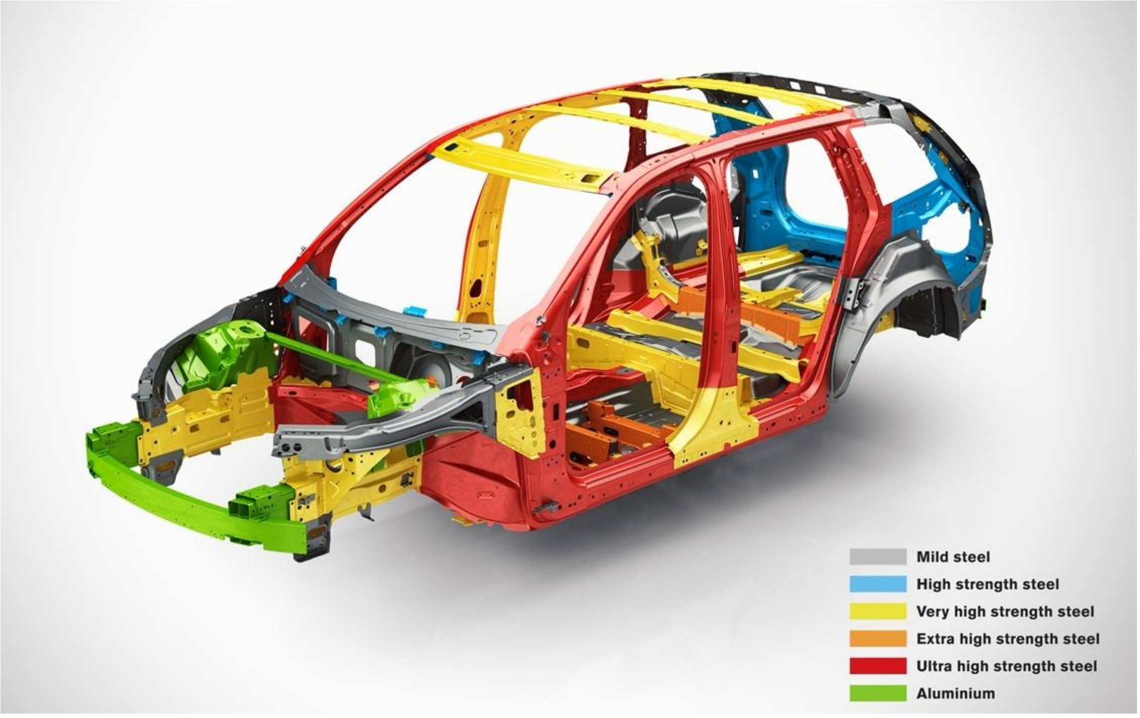

Figure 1.1. Body in white (BIW) coloured schematic of Volvo XC90 (2019) [8].

Resistance spot welding (RSW) has established itself as the dominant joining method in the automotive body-in-white (BIW) industry due to its speed, automation potential, cost-effectiveness, and cleanliness [4]. This welding technique is particularly well-suited for the sheet metals commonly used in automotive construction, offering a fast and efficient process that can produce over 5000 welds in a typical car [9][10]. One of the key benefits of RSW is its adaptability to robotic manipulation, which further increases the speed and precision of the welding process [9]. RSW has proven to be an effective joining method for these advanced materials, making it indispensable in modern automotive manufacturing. The process's ability to join different thicknesses and types of steel, further demonstrates its versatility in automotive applications [11]. The process produces minimal fumes and no spatter, contributing to a cleaner working environment and reducing the need for post-weld cleanup. [12]. RSW can be directed towards quality to provide better crashworthiness compared to other welding processes [13], through enhancing the strengths compared to laser beam welding. For instance, the yield strength of DP600 and DP1000 was increased by 24% and 13% respectively after RSW compared to laser beam welding. [14]

Since the causes of mechanical changes resulting from the RSW process are varied and complex, this thesis aimed to investigate the resistance spot weldability of DP and MS steels, focusing on coveted RSW outcomes that demonstrate superior performance in the automotive industry. The study examined the microstructural evolution and its impact on mechanical properties. The research involved characterizing the microstructure of the fusion zone (FZ), also referred to in other literature as the weld nugget (WN) and heat-affected zone (HAZ) using various techniques, including SEM, EBSD, and hardness mappings, to correlate specific microstructural features with mechanical properties determined by dynamic, quasi-static tests. The challenges in the impact test are encountered in measuring the force as a function of time since a very high sample rate instrumentation in the testing device is required. To modify unwelcoming microstructural constituents, different in-process heat treatments were performed using a second pulse technological parameter. The heat input and cooling rates in HAZ sub-zones welded by single and double-pulse technology were measured physically and by a thermal simulator (SYSWELD). The challenge of capturing the very high seed RSW heating-cooling cycle is encountered, and the allocation of the thermocouple in a certain location is also made difficult by the small HAZ subzone. The HAZ was characterized in terms of microstructure and local mechanical properties. Martensite and ferrite content were microstructurally determined, and mechanical properties were evaluated through mechanical and microstructural testing on these single and double pulse samples, with the goal of determining the characteristics of the weld nugget and HAZ sub-zones for RSW joint integrity.

2. STATE OF THE ART

2.1. Physics background of heat generation in RSW

RSW is a technique that joins overlapped metal sheets by generating heat driven by Joule law through electrical resistance as current flows between the sheets (Faying surface) under pressure from electrodes, resulting in localized melting and formation of a fusion zone (FZ) [15][16][17]. Equation (1) illustrates the heat generated through Joule heating [18].

$$Q = \int_0^t I(t)^2 R(t) dt \qquad (1).$$

where Q is the heat generated, *I(t)* is the applied current, *R(t)* is the resistance across the electrodes, and t is time, When the current or resistance is not constant, integrating the above expression will result in the heat generated in a time interval t [19].

The required electrical current is supplied via two copper-based electrodes and also provides the clamping force to fix the sheets and to bring the surfaces in contact [20]. The RSW setup is schematically shown in *Figure 2.1*. The figure illustrates the various resistances encountered during the RSW process. It provides a clear schematic representation of the electrical resistance components that contribute to heat generation and nugget formation during welding. The bulk resistances of the electrodes and sheets (R1, R3, R5, R7) are naturally present due to the inherent properties of the materials used in the electrodes and workpieces. Bulk resistance is a function of the material's electrical resistivity and geometry, and it plays a crucial role in the overall heat distribution. Contact resistance at the electrode-to-workpiece Interface (R2, R6), These resistances occur where the electrodes touch the workpieces. Factors such as surface roughness, cleanliness, and contact pressure significantly influence these values. Contact resistance at the faying surface (R4), occurs at the interface between the two workpieces being welded. It is particularly critical because it governs the initial heat concentration and affects nugget formation. This resistance is influenced by surface conditions like oxide layers, coatings, or contaminants. As welding progresses, bulk resistance becomes more significant as the materials heat up and deform, reducing contact resistance.

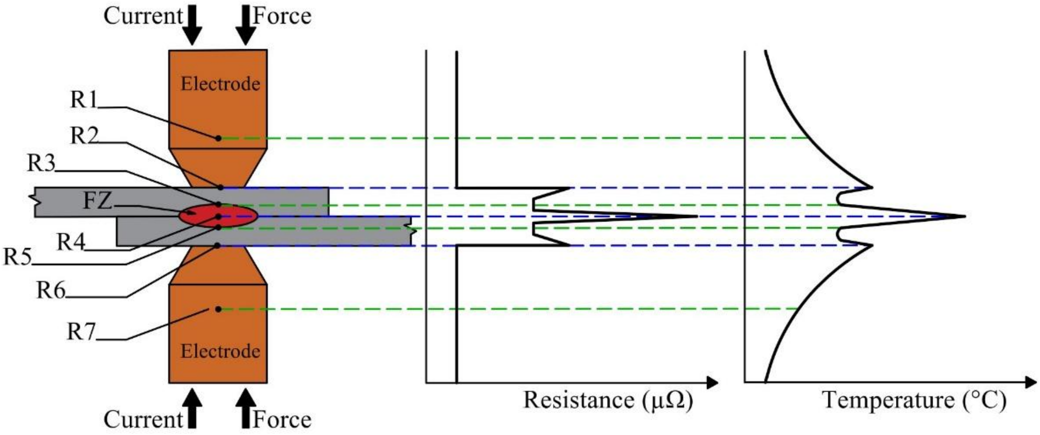

Figure 2.1. Resistances during the RSW process and their amounts [21].

Since R4 is usually the highest resistance, heat is predominantly generated at the interface between the sheets, and thus the formation of the FZ [10][22][23]. The evolution of the FZ can be illustrated by the curve of the electrical resistance shown in *Figure 2.2*. The first peak represents the contact resistance at the interface of the sheets. It breaks down within milliseconds to a minimum, which is referred to as the trough. Due to the increase of the temperature also the resistance increases with time, while local melting facilitates the current flow and thus reduces the resistance. This interplay reaches its equilibrium at the so-called peak. At this point, the temperature stabilizes, and the FZ growth starts to dominate, which causes the resistance to decrease till the current is switched off. The water-cooled electrodes represent strong heat sinks, which cause extremely high cooling rates of several thousand °C/s during the subsequent holding step. Once the electrodes are released, the welding process is finished [20].

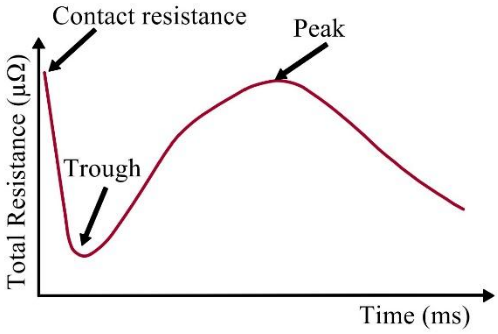

Figure 2.2. Schematic illustration of the electrical resistance curve during welding [20].

2.2. Base material in global formability diagram

The global formability diagram, which compares the strength and elongation of current and emerging steel grades, serves as a valuable tool for understanding the properties of different AHSS types. *Figure 2.3* illustrates the wide range of AHSS grades available, including DP, and MS steels, each offering specific advantages for different automotive components [2].

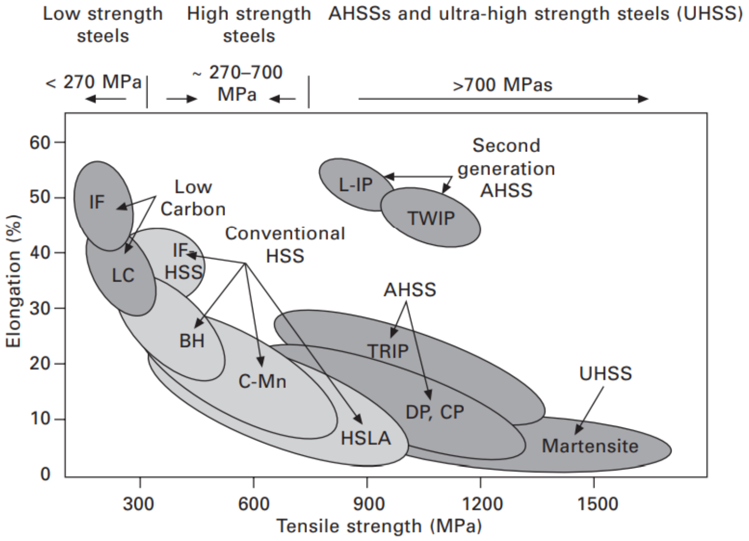

Figure 2.3. Global formability diagram [24].

RSW of AHSS, particularly martensitic (MS) and dual-phase (DP) steels, presents significant challenges in the automotive industry and is widely used in vehicle structural parts to enhance safety performance. These steels are known for their high strength, excellent forming characteristics, and strain energy absorption [3][25]. *Figure 2.3* illustrates the relationship between tensile strength and elongation for various steel types, emphasizing the balance between these properties in DP steels and MS steels. The x-axis represents tensile strength (MPa), while the y-axis indicates elongation (%), highlighting the trade-off between strength and ductility across different steel classes. DP steels, located within the AHSS category, exhibit a favorable combination of strength and elongation. MS steels, on the other hand, are positioned in the Ultra-High-Strength Steel (UHSS) category, with tensile strengths up to 1700 MPa. However, this high strength comes at the expense of ductility, as indicated by their relatively low elongation values.

2.3. Dual-phase steel (DP)

DP steel exhibits unique properties like continuous yielding, low yield-to-tensile strength ratio, and high initial work hardening rate [4][10] offering a balance between strength and ductility [13][26]. It became popular in automotive applications and is being increasingly integrated into body structures for components like bumpers, B-pillars, and side-impact beams due to its unique microstructure and weldability [13][27]. DP steel consists of martensite islands (α’) dispersed in a ferrite matrix (α) [28][29]. This composite microstructure allows DP steels to achieve high strength while maintaining good ductility [10]. The ferrite phase forms the matrix of the material, appearing as larger, irregularly shaped grains that contribute to the steel's ductility and formability. The martensite, visible as smaller, darker islands or regions within the ferrite, provides strength and hardness to the material. *Figure 2.4* shows the microstructure of martensite-ferrite DP steel.

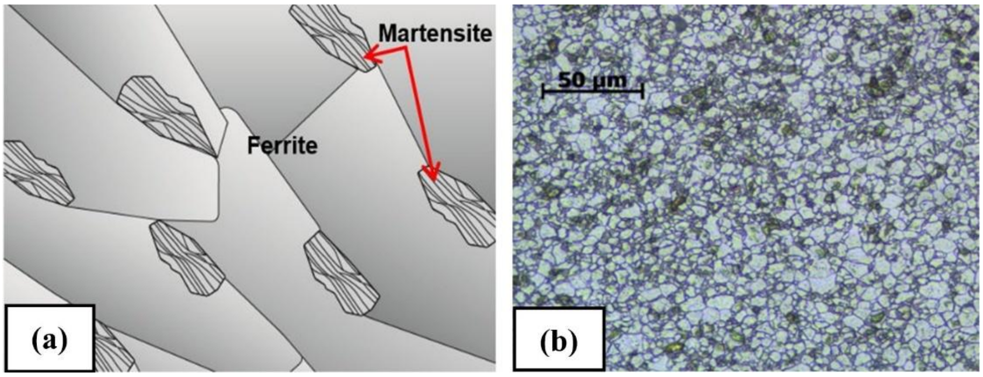

Figure 2.4. A: Schematic of a DP steel microstructure [30]; B: microstructure of Docol DP600 (dark: martensite/light: ferrite) [31].

The strength increases as the grade number rises (e.g., DP450 < DP590 < DP980). This trend reflects the increasing martensite content and strength of the higher-grade DP steels [4]. The manufacturing production process of DP steels involves several key steps, each carefully controlled with a specific heat treatment cycle to achieve the desired microstructure and mechanical properties [32]**.** This cycle is crucial for developing the characteristic DP microstructure consisting of a soft ferrite matrix with dispersed islands of hard martensite exhibiting a uniform distribution that contributes to their balanced mechanical properties [33].

Figure 2.5 shows three different methods, to control the amount of martensite content and the microstructure to optimize the mechanical properties. Route A is rapid cooling from the inter-critical temperature to room temperature. Higher inter-critical temperatures during soaking result in increased martensite content, which enhances tensile strength but reduces elongation. Route B is characterized by slow cooling and quenching from the austenitic region to the ferrite transformation temperature and then quenched to convert the remaining austenite into martensite. This results in lower martensite content compared to Route A, yielding lower tensile strength but better ductility. Route C is a modern technique that combines hot rolling with controlled cooling sequences, including ultrafast cooling followed by slow coil cooling to refine the microstructure [34]. The cooling rate is critical in this step, as it must be precisely controlled to prevent undesired microstructural formations.

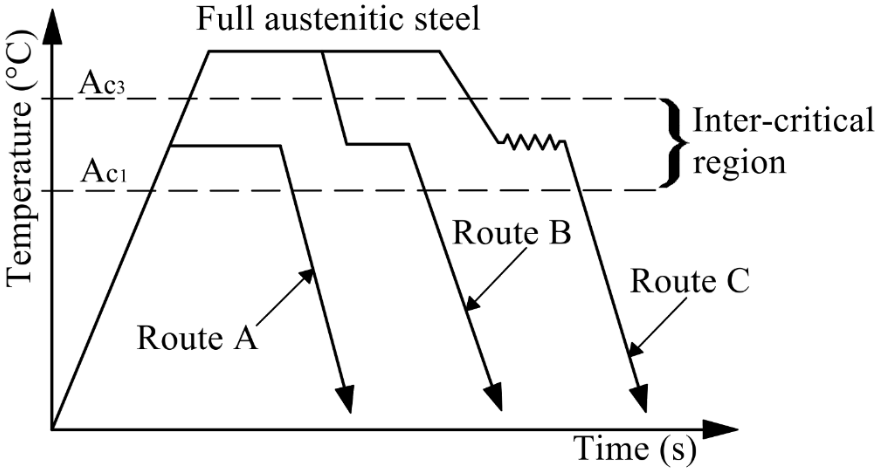

Figure 2.5. Processing routes for producing DP steels [34].

The annealing process involves heating the steel to a temperature within the inter-critical region, typically between 730°C and 860°C, where both ferrite and austenite are stable [35]. The steel is held at this temperature for a specific duration to allow partial austenization, with the amount of austenite formed depending on the desired final martensite content. Following inter-critical annealing, the steel is rapidly cooled or quenched directly to room temperature [36] to transform the austenite into martensite while retaining the ferrite phase [37].

2.4. Martensitic steels (MS)

MS steels are extremely high-strength steels, with a very high UTS (>1200 MPa), up to 1700 MPa with relatively low elongation [38] and provide high stiffness, anti-intrusion, and load-transferring [39]. It's a preferred choice in the automotive industry, especially for achieving lightweight and enhancing the crash safety of vehicles [40]. It is often used in safety-critical components and parts that need to be able to absorb energy in the event of a crash, such as bumper beams, door intrusion beams, and seat belt components [41]. MS steel is characterized by a predominantly martensitic microstructure, offering higher strength but reduced ductility compared to DP steels designed for applications requiring high strength in the automotive industry [42][43]. In the ferrite matrix, martensite constitutes the predominant phase, while ferrite is present in a smaller proportion. This transformation occurs as a result of quenching from the austenite phase. *Figure 2.6* shows the microstructure of martensite-ferrite MS steel.

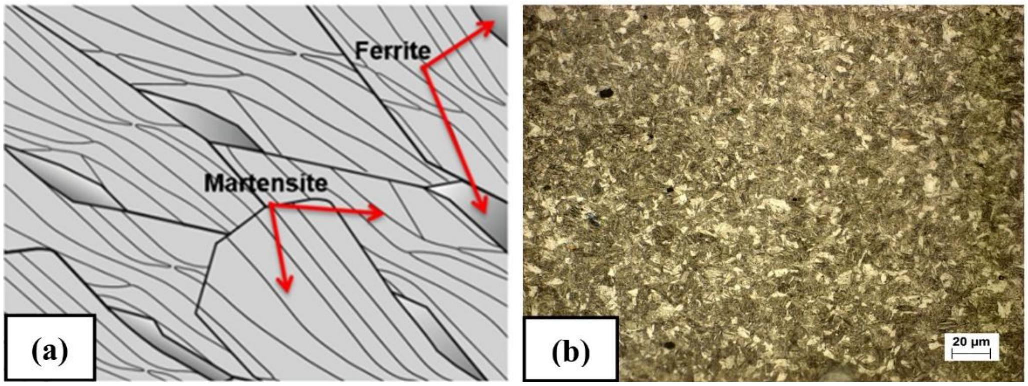

Figure 2.6. A: Schematic of a MS microstructure; B: microstructure of MS1200 [30].

The manufacturing production process of MS steel involves several critical steps, each carefully controlled to achieve the desired microstructure and mechanical properties. *Figure 2.7* shows one of the processes of MS steel production. The key step in producing MS is the heat treatment process, which typically involves austenitization followed by rapid cooling (quenching). The steel is heated to a temperature above the austenite transformation temperature (typically 900-1000°C) and held for a sufficient time to ensure complete austenitization [44]. Following austenitization, the steel is rapidly cooled or quenched to transform the austenite into martensite. The cooling rate must be fast enough to suppress the formation of other phases such as ferrite, pearlite, or bainite [45].

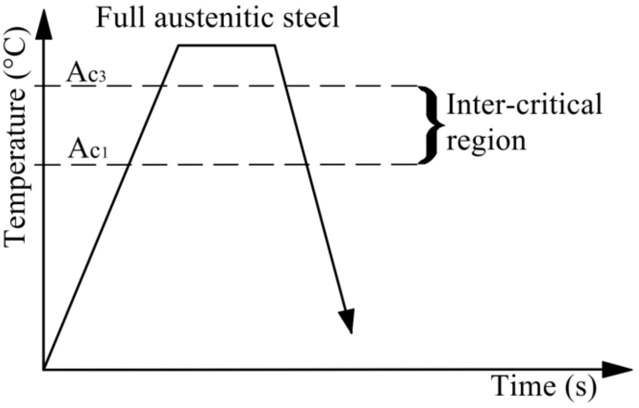

Figure 2.7. Processing route for producing MS steels [24].

After quenching, MS steel is often tempered to reduce internal stresses, improve ductility, and achieve a balance between strength and toughness. Tempering involves reheating the quenched steel to a temperature below the austenite formation temperature. For many steels, tempering is typically performed in the range of 500–650°C to achieve a balance between hardness and ductility, with the material held at the tempering temperature for a specific time before cooling [46]. The applied post-heat treatment process is to improve ductility where the additive elements such as manganese, silicon, and boron are added to increase the hardness and improve other mechanical properties [47]. The carbon in MS steels increases the hardenability and contributes to further strengthening the martensite [34].

2.5. RSW parameters

The joining of martensitic AHSS presents considerable challenges due to their high strength, susceptibility to cracking, and the adverse microstructural changes that occur during the welding process. [48][49][50]. For thinner AHSS materials, RSW is the most commonly employed joining technique. However, this process is often associated with a meaningful reduction in the mechanical properties and strength of the welded joint. [51][52][53][54][55].

Welding parameters that influence the RSW process; squeeze time (ST) which is the initial period when electrodes apply pressure to the metal sheets before current flows; welding current which is the magnitude of the electric current flowing through the electrodes; welding time (WT) which is the duration of flowing applied current; holding time (HT) which is the time electrodes remain in place after the current stops, allowing the weld to cool under pressure; and electrode force (EF) which is the force exerted by the electrodes to hold the workpieces securely in place during welding [10]. *Figure 2.9*a shows a schematic drawing example of the welding cycle of one pulse.

Understanding the effects of welding parameters on the thermal cycle (temperature-time) in RSW is crucial for optimizing these parameters and achieving a balance between the strength and ductility of the required high-performance spot joint. [56]. For instance, in pulse technological welding parameters varying the second pulse current in a pulsed RSW schedule can modify the weld thermal cycle and alter cooling rates during welding [57][58][59].

In general, there are three important factors for evaluating the quality of RSW, which are the weld-nugget size, weld mechanical performance, and failure modes. [51]. According to Aslanlar (2006), the size and quality of the FZ in RSW are influenced significantly by parameters like welding current, electrode force, and welding time. Optimizing these parameters can achieve the desired qualities, ensuring strength and defect-free RSW joints. [60]. Welding parameters play a crucial role in determining FZ characteristics and overall weld failure behavior. [23]. The nugget size and quality are critical indicators of weld strength and integrity. The optimum value for each welding parameter that maximizes nugget size and mechanical properties [56].

2.6. The effect of welding parameters

2.6.1. Electrode force

Electrode force significantly affects FZ size and optimizes the mechanical properties. Increasing the electrode force enhances joint strength by enlarging the weld nugget, but only up to a critical limit. Beyond this point, the weld quality deteriorates because the drop in electrical resistance reduces heat at the interface [61]. The effect of electrode force on the microhardness distribution across the RSW is relatively weak, however, the increase in electrode force generally enhances both tensile-shear load and failure energy up to a certain point [61]. The hardness values of weld nuggets produced using two different electrode sizes have shown no significant difference, suggesting that electrode size mainly influences weld geometry and dimensions rather than affecting the microstructural properties responsible for hardness [62]. The weld zone appears symmetrical, indicating proper welding, and the standard weld core height/width ratio, suggests correct electrode force [11]. Excessive force can reduce the FZ size due to decreased contact resistance and heat generation, leading to lower mechanical properties [61]. Welding defects such as expulsion, can reduce the weld quality and lead to reduce the mechanical properties

[10][63][64]. Expulsion can occur when electrode force is too low or welding time is prolonged, leading to excessive heat input; conversely, increasing electrode force helps reduce metal splash during welding [61][63].

2.6.2. Welding current and time

The relationship between welding current and weld strength shows a clear positive correlation up to an optimal range [64]. Under certain RSW parameters, exceeding a specific welding current results in greater electrode indentation (plastic deformation) on the sheet surfaces, with the indentation increasing as the current rises due to the combined effects of heat generated by the current and the applied electrode force [10][65]. However, while greater indentation can enhance FZ sizes, excessive depth may compromise weld performance by diminishing the effective thickness of the welded sheets and influencing the mechanical properties of the weld [10][66]. The optimal range of welding currents that produce large FZ sizes without causing excessive indentation or expulsion [10]. Electrode indentation can promote the desired failure mode through stress concentration and higher energy absorption before failure but also may negatively impact overall weld quality [23][61]. Excessive heat input resulting from high current and prolonged weld times caused multiple failures, including blowout, which is the expulsion of molten metal from the weld zone, and splashing, characterized by the ejection of small particles of molten metal [65].

Welding currents and times varied based on material thickness and coating [67]. Higher welding currents and longer welding times increase the heat input, leading to larger nugget sizes, allowing for greater material fusion leading to increased indentation and improved mechanical properties in low-carbon (LC) and high-carbon (HC) steels [5][68][69]. Slight increase in martensite with increasing welding current [11] and longer welding time lead to larger martensite sizes and decreased hardness from grain growth [63]. Higher welding currents lead to more pronounced microstructural changes in the HAZ, particularly in the SCHAZ, where martensite tempering occurs. This results in a softened zone that can influence the mechanical properties and failure modes of the weld [66] *Figure 2.10* shows the softening phenomenon. HAZ softening is caused by increased tempering of martensite. While electrode force has minimal influence, welding time plays the most significant role in affecting microhardness, followed by welding current with a moderate impact. Excessive heat input from prolonged welding time and high current leads to phase softening, further reducing the hardness of the weld nugget [56]. Welding time has the most significant effect on FZ microhardness and significantly influences the toughness characteristics of welds, both tensile-shear and cross-tensile strengths increase as the welding current rises, reaching their maximum at a specified current [10][59].Higher welding currents and longer welding times lead to coarser structures in the FZ and HAZ, as they reduce the temperature gradient and increase heat input [56]. Prolonged welding times, particularly at higher penetration rates, lead to coarser microstructures in the FZ due to extended exposure to elevated temperatures [63].

In the case of double pulse welding microstructural analysis revealed larger FZ sizes [27]. Research has found a significant distinction between single pulse welding (SPW) and double pulse welding (2-pulse) methods, with 2-pulse achieving a nugget diameter approximately 13.8% larger than that of SPW in the same welding parameters. This increase in size is attributed to the higher heat input associated with the 2-pulse process showing that the welding current is a more critical factor in heat generation than the duration of the pulse [59][70]. *Figure 2.8* shows the difference between SPW and 2-pulse in terms of load-displacement (L-D) diagrams.

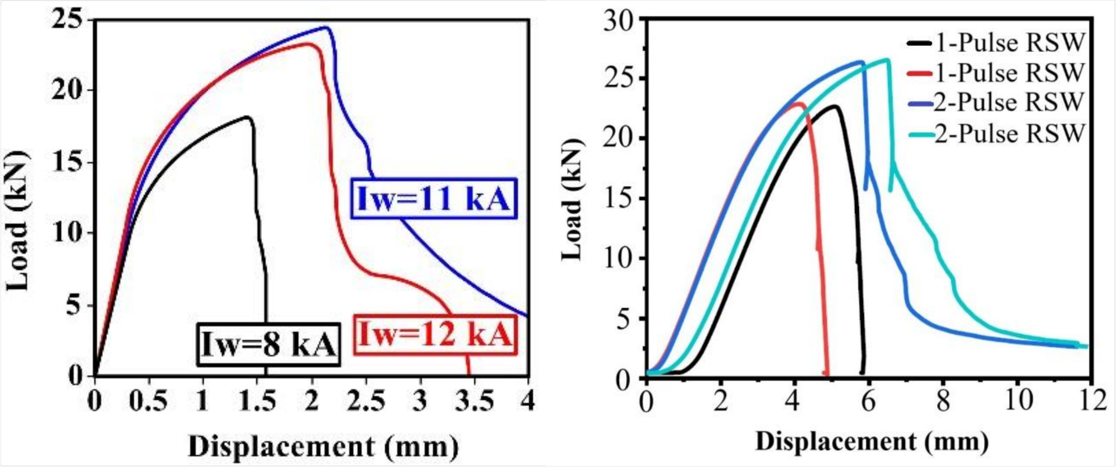

Figure 2.8. T-S test results in different RSW parameters. (a) T-S test results of different welding currents [10], (b) T-S test results of different pulsation [27].

2.6.3. Pulsation technology

The conventional RSW technology has been employed by applying a single pulse with varying welding times and/or currents. These variations affect the sizes of the FZ and the HAZ [71][72]. The RSW pulsation technological parameter is a method for regulating electrical pulses hence control generated heat and enhanced joint reliability. Moreover, the size and hardness of the FZ and HAZ are influenced by the local thermal history and can be controlled by the pulse current [58]. *Figure 2.9* shows the welding cycle for RSW single and 2-pulse.

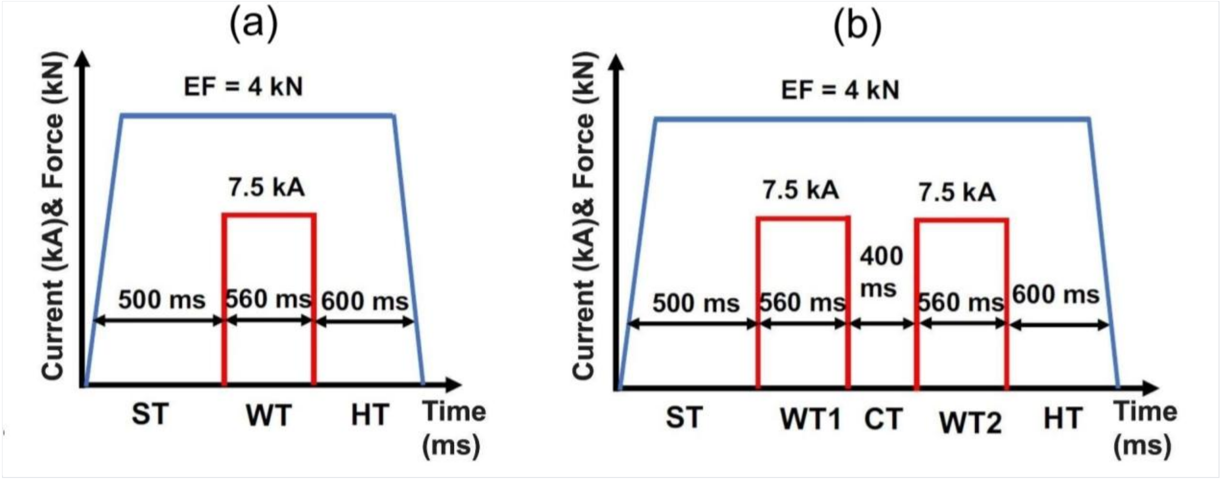

Figure 2.9. (a) RSW schemes used in the present investigation a single-pulse welding, (b) 2-pulse welding. [27].

In recent years, pulsed welding technology has gained increasing attention, particularly for high-strength steel [55][73][74][75][76][77][78][79]. The pulsed RSW technology method can produce FZ sizes similar to those in short-time welding but with different softening characteristics, primarily due to the second pulse, which effectively heat-treats both the FZ and the HAZ [80]. It is reported that the extent of softening in the FZ depends on the pulse parameters, including welding current, duration, and cooling time between pulses [75][76][77][78][79] which determine the applied thermal cycles on each region.

Previous research reported significant differences in hardness distribution between 1-pulse and 2-pulse technologies [81]. The investigations on AHSS's on two- or multi-pulse techniques revealed that the FZ size is primarily altered by the first pulse, with subsequent pulses impacting the microstructure as demonstrated in the studies by [75][76][77][78][79].

This modification of the weld microstructure offers potential improvements in the overall mechanical properties and performance of the welded joint [28].The improvements in mechanical properties and microstructure are attributed to the secondary heating cycle inherent in the 2-pulse RSW process, which promotes the formation of tempered martensite, thereby enhancing weld toughness [27]. The second pulse resulting stronger welds, likely due to increased heat input and more effective martensite tempering [59].

Research emphasized that the tempering effect in the FZ can be adjusted by modifying pulse parameters [82]. Similarly, Eftekharimilani *et al.* [74] reported that the 2nd pulse can anneal the primary FZ at the edges, homogenizing alloying elements and improving the joint's cross-tension strength [74]. Several studies on DP and 22MnB5 steels [76][78][79] have also found that the second pulse decreases the hardness of FZ and enhances the cross-tension strength of the joint.

Among the double pulse configurations, the weld with two equal current pulses stood out, achieving the highest L-D values while also displaying the most favorable full plug failure mode. This indicates that the use of double pulse welding, particularly with equal current pulses, can significantly enhance the mechanical properties and overall quality of the welds [83]. Mechanical testing demonstrates the superior performance of 2-pulse RSW specimens, with a 15.6% higher average peak load and an 83.1% higher failure energy compared to single-pulse weld specimens [59]. Double pulse welding and higher welding current up to limit enhances tensile-shear strength and energy absorption compared to SPW (see *Figure 2.8*b) [28][83][84][85].

2.7. Heat-affected sub zones

The macrostructure of the RSW is divided into three main zones: the fusion zone (FZ), the heat-affected zone (HAZ), and the Base Metal (BM). The HAZ surrounds the FZ and undergoes solid-state phase transformations without melting [63][66]. It is subdivided into sub-zones with distinct temperature ranges including Upper-Critical Heat-Affected Zone (UCHAZ) (800°C to 1200°C), typically denoted as Ac3 and consists of the fine-grained heat-affected zone (FGHAZ), and the coarse-grained heat-affected zone (CGHAZ), [82]**,** Inter-Critical Heat-Affected Zone (ICHAZ) (720°C to 790°C), and Sub-Critical Heat-Affected Zone (SCHAZ) (350°C to 650°C) donated below the A1 transformation temperature [56][61][63]. Fine-grained heat-affected zone (FGHAZ) and coarse-grained heat-affected zone (CGHAZ) are integral parts of UCHAZ, each contributing differently to the overall mechanical behavior of the welded joint due to their distinct microstructural characteristics. The size of the HAZ and its sub-zones increases with higher welding currents, with the SCHAZ being particularly significant due to its larger size and contribution to softening [66]. The BM remains unaffected by the heat, retaining its original microstructure. *Figure 2.10* shows an example of the RSW FZ and HAZ subzones with softening resulting from RSW.

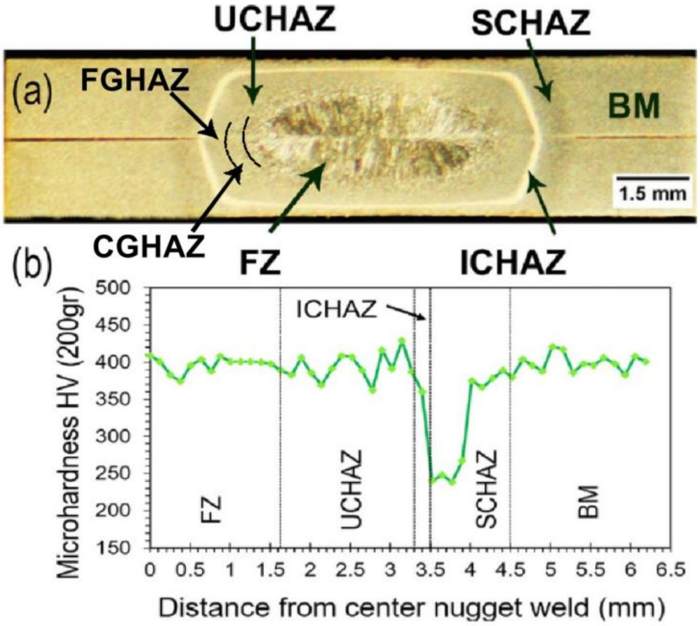

Figure 2.10. Typical (a) macrostructure, (b) the hardness profile of the MS1400 steel RSW.[66].

2.8. *Microstructural transformation in RSW*

The base material microstructure serves as a reference point for comparing changes that occur during the RSW process. Understanding the initial microstructure is crucial for interpreting the transformations and property changes in the welded regions [13] Using both optical microscopy and SEM offers a comprehensive understanding of the weld's microstructure and mechanical properties. In EBSD analysis, the IQ map serves as a crucial tool for visualizing diffraction pattern quality, enabling the identification of microstructural features, grain boundary characteristics, and transitions between weld zones, such as the HAZ and FZ. By combining IQ map data with EBSD results, detailed insights into grain size distribution, orientation relationships, and martensite distribution were achieved, facilitating a comprehensive understanding of the microstructural evolution and its impact on the mechanical properties of resistance spot weld [86].

In RSW of AHSS like DP and MS steels, the austenite can transform into martensite, bainite, or ferrite/perlite depending on the cooling rate and the hardenability of the steels [11] significantly influencing the phase transformations in the FZ and HAZ [4][10]. These transformations, along with the size and distribution of martensite, and gradual microstructural changes such as retained austenite and lower bainite in transition areas, critically affect the mechanical properties of the welded joint [64][68].

Martensite is a hard, brittle phase in steel formed by the rapid cooling of austenite, which traps carbon in the lattice, causing distortion and hardness, with its properties influenced by carbon content [68]. In DP and MS steels, a martensitic microstructure forms in the weld metal when the cooling time $t_{8/5}$ (time to cool from 800°C to 500°C) is less than 3 seconds [14], with rapid cooling rates typical of RSW intersecting only with the martensite start line, resulting in predominantly martensitic structures in the FZ and HAZ [13][70][87]; the critical cooling time extends with higher carbon equivalents, highlighting the influence of alloy composition and transformation temperatures on martensite formation and hardness [43].

Bainite can form during rapid quenching after initial martensite, with its detection complicated by similar dislocation densities to martensite [88]. A comparison of two DP600 steels revealed that higher carbon content promoted the formation of bainite (~6.8 ± 2%) while lower-carbon grades contained none, despite both having similar ferrite grain sizes and total martensite content but differing significantly in martensite distribution and morphology [26]. Slower cooling rates further lead to mixed microstructures, including ferrite, pearlite, and possibly some martensite or bainite.

DP steel chemistry influences tempering behavior and softening resistance. Richer base metal chemistry (higher Cr, Mn) showed higher resistance to softening [29]. Tempering characteristics of martensite in DP steels are similar to fully MS steel of comparable carbon content [29]. The extent of tempering/softening depends on the diffusion of carbon, controlled by temperature and time [29]. Steel composition, particularly carbon content and other alloying elements, affects the hardenability and transformation temperatures [43]. For instance, The martensite start temperature (Ms) and martensite finish temperature (Mf) are critical parameters that depend on the steel's chemical composition and influence the quenching process [89]. Higher carbon levels yield finer microstructures with increased hardness and strength but also greater brittleness, while lower carbon content results in coarser structures that enhance toughness at the expense of hardness and strength [68].

Microhardness testing is an effective way to assess spot weld quality by providing insights into weld strength, ductility, and hardness, with particular attention to HAZ softening, which can impact the mechanical performance of the joint [28][56]. The symmetrical hardness profile across the weld center, despite typical variability in the FZ and HAZ due to microstructural heterogeneity, suggests consistent heat input and cooling rates, indicating a stable welding process [5][13][90]. Hardness profiles across the weld revealed complex microstructural evolution. The FZ and CGHAZ exhibited peak hardness due to fresh martensite formation [59]. While the HAZ showed a gradual hardness drop (softening) from martensite tempering [63]. A study monitored the softening in the HAZ of different martensitic steel (MS) grades so due to allotriomorphic ferrite formation in the ICHAZ and the tempering of martensite in SCHAZ [91]. The softening is directly proportional to the martensite volume fraction (MVF) in the BM and is particularly pronounced in higher grades like DP980 which is not as pronounced in DP600 [4][10][14]. It was found that the softening in MS RSW joints is used to improve some mechanical properties of spot weld joints in the automotive industry due to its direct proportionality with elongation, which helps avoid brittleness. Additionally, this softening increases the ability of impact load absorption, improving the ductility of the RSW joints and enhancing their capacity to absorb applied stresses [51]. Controlling HAZ softening becomes a critical factor in producing high-performance welds in MS steel, as it directly impacts the overall strength and integrity of the welded structure [69].

Continuous cooling transformation (CCT) diagrams and cooling curves provide a theoretical basis for understanding and predicting microstructural evolution during the welding process [43]. This diagram illustrates the formation of various phases as the steel cools from its austenitic state at different rates [59].

2.8.1. Fusion zone (FZ)

During the welding process, the FZ undergoes complete melting and rapid solidification, resulting in a dendritic structure that grows directionally from the fusion line toward the center of the FZ [27][28][56][61][63][66][70][74][85][92][93][94], the fusion zone (FZ) in RSW of DP and MS steels, characterized by a fully martensitic structure with a columnar lath or needle-like morphology [10][13][14][43][51][64][66][69][95][96]. This transformation is facilitated by the high cooling rates inherent to the RSW process primarily due to the rapid cooling caused by the water-cooled electrodes, which suppresses the formation of phases like ferrite or bainite. SEM micrograph shows the FZ at a lower magnification, illustrating a fully martensitic structure characterized by lath morphology typical of martensite in low-carbon steels [10][13]. Lath martensite has a multi-scale complicated hierarchical morphology. *Figure 2.11*a shows a schematic of the three-level hierarchy in lath martensite microstructure, laths, blocks, and packets. *Figure 2.11*b illustrates a typical EBSD orientation color map of the martensite structure in steel with 0.2 wt% carbon. These morphological and crystallographic characteristics of lath martensite in steel greatly affect its mechanical properties [43].

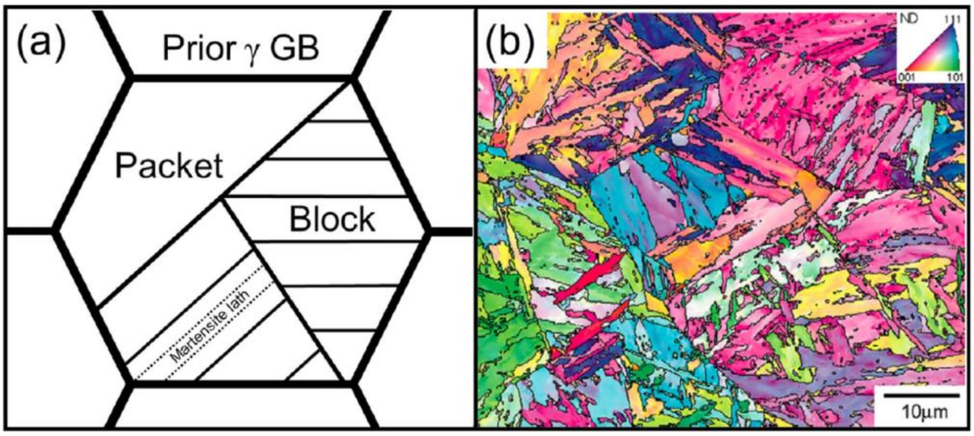

Figure 2.11. (a) Schematic illustration of three-level hierarchy in lath martensite structure, (b) Inverse pole figure (IPF) color map of the lath martensite structure in the 0.2 wt% C steel [43].

The enhanced performance of 2-pulse joints is attributed to the FZ's randomly oriented grains with high-angle grain boundaries and the toughness improvement from martensite tempering [59]. Double pulse welds exhibit a distinct microstructural division, with an inner fusion zone (FZ2) comprising coarse columnar grains similar to single pulse welds [92] (see *Figure 2.12*), and an outer Rex-zone characterized by equiaxed prior austenite grains with coarser Bain groups and fewer high-angle grain boundaries resulting in lower hardness and residual strain, compared to FZ2 which affects crack initiation and propagation resistance [28][84][92].

The 2-pulse FZ, benefiting from a secondary heating cycle, exhibits refined, equiaxed grains with fewer low-angle grain boundaries (LAGBs) and a higher proportion of high-angle grain boundaries (HAGBs) is thought to contribute to improved mechanical properties, potentially resulting in a tougher weld structure [28][84]. The HAGBs in martensitic structures act as barriers to dislocation movement, contributing to the material's strength [68].

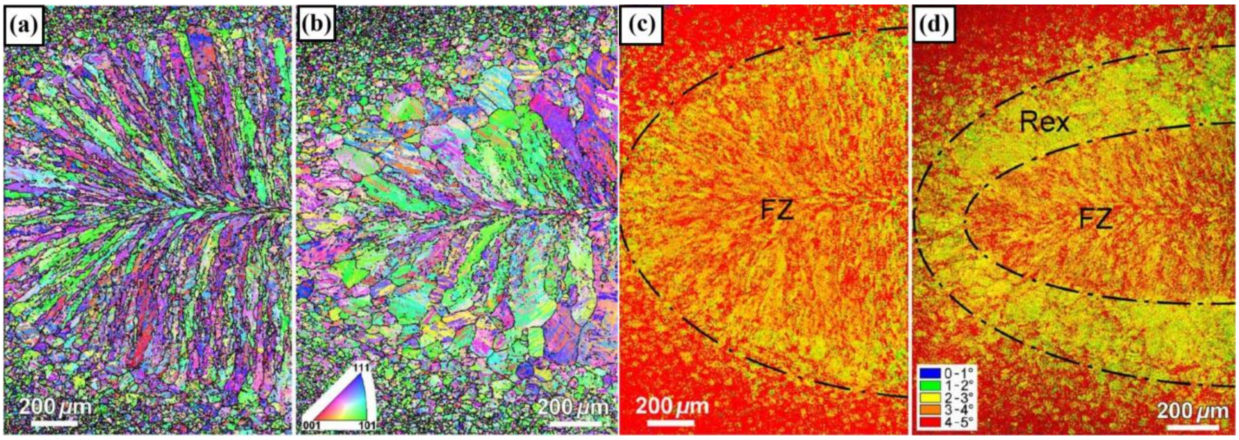

Figure 2.12. Inverse pole figure map and average misorientation map made at welding current of 6.4 kA RSW. (a,c) single pulse weld, (b,d) 2- pulse weld [92].

2.8.2. Upper-critical HAZ

The UCHAZ, located adjacent to the FZ does not melt during welding but reaches a peak temperature above A_{c3} [51]. Therefore, full austenitization is achieved during heating [51][66] which later transforms to new martensite packets during subsequent cooling [51]. Depending on the peak temperature and distance from the FZ, this zone contains both larger and smaller grains [10][51][66][69], with finer grains contributing to slightly higher hardness compared to coarser grains [51]. In cross-tension tests, failure often occurs in UCHAZ, as noted by Tamizi [51].

Coarse-Grained HAZ

In the CGHAZ, single pulse welds exhibit coarse lath martensite packets due to significant grain growth at temperatures above overheated region Ac3 [27] with significant austenite grain growth followed by rapid cooling which significantly impacts the microstructure characterized by coarse martensite, larger grain size, and reduced toughness, making it prone to crack initiation and propagation and a critical failure location during mechanical testing [4][10][28][61][66][97].

The double pulse welding process significantly refines the microstructure of the CGHAZ [28], resulting in finer grains that enhance toughness compared to coarser-grained regions [66].The CGHAZ is characterized by coarse grains with a mixed microstructure consisting of tempered martensite (T α'), retained austenite, and occasionally ferrite, all of which influence its overall mechanical properties [85][13].

Fine-Grained HAZ

The FGHAZ, located slightly farther from the FZ within the UCHAZ, experiences temperatures just above Ac3 [4], leading to full austenitization with smaller austenite grains [10]. Upon rapid cooling, it develops a fully martensitic structure with finer grains compared to the CGHAZ [66]. The FGHAZ exhibits a heterogeneous microstructure comprising fine grains of tempered martensite, ferrite, and retained austenite, resulting from full austenitization and rapid cooling, with tempering contributing to its refined structure [13][61][85].

In double pulse weld the FGHAZ exhibits the highest fracture toughness due to its ultra-fine structure of martensite and untransformed ferrite, which provides both high strength and toughness beneficial for weld performance [97]. In contrast, the FGHAZ consists of fine packets of lath martensite, resulting from complete austenitization at lower peak temperatures than the CGHAZ [27].

2.8.3. Inter-critical HAZ

In ICHAZ base metal microstructure partially transforms into austenite during heating leading to a DP microstructure of ferrite plus martensite after cooling [10][51][66][69][98]. Experiences temperatures between Ac1 and Ac3 the temperature in this zone partially transforms the martensitic BM into ferrite and austenite, which then transforms back to a mixture of ferrite and martensite and tempered original martensite upon cooling [51][66][98]. This zone shows a gradual transition from the tempered martensite structure to a more martensitic structure. The ferrite area decreases, and martensite content increases as you move from SCHAZ to ICHAZ [4].

2.8.4. Sub-critical HAZ

The SCHAZ experiences peak temperatures between 600-700°C, below the Ac1 temperature, where no austenite transformation occurs, resulting in the tempering of existing martensite and leading to HAZ-softening [4][51][66][69]. Literature [51][66][98] indicates that the initial martensite is tempered in SCHAZ by the welding thermal cycle [82]. This leads to softening which, primarily due to martensite tempering where carbon atoms diffuse out from the supersaturated martensite phase to form cementite (Fe_3C), results in a tempered martensite structure that exhibits reduced strength and hardness but increased ductility [99]. The tempered martensite structure in the SCHAZ is characterized by fragmented laths and precipitated carbides, which are distributed more or less uniformly [4][13][51]. The tempered martensite structure, observed in DP600, DP780, DP980, and MS1400. MS1400 has shown the most pronounced tempering effect and a more softening [4].

The SCHAZ in double pulse welds exhibits fine grains of ferrite and tempered martensite [27][28]. The double pulse approach induces more pronounced softening in the SCHAZ**,** which contributes to enhanced mechanical properties of the weld [92]. The softening reduces stress concentration around the weld edge, enhancing mechanical performance [28].

3. MECHANICAL TESTING

Mechanical testing is essential for assessing the quality of RSW joints. Various types of mechanical tests are used to evaluate the strength, durability, and overall performance of the welds. Vehicle spot welds are subjected to complex loading histories during service. Strength under quasi-static, impact, and fatigue loading is critical for durability and safety [100]. Consequently, it is necessary to conduct mechanical testing to evaluate the performance of spot welds under these varying conditions and ensure their reliability in real-world applications. No clear relationships were found between BM mechanical properties (yield strength, tensile strength) and joint performance. When making claims about relationships between material properties and joint performance, experimental conditions should be clearly identified [67]. Predicting joint performance in AHSS is complex, involving the interaction of geometrical factors, metallurgical properties, and loading mode [23][100]. Weld nugget size is a key factor controlling mechanical properties and failure mode, a direct correlation where larger nugget sizes enhance mechanical performance [61]. A strong correlation was found between static and dynamic test results for both tensile-shear and cross-tension. Static test results can be indicative of dynamic performance [67].

3.1. Failure mode

The American Welding Society (AWS) has classified eight potential failure types for AHSS spot welds, with the most characteristic being Button Pullout (BP), Partial Interfacial Failure (PIF), and Full Interfacial Failure (FIF), while the study examined three different DP steels: DP450, DP590, and DP980 [101].

Understanding the failure location is important for predicting and controlling the failure mode of resistance spot welds in different materials [23]. The conventional rules (4t^0.5 or 5t^0.5) are inadequate for ensuring pull-out failure in thicker spot welds. This suggests that these standards may be insufficient for ensuring pull-out failure in DP and MS steels [98][100]. This finding study underscores the need for revised weld size criteria that incorporate metallurgical factors, particularly for advanced high-strength DP steels [10]. Factors such as nugget size, MVF, carbon content, SCHAZ softening, and microstructural properties significantly influence failure mode transitions [68][99]. As FZ size increases, failure typically shifts from interfacial failure (IF), governed by FZ shear strength, to pull-out failure (PF), which enhances energy absorption and load-bearing capacity, with fractures often originating at the nugget periphery [10][23][70][92][100].

The dominant failure mode is determined by the competition between shear plastic deformation in the FZ and necking in the BM or HAZ, depending on which reaches critical stress first in the mechanical testing [23][68]. The failure mode is considered a qualitative measure of weld quality. Pullout failure is generally preferred as it indicates a stronger, more ductile joint capable of absorbing more energy before failure [61].

The failure mode in RSW is crucial for evaluating the quality and performance of welds, particularly when subjected to cross-tension and tensile shear tests. For example, Interfacial Failure (IF) occurs when the FZ fractures along the interface between the two sheets indicating issues such as insufficient heat input, poor electrode alignment, or contamination at the weld interface. It is generally considered undesirable because it indicates weak bonding and insufficient fusion at the weld interface [102][103][104].

Pull-out failure (PF) occurs when the FZ remains intact, and the surrounding sheet material tears away. This mode is preferred as it indicates a stronger weld with better energy absorption capabilities [105][106][107]. *Figure 3.1* shows the schematic representation of the failure modes during the cross-tension test [66]. Section 2.1 demonstrates how welding parameters affect the failure mode.

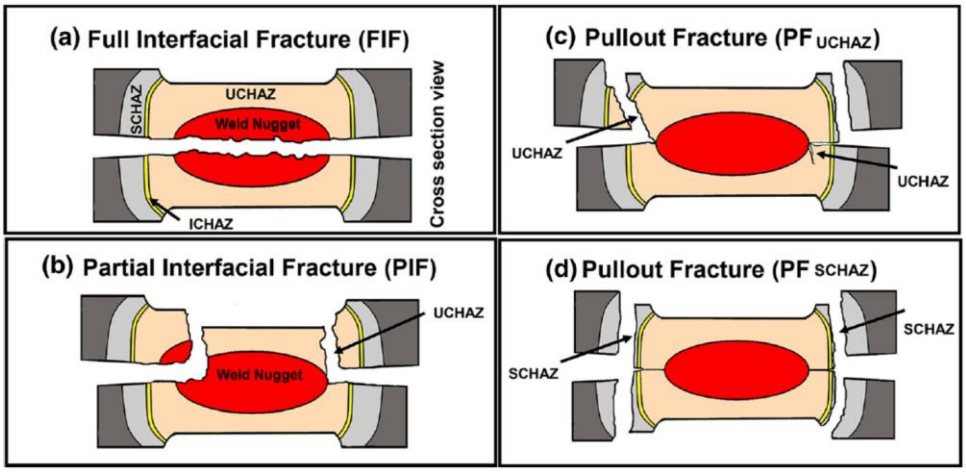

Figure 3.1. Four typical types of fracture mode after cross-tension test in MS1400 RSW [66].

Pullout failure occurs when the FZ remains intact but is pulled out from one of the welded sheets, creating a hole and leaving a fracture surface marked by roughness and plastic deformation, indicating substantial energy absorption and joint integrity; this mode, often seen with larger fusion zones, is preferred for its association with higher energy absorption, better crashworthiness, and greater load-bearing capacity [61][100], especially in double-sided pullout cases or round pullout failures in softened SCHAZ areas particularly when significant softening leads to plastic deformation and necking before the FZ fails [101]. Double-sided pullout failures, which show greater plastic deformation compared to single-sided failures [10][99]. Single-sided pullout failure mode while still better than interfacial failure, it is generally less desirable than double-sided pullout [10]. While HAZ softening can facilitate beneficial button pullout failures, it may also result in early failures due to strain localization in the softened areas. However, the strong performance of DP980, despite pronounced HAZ softening, indicates that this softening can enable the preferred pullout failure mode without substantially weakening the overall joint strength [4].

In scenarios where HAZ softening is absent like in DP600 RSW, pullout failure typically occurs at the softer BM rather than the harder HAZ. HAZ softening can shift the failure location from the BM or CGHAZ to the softer SCHAZ, resulting in a change of load-bearing capacity of the spot welds [66]. Interfacial failure is leading to a rapid decrease in load after peak strength due to quick crack propagation [10]. Weld strength in interfacial failure mode correlates strongly with FZ size and hardness, the pullout mode exhibits a more complex behavior due to competing effects of increased FZ size and HAZ softening [98]. The severe tempering in the SCHAZ of 2-pulse RSW joints promotes plastic deformation and the pullout failure mode, contributing to improved mechanical performance [27].

3.2. Quasi-static tests

Two quasi-static loading conditions, tensile-shear and cross-tension commonly employed in the automotive industry to assess weldability challenges [101]. RSW analysis often employs load-displacement plots to evaluate weld performance comprehensively. These plots reveal critical parameters such as peak load (P_{max}) and failure energy (W_{max}), which are essential for assessing weld strength and energy absorption capacity [59]. The curve's shape provides valuable insights into the weld's behavior under stress, with the initial linear portion indicating elastic deformation and the subsequent non-linear section representing plastic deformation [5][56]. Interfacial failure modes exhibit a sharp drop in load after reaching peak levels [10], while pullout failure modes demonstrate a gradual drop-off after peak load in the suggested ductile failure mode [59]. The load-displacement curves for both test types provide further insights into the deformation behavior, with tensile-shear tests showing higher strength but lower ductility compared to cross-tensile tests [70]. The higher peak loads and larger displacements not only suggest superior mechanical performance in their spot welds but also indicate an enhanced crashworthiness potential due to their increased energy absorption capabilities [4].

3.2.1. Cross-Tension testing

The cross-tension test is used to evaluate the strength and performance of resistance spot welds subjected to a tensile load applied perpendicular to the plane of the sheets [105]. The complex loading conditions in cross-tension tests, combined with the non-homogeneous microstructure and geometry of the weld, make it challenging to isolate the specific contributions of individual microstructural features to crack initiation and propagation [28]. The study of crack propagation in DP980 was conducted through interrupted cross-tension tests, revealing that crack initiation occurs at the notch tip under (tensile opening) [101][108]. Crack initiation was linked to stress concentration along the FZ periphery, amplified by electrode welding force. Weld design should consider competition between notch stress concentration and HAZ softening [69]. *Figure 3.2* depicts the stress distribution for a cross-tension sample, focusing on shear stress around the weld nugget. The shear stress distribution exhibits four identical sectors of stress concentration, demonstrating symmetry consistent with the applied tensile load. The maximum shear stress is observed at the key angular points (0°, 90°, 180°, and 270°), emphasizing the material's shear resistance and its influence on the failure mode [106].

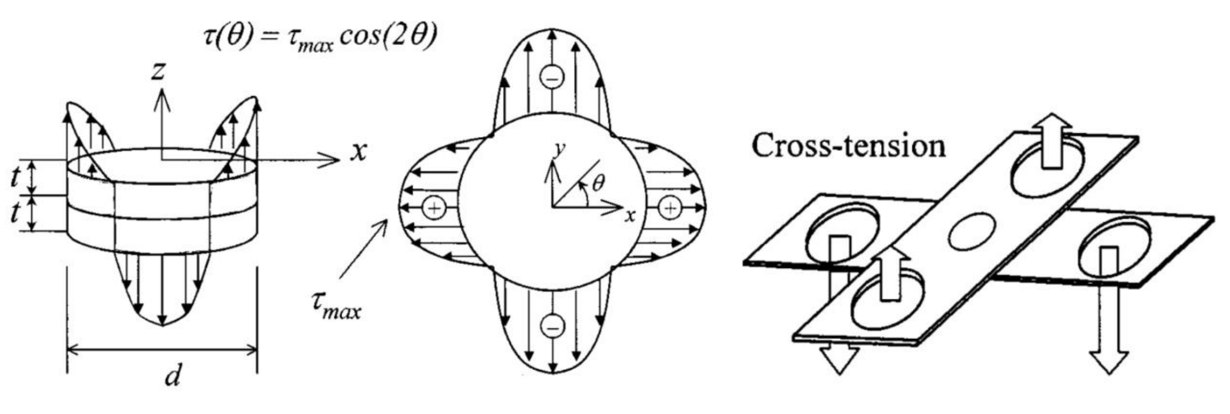

Figure 3.2. Stress distribution around the weld nugget in a cross-tension sample & Cross tension and lap-shear test sample geometries [106].

Cross-tension strength tests revealed that maximum force increased significantly in 2-pulse welds with short cooling times. However, extending the cooling time led to a reduction in mechanical performance [109].

3.2.2. Tensile-shear test

Favorable strength in the tensile-shear test is depicted by the maximum force the welded joint can sustain shear loading conditions before failure with high energy absorption capacity (displacement) of the weld, like in crash-prone zones of vehicles [106][110][111]. Tensile-shear test is the most common static test [10]. The tensile performance of spot welds is defined by three key factors: the maximum load to failure, the mode of failure, and the minimum button size required to avert interfacial failures [4]. Tensile shear load and failure energy absorption show a direct relationship with nugget size [4][61], with performance initially improving as the nugget diameter increases. However, beyond an optimal size, excessive melting, electrode indentation, and splashing can reduce the effective weld area, leading to a decline in tensile-shear force and compromising the overall weld quality [65]. For lap-shear samples, the strength of spot welds increases linearly with the BM strength up to a certain point, after which the rate of increase diminishes, reflecting a hierarchy of T-S load and energy absorption from DP600 to DP980, influenced by material strength and HAZ softening [4][108].

During a tensile-shear test, dominant shear stresses parallel to the weld interface lower than the tensile strength make the test highly prone to interfacial failure, with the fracture path propagating through the FZ, characteristic of this failure mode regardless of the fusion-zone size [23][70][100]. The outcome of T-S depends on which stress shear at the interface or tensile at the circumference reaches its critical value first [4]. *Figure 3.3* illustrates the assumed stress distribution around the weld nugget for a lap-shear sample. The stress is described as a harmonic tensile stress distribution, characterized by its alignment with the loading direction. The maximum tensile stress occurs at the edges of the nugget circumference (at specific angles of 0° and 180°). The figure highlights that the stress diminishes symmetrically as the angle diverges from these points, reflecting the strain-hardening behavior and deformation patterns of the material [106].

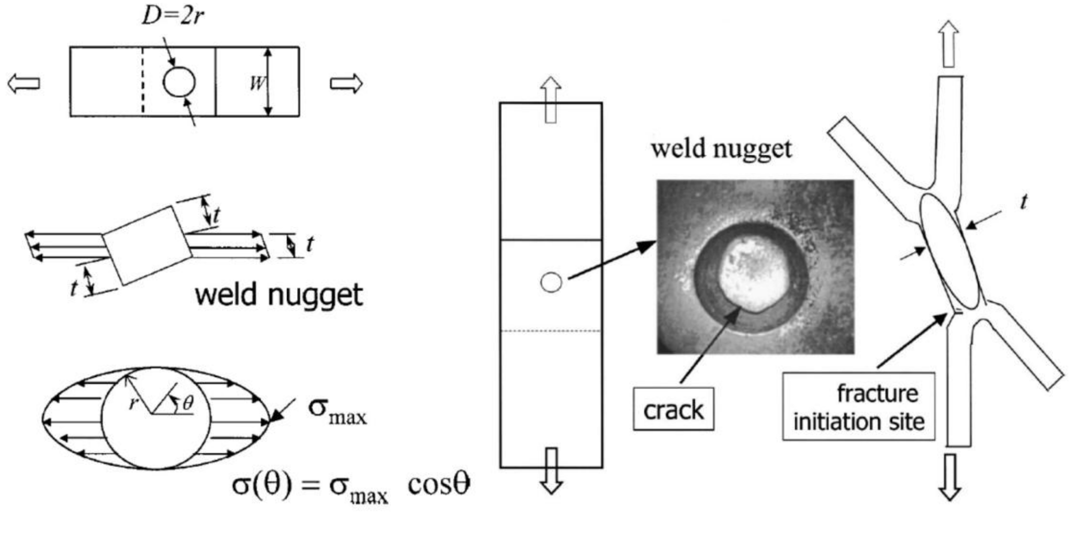

Figure 3.3. Stress distribution around the weld nugget in a lap-shear sample & Fracture initiation site of a lap-shear spot-weld sample [106].

Figure 3.3 emphasizes that while the global loading is shear, the failure mechanism at the material level is tensile, driven by concentrated stresses around the weld nugget's perimeter. The global deformation and failure process of a lap-shear spot-weld sample progression is divided into four stages, initial configuration which the lap-shear sample begins in its original, undeformed state, with the two metal sheets joined by the weld nugget, nugget rotation, necking, and tensile fracture. Crack propagation has begun along the circumference of the weld nugget, with the fracture extending (see *Figure 3.3*) [106]. The visible rotation of the FZ during tensile-shear loading highlights a complex stress state, where shear-tensile stresses at the nugget circumference transform into tensile stresses [101], inducing plastic deformation through the sheet thickness, emphasizing the critical roles of both the HAZ and BM in determining overall weld strength [23].

Failure in spot welds during quasi-static tensile-shear tests consistently initiates in the SCHAZ and varies with steel grade, with DP600 tending to fail in the BM due to its lower hardness compared to other weld regions, However, higher strength steels like DP780 and DP980 experience HAZ softening during welding, leading to failure in the softened HAZ region [4][23]. These differences in failure location are attributed to the hardness profile characteristics of the weld, with necking typically occurring at the point of lowest hardness. The dominant failure mechanism in these tests is through-thickness necking [23]. Welds produced by 2-pulse RSW exhibited a remarkable 15.6% increase in peak load and an impressive 83.1% enhancement in failure energy during tensile shear tests [112].

3.3. *Dynamic tests*

3.3.1. High cycle fatigue (HCF) of RSW

Fatigue in vehicle components arises from time-varying loads induced by road irregularities and vehicle dynamics. These stresses lead to the accumulation of damage over time, ultimately resulting in crack initiation and failure, especially in joints like spot welds [102][113]. Therefore, the spot weld quality in the context of fatigue is very important to ensure the vehicle's integrity and durability [95]. Higher yield strength materials demonstrate superior fatigue performance in the low-cycle fatigue regime by resisting plastic deformation and distributing stress more effectively around welds [90][114][115][116]. Advanced high-strength steels (AHSS) high-cycle fatigue (HCF) behavior is similar to conventional steel [115][116] as crack growth rate becomes the dominant factor [114]. The microstructure-driven fatigue performance of resistance spot welds is predominantly influenced by stress concentration and notch sensitivity rather than the base material's strength, with high-cycle fatigue behavior remaining largely consistent across different steel grades due to shared crack initiation and propagation mechanisms [90][115][116][117][118][119][120][121][122][123]. For instance, fatigue tests were conducted on spot-welded joints made from mild steel (270 MPa grade) and ultra-high tensile steel (980 MPa grade). The results revealed that, in the high-cycle fatigue regime, the differences in fatigue performance between the two materials diminish, with their fatigue limits becoming nearly identical. This observation suggests that the notch sensitivity of the steel's fatigue strength plays a significant role in determining how the strength level of the steel influences the fatigue behavior of spot-welded joints [116].

The microstructure of dual-phase steel, particularly the volume and distribution of martensite within the ferrite matrix, plays a crucial role in fatigue performance by influencing crack initiation and stress distribution, with increased martensite content generally enhancing fatigue life under cyclic loading [62][124], though excessive martensite, especially in welded regions, can lead to stress concentrations and microcrack formation, affecting overall durability [121][118]. The nugget's high hardness (due to martensite formation) makes it brittle and susceptible to crack propagation once initiated [64]. On the other hand, research has found that the microhardness in the HAZ does not significantly affect fatigue performance under tensile-shear conditions [114]. Despite notable differences in HAZ hardness or base metal between materials HSLA and MS1300, the fatigue curves remain consistent [125].

In dissimilar material joints, fatigue cracks tend to initiate in the stronger base metal due to stress concentration at the sheet interface, where the sharper notch in the harder material amplifies localized stresses, leading to crack initiation and propagation [122][126]; this effect is particularly evident in ultra-high-strength steels, where notch sensitivity and cyclic loading shift failure locations, highlighting the dominant role of geometric and mechanical mismatches over microstructural hardness in controlling fatigue behavior [122].

The fatigue life of spot-welded joints is influenced by factors such as joint type, load amplitude, sheet thickness, and weld nugget size, with larger diameters and thicknesses generally improving fatigue performance by reducing stress concentration [90][95][102][114][115][117][118][127][128]. Optimizing weld nuggets to produce Larger and more uniform weld nugget diameters through higher welding currents and electrode geometry significantly enhances fatigue life by reducing stress concentration and improving load distribution [22][64][90][113][126][129], while larger electrode tip diameters further influence weld characteristics by characterise the notch geometry [119]. Materials with similar weld geometries exhibited nearly identical fatigue performance, confirming the overriding influence of geometric factors over material microstructure or strength in high cycle fatigue [90].

HCF Fatigue cracks in resistance spot welds predominantly initiate at stress concentrations around the weld nugget edge and sheet interface, where sharp geometrical discontinuities act as natural notches [22][53][62][90][115][117][123][126][127][130], where stresses often exceed the material's elastic limit, causing microplastic deformation that leads to crack initiation and propagation under complex loading conditions like mixed-mode shear and cross-tension [131]. Unlike low-cycle fatigue (LCF), where significant plastic deformation can dictate crack initiation in the base metal, HCF primarily involves elastic deformation [115]. Fatigue cracks in resistance spot welds typically initiate at stress-concentrated areas, such as the weld nugget's edge or sheet interfaces, with notches and stress concentrators playing a critical role in reducing fatigue resistance by amplifying localized stresses and accelerating crack initiation under cyclic loading [53][102][114][115][117][121][130][132][133][134][135][136]. Weld geometry, particularly notch shape and weld nugget size, plays a crucial role in HCF, while notch sensitivity significantly influences the fatigue strength of spot-welded joints, especially in the high-life region where fatigue limits become comparable to mild steel [115] [116].

In high-cycle fatigue, the crack growth path in resistance spot-welded joints is dictated by stress concentrations and microstructural heterogeneity, with cracks often initiating in softened HAZ before propagating along paths of least resistance influenced by local mechanical properties [115]. Fatigue cracks in DP780 typically initiate at stress concentration points, amplified by microstructural features like grain boundaries and phase interfaces, where localized stresses arise from the interaction between ferrite and martensite phases [124]. A study examines different microstructures of high-strength steels, including ferritic, martensitic, and dual-phase structures. Each microstructure presents unique characteristics that can affect both toughness and strength thus notch sensitivity [137].

Crack initiation and propagation in welded joints are governed by localized stress concentrations and microstructural heterogeneities, with fatigue cracks often originating at weld interfaces or notch tips due to metallurgical differences, while their growth path follows regions of reduced fracture toughness, such as tempered martensitic zones in the HAZ, particularly under cyclic loading conditions [64][95][124][126][129][138][139]. The maximum stress concentration occurs due to the weld nugget geometry and notch effect under cyclic tensile-shear loading [133]. *Figure 3.4*a illustrates the focal point of stress distribution, where normal stress (σx) and transverse shear stress (τ) interact across the sheet thickness (t), with stress concentrations near the nugget's edge; additionally, *Figure 3.4*b illustrates the structural stress components membrane stress (σm), uniformly distributed across the thickness, and bending stress (σb), exhibiting a gradient due to bending moments [127]. The interplay between tensile, shear, and bending stresses creates a high stress concentration, this explains why fatigue cracks often initiate in these regions during cyclic loading [64].

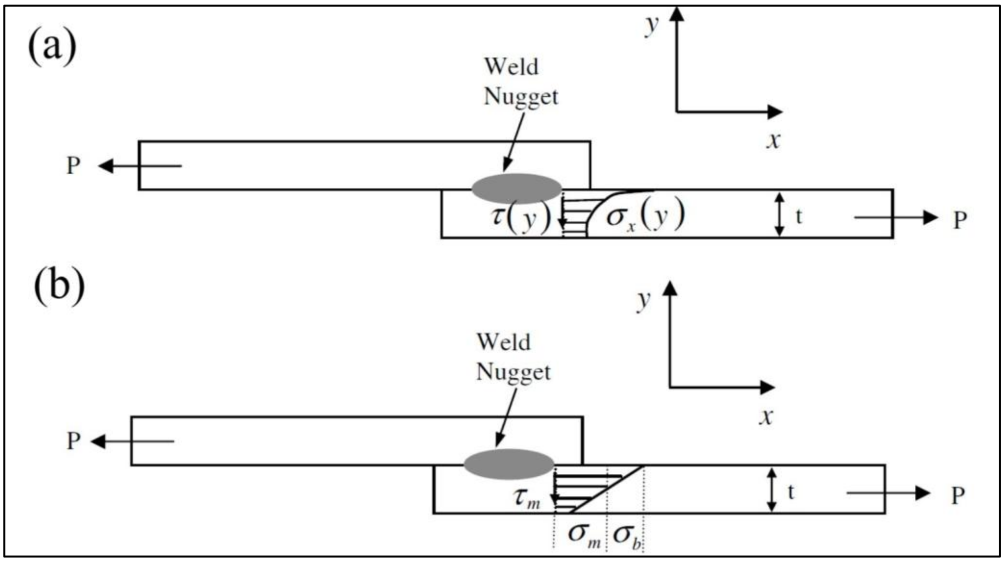

Figure 3.4. Structural stress definition at the edge of spot weld nugget [127].

Fatigue life is significantly influenced by weld notch geometry, with larger nugget diameters and optimized notch root angles enhancing stress distribution and resistance to cyclic loading [140][141], while increased joint angles, smaller notch radii, and sharper notches elevate stress concentrations, accelerating crack growth and reducing fatigue performance [102][114][131][133]. Materials with high notch sensitivity, typically characterized by a high yield-to-tensile strength ratio (Y/T), exhibit limited ductility and are more prone to fatigue crack initiation at notch roots due to increased localized stress, whereas low notch-sensitive materials with greater ductility resist crack initiation and instead experience fatigue dominated by crack propagation [142]. Thus, a material's strength significantly impacts its notch sensitivity, with higher-strength materials generally showing increased notch sensitivity, especially under conditions of high stress concentration or limited ductility [142]. Fatigue strength was consistent across all material combinations regardless of the strength of the softer steel. In tensile shear and cross-tension modes, cracks consistently initiated and propagated on the UHSS side, emphasizing the influence of its notch sensitivity [122].

Fatigue failure in spot-welded joints progresses through distinct stages of crack initiation, propagation, and fracture [138][143]. While AHSS provides advantages in specific fatigue scenarios, its performance in HCF crack propagation aligns closely with traditional steels, as the geometrical stress concentrations overshadow material-specific characteristics in dictating the crack growth path [115]. The cracks propagated through fatigue striations, a characteristic feature of fatigue failure, indicating that the cracks grew incrementally with each load cycle [53][126]. Fatigue cracks in welded joints predominantly initiate at stress concentration points within the HAZ or FZ, propagating perpendicularly through the sheet thickness and extending in eyebrow shape outward along the weld nugget or base material, with crack pathways influenced by material properties, weld geometry, and cyclic loading conditions [27][53][62][90][102][114][115][117][121][122][129][132][136][143].

Figure 3.5 illustrates HAZ fatigue failure depicted by its distinct radial crack propagation pattern. The cracks in HAZ failure start near stress concentrators such as notches, propagating outward from the nugget in a direction perpendicular to the applied load. Progress through the material rather than around or through the nugget. This failure mode typically involves a combination of brittle and ductile fracture mechanisms. This failure mode is more common under moderate fatigue loads, where the stress distribution promotes crack initiation and propagation within the HAZ rather than the nugget itself. The microstructure analysis of the TRIP980 failure mode shows that the HAZ comprises tempered martensite or a mix of ferrite and bainite [62]. A study found that the opening between two sheets (notch) in the nugget-surrounding area acts as an initial crack due to stress concentration [64]. The notch root radius plays a significant role in determining the stress concentration at the spot weld. A smaller radius typically results in higher stress concentration, which can affect the fatigue life and failure resistance of the weld [144].

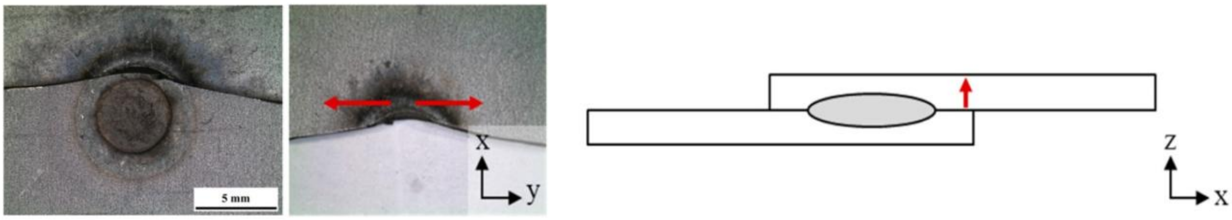

Figure 3.5. Crack propagation direction (red arrow) with HAZ failure mode [62].

Eyebrow shape fatigue failure in resistance spot welds occurs primarily in high-cycle fatigue conditions, where cracks initiate away from the weld nugget and propagate linearly through the base metal without significant deformation, emphasizing the role of base material properties and stress distribution in fatigue performance [102][129]. *Figure 3.6* shows different types of HCF failure mechanisms observed in DP980 steel under cyclic loading of welds at different maximum cyclic load levels. In the eyebrow shape failure, the fracture was observed along the width of the sheet in the direction perpendicular to the loading direction. Only, the base metal failed, and the nugget was intact. While in the partial plug failure, the fracture was noticed along the circumference of the nugget up to some extent before crack propagation in the width direction and the weld nugget was fractured partially [129].

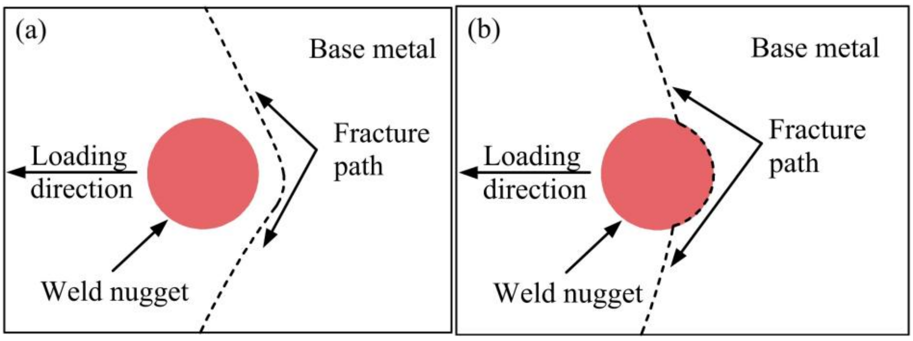

Figure 3.6. HCF failure: (a) Eyebrow shape failure, (b) Partial plug failure [129].

The HCF behavior at low loads exhibited similarities across all conditions despite variations in overload weld strength, cracks at lower loads (approximately 20% of yield load), they traveled along the fusion boundary, weak HAZ, and BM, culminating in a transition in failure mechanisms and fracture modes around 50% of yield load [95]. In DP600 steel at lower loads, fatigue cracks initiate in the HAZ near the FZ boundary and sheet interface, cracks initiate at the nugget boundary, penetrate the thickness, and propagate perpendicularly to the loading direction through the BM where theoretical stress analysis reveals maximum triaxial stresses [64].

Rayan. W Rathban reveals in his dissertation that fatigue cracks consistently initiate at an oxidized structure on the weld periphery, referred to as the "tongue." This tongue forms during the welding process when molten material is expelled and solidifies along the sheet interface. This structure, which is globular in shape and partially bonded to the base material, creates a weak interfacial region prone to crack initiation under cyclic loading. *Figure 3.7*a illustrates the schematic of the fatigue fracture path in a spot weld, breaking it into three distinct regions: A, B, and C. The crack initiates at the interface between the tongue structure and the base material, labeled as point "A" At this stage, the crack propagation occurs along the tongue-sheet interface but eventually shifts to penetrate through the thickness of the sheet. At point "B" the crack propagates parallel to FZ, and at point "C" the deviation in the crack path is due to changing stress distribution as the crack grows. This directional change is driven by the crack aligning perpendicular to the applied load, which increases the tensile stress at the weld, especially under bending moments [90]. *Figure 3.7*b shows the fatigue fracture line of the 590TRIP steel RSW welded in 8.4 kA current and 3.9 kN electrode force. The fatigue fractures predominantly started at the notch and tongue in the outer nugget surface, where stress was concentrated [22].

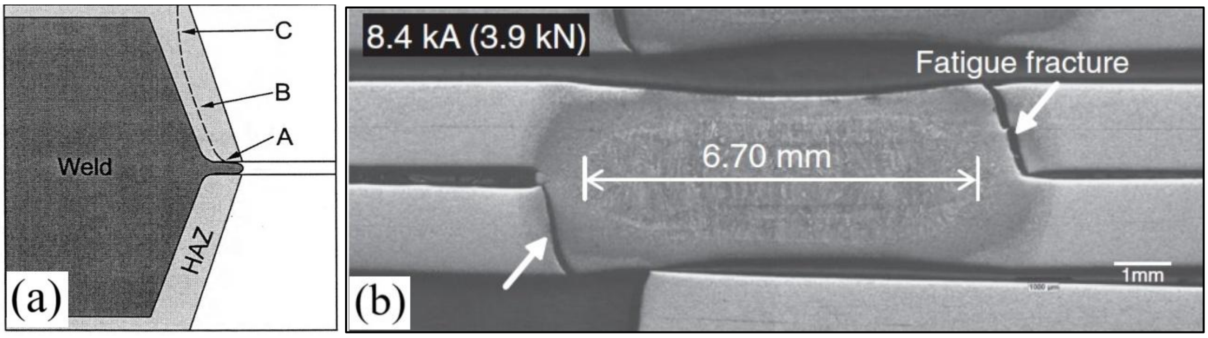

Figure 3.7. (a) Schematic of the fatigue fracture in HSS RSW [90], (b) Fatigue fracture [22].

3.3.2. HCF analysis method

The JSME S 002-1981 standard, established by the Japanese Society of Mechanical Engineers, outlines a methodology for conducting fatigue tests on materials, particularly focusing on HCF. Primarily used in industries where high-cycle fatigue is prevalent, such as automotive and aerospace applications, focusing on materials tested under controlled laboratory conditions [145][146]. Since HCF test results have greater uncertainty, standard deviation, and lower reliability than static test results [147], the JSME S 002-1981 staircase method, is a statistical approach used to determine the fatigue limit (endurance limit) of a material utilizes a 14-specimen [148].

It is commonly used in high-cycle fatigue testing, where stress levels are adjusted in fixed increments to systematically determine the fatigue limit of the material [148].In fatigue testing, the fatigue life at a given stress level follows a log-normal distribution due to natural material variability. The standard deviation (SD) measures how much fatigue life data points vary around the mean curve. A higher SD indicates greater variability, meaning fatigue life is less predictable. *Figure 3.8* shows the staircase method of the HCF strength curves *(*S-N) diagram used in fatigue analysis, the diagram illustrates multiple stress levels, denoted as $\Delta\sigma_0$, $\Delta\sigma_1$, $\Delta\sigma_2$, and so on, which represent different applied stress ranges in fatigue testing.

The black curve, labeled "Mean", represents the mean S-N curve, which is derived from fatigue tests conducted at different stress levels. This curve provides an average estimate of a material's fatigue life based on experimental data. The fatigue limit section of the limit curve represents the fatigue limit value, which is determined using the average stress levels of the surviving specimens in cases where specimens did not fail. This approach ensures that the calculated fatigue limit reflects the material's endurance properties based on experimental results. However, for design safety, engineers do not rely solely on the mean curve. To account for variability in fatigue performance, the red curve, labeled "Mean - 2SD", represents a statistically lower-bound curve that is positioned two standard deviations below the mean S-N curve. The gap between the black and red curves represents the statistical reduction (2SD) applied to the mean fatigue strength.

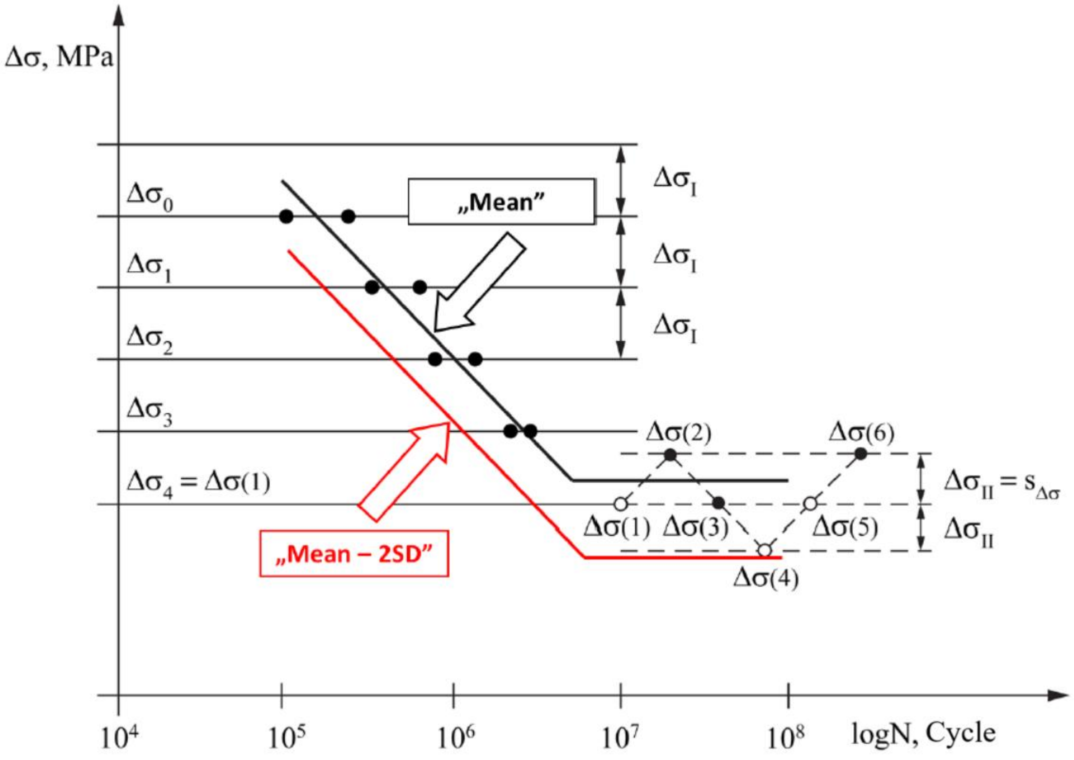

Figure 3.8. Staircase method of HCF strength curves, „Mean-2SD" S-N curves [149].

To minimize bending and misalignment during tests, two shims (spacers) of the same thickness as the specimens were added at the grip sections to ensure proper alignment and reduce any potential sheet deformation [63][10]. Improper welding parameters can lead to solidification voids or cracks with characteristic dendrite microstructures, resulting in interfacial fracture under static or cyclic loading [64]. Peak load and energy absorption capability, as fatigue tests indicate a slightly lower fatigue limit for specimens affected by expulsion, ultimately compromising weld integrity [10][63][64]. As expected, fatigue life increases with decreasing fatigue load, following a well-established trend in materials science [62].

A study evaluated the spot weldability and fatigue behavior of M190 martensitic steel by comparing its performance with DP steel through tensile shear-type specimens subjected to tension-tension sinusoidal loads, where a load ratio (R) of 0.1 indicates that the minimum load is 10% of the maximum load in each cycle [95], revealing that HCF behavior is primarily influenced by stress field parameters rather than material strength or microstructure for the steels examined [90][95].

Surprisingly, welding current had minimal impact on fatigue life within experimental scatter, though samples welded at 8.54 kA showed a slightly lower fatigue limit (see *Figure 3.9*a) [64]. FZ size affects the tensile strength and fatigue life of the welds. A study showed that specimens welded with larger electrode face diameters (10 mm) exhibited superior fatigue life under higher loads, as their larger nugget size enhanced load-bearing capacity and minimized stress concentration, enabling them to sustain double the fatigue limit load of smaller electrode specimens (8 mm) over 2 million cycles (see *Figure 3.9*b) [62].

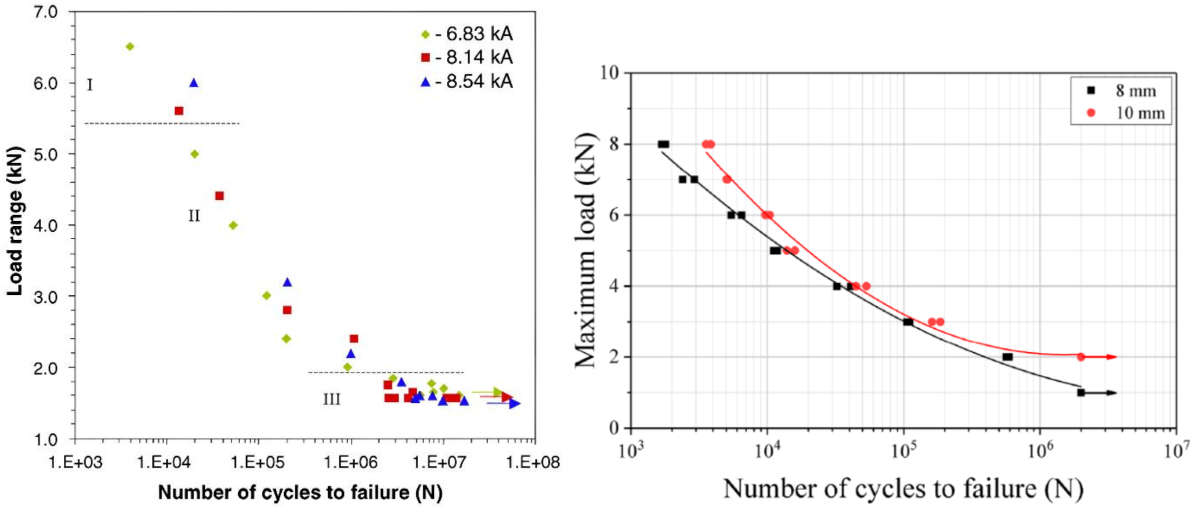

Figure 3.9.(a) Load-Number of cycles to failure curves of different welding currents, (b) Load-Number of cycles to failure curves of different electrode sizes.

3.3.3. Instrumented impact testing of RSW

Over the years several impact testing methods have been developed for spot welded joints for example the drop-weight system, pendulum impactor, and high-speed servo-hydraulic equipment [150][151][152][153][154][155][156][157]. Hammer-type (striker) impact testers (like Charpy) can be used for smaller cross-sections, such as RSW joints. The Charpy impact test is regarded as one of the most frequently used tests to evaluate the relative toughness of a material in a fast and economical way [158]. The Charpy impact test is a standard test to measure the impact energy (also referred to as notch toughness) absorbed by a material during fracture. The notch provides a point of stress concentration within the specimen and improves the reproducibility of the results [159]. The absorbed energy is computed by working out the potential energy lost by a pendulum by breaking a specimen [159]. In the early 1970s, French researchers developed test methods for the dynamic testing of thin plates [160]. The test is essentially a dynamic impact test. The maximum kinetic energy of the impactor is 300 J.

The emphasis on safety aspects became increasingly important (such as compliance with increasingly stringent fracture tests), and the automotive industry needed to dynamically test welded joints in thin sheets in addition to testing sheet materials, so research has continued in this direction. In the mid-1990s, Kaplan's team in Paris further developed the Grumbach test design. That new method was already suitable for the dynamic testing of spot-welded joints from 0.5 - 5 mm thin plates, and the maximum kinetic energy was increased to 450 J [161]. The new method was called the impact tensile crash test. The aim of the developers was to perform the test under industrial conditions and to get as close as possible to the processes that take place during real crash tests [158]. There is no notch in the thin-plate specimen containing the spot-welded joint.

This is because, during the design of the test specimen, the developers assumed that the spot-welded joint would serve as a stress concentration point, so no separate notch was required. However, with this specimen design, the dynamic behaviour of the larger material around the joint is also investigated. This means the dynamic characteristics of the whole structural element containing the welded joint can be determined, thus simulating the processes that take place during an actual collision [158][162]. The developed specimen design is shown in *Figure 3.10*.

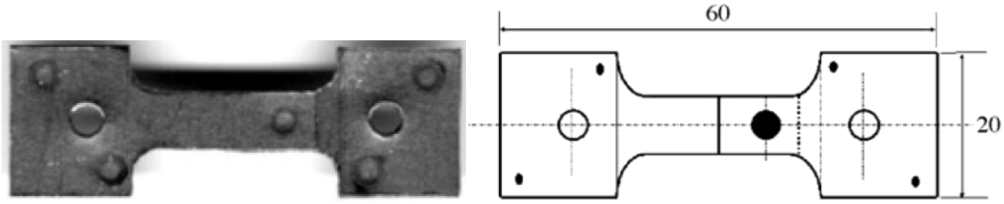

Figure 3.10. Developed impact-tensile specimen for RSW joints [163].

The principle of the test has not changed, and the specimen is still subjected to dynamic impact tensile loading. *Figure 3.11* illustrates the fixation of the specimen, the direction of loading, and the test setup.

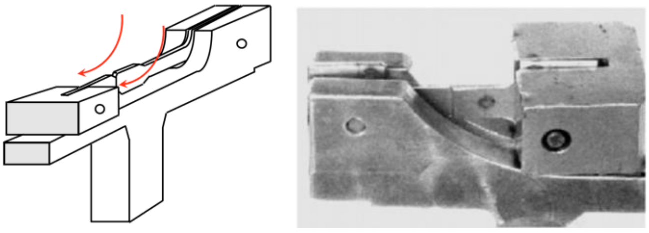

Figure 3.11. The fixation of the specimen to the special specimen holder [163]

The 1995 version was upgraded in 2003 the specimen size was increased, the hammer was redesigned, and the impact energy was increased to 750 - 800 J [161]. The new developments are shown in *Figure 3.12* and *Figure 3.13*.

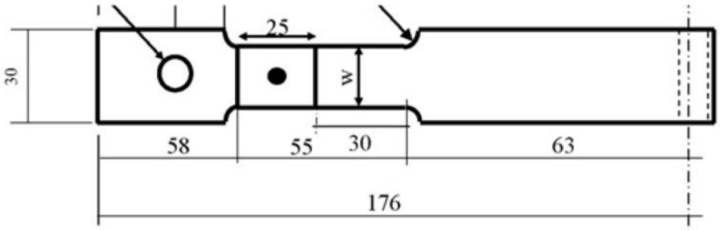

Figure 3.12. New geometry specimen with larger dimensions [158]

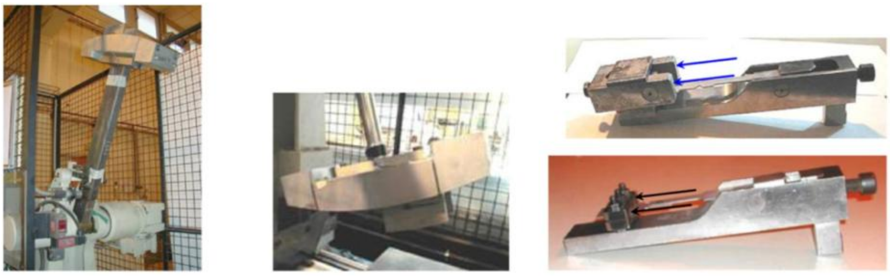

Figure 3.13. The redesigned hammer and specimen holder [158]

The impact energy characterization of RSW specimen enhanced with additional instrumentation setup is designed to extract detailed mechanical data during impact testing. This approach often involves strain gauges mounted on the striker and a velocity measurement system to measure the load-time behavior as the specimen undergoes deformation and fracturing. *Figure 3.14* shows the instrumented setup of impact testing.

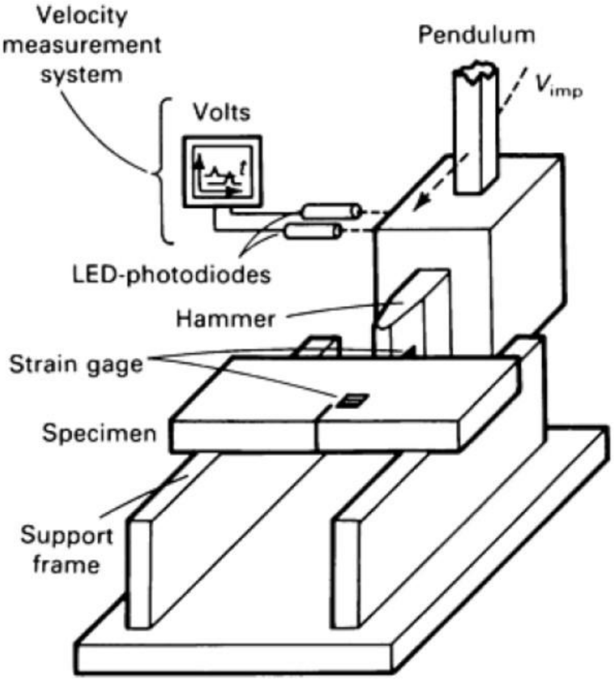

Figure 3.14. Instrumented Charpy impact testing setup

The results of the performed dynamic tests and fracture tests showed that the failure mode of RSW joints of AHSS are very often interfacial or are only partial weld pull-out. This is presumably due to the fact that the welding parameters to be used during production are chosen on the basis of the results of conventional, quasi-static tests (shear-tensile, cross-tensile, peel, etc.) [158]. During the quasi-static test, the joints are still pull-out, but they already show a less favourable failure mode due to dynamic loads. Besides these, the developed impact test methods for RSW joints are investigating the impact-shear or impact-tensile properties, which do not perfectly show the behaviour of spot welds in case of real impact effect. Typically, the side parts of a car chassis during a car crash suffer impact-bending. The impact velocity range can be very variable; in the case of low-speed car crash simulations it is less than 10 m/s [164]. The stress condition near the FZ is three-dimensional and very complex in a spot-welded specimen. Furthermore, the strain rate near the spot weld could be very high under ordinary vehicle collision speed, for example, the local strain rate can reach 3500 1/s at 6 m/s impact velocity [165]. For higher impact velocity, more and more researchers are using a ballistic test of spot welds, where the impact velocity is more than 100 m/s [73]. Nowadays several data sets have been published about strain rates and their complexity [166][167].

4. HEAT-CYCLE MEASURING (HCM)

4.1. Introduction

Understanding the thermal history of RSW technologies is crucial for interpreting the microstructural changes that occur during welding [144]. The cooling rate in addition to composition significantly impacts the microstructure and properties of UHSSs [168].

The temperature-time relationship is fundamental to understanding the weld's microstructural development, particularly the formation of martensite during cooling and its tempering [59]. The HAZ exhibits a gradient of microstructural variations resulting from the differing peak temperatures and cooling rates experienced across its sub-zones during the welding thermal cycles [10][61].

During RSW, the steel is rapidly heated to temperatures above its melting point in the FZ followed by subsequent rapid cooling, which occurs primarily through heat dissipation to the electrodes [43]. Heat dissipation in RSW involves conduction, where heat spreads through the metal sheets and welding electrodes influenced by their thermal conductivity; convection, which can be applicable if a water-cooling system is applied in electrodes; and radiation, which plays a minor role but can contribute to heat loss at higher temperatures [169]. *Figure 4.1* shows a scheme of heat dissipation mechanisms in RSW.

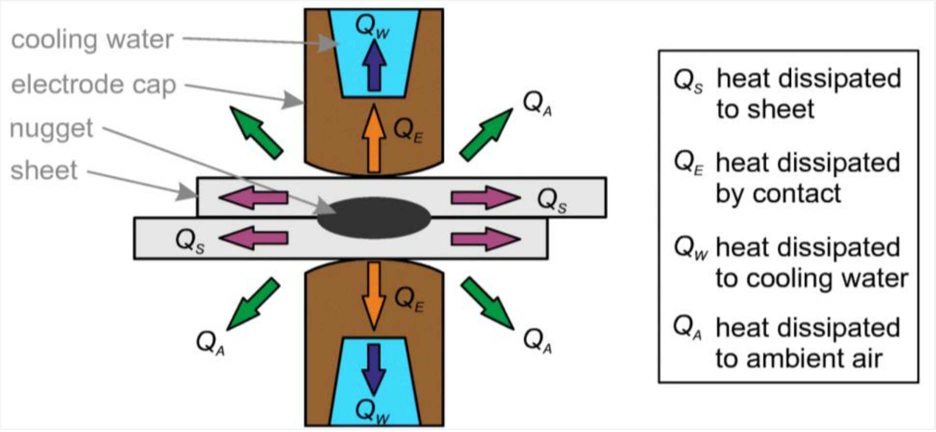

Figure 4.1. Schematic illustration of heat dissipation in RSW[169] .

After the current stops, the FZ starts to solidify and cool. The cooling rate in RSW can vary widely depending on several factors, including material properties, thickness, welding parameters, and environmental conditions. For many steels, especially high-strength steels used in automotive applications, the cooling rates in RSW can range from 10^3 to 10^4 °C/s [170][19].

The heat cycle in RSW creates temperature gradients across the weld zone, with FZs being the hottest and decreasing temperatures outward. Expulsion can disrupt these gradients, causing non-uniform cooling measurements [171]. Expulsion in RSW has a pronounced effect on the heat cycle of the process. Instantaneous temperature drops when the expulsion occurs because of increasing the contact area between the sheets being welded thus resistance may drop. This results in an instantaneous loss of heat since the expelled metal carries away a significant amount of thermal energy [19].

Both LC and HC welds show similar peak temperature distributions across their weld zones [68]. Increasing the thermal conductivity of the sheet increases the cooling rate, as materials with better thermal conductivity dissipate heat more rapidly; however, thicker sheets experience a slower cooling rate due to the greater distance from the electrodes [43]. In addition to the sheet thickness the general cooling rate is significantly influenced by factors such as water-cooled copper electrodes, and a short welding cycle [10].

Spot welds in sheets up to 2 mm thick exhibit extremely rapid cooling, solidifying within 3-4 cycles at rates ranging from ~2000°C/s for 2.0 mm sheets to over 100000°C/s for sheets under 0.5 mm thick, with 1.25 mm DP600 steel cooling at ~6000°C/s significantly exceeding the 40-120°C/s required for martensite formation in DP steels [64]. A study found the critical cooling rate for DP600 steel is around 60 °C/s; thus, the actual cooling rate far surpasses this critical threshold, facilitating martensitic transformation in the fusion zone [10]. A study has shown welding process, the cooling rate was estimated at 2762°C/s in the critical temperature range of 549-273°C, far exceeding the 100°C/s threshold for full martensite formation [59]. Moreover, the extremely high cooling rates, exceeding 400°C/s, prevent carbon diffusion and promote martensite formation [70].

The cooling rate is typically very high, with $\Delta t_{8/5}$ (cooling time from 800°C to 500°C) ranging from 0.05 to 0.15 seconds for sheet thicknesses of 0.8 to 2 mm [43], which is less than the 3 second threshold for martensite formation [14]. The cooling process in welding involves an initial rapid temperature drop of over 1000°C within 0.1 seconds, followed by a slower decline below the martensite finish (M_f) temperature (~300°C), with a minimum cooling time of 0.4 seconds ensuring a complete martensitic transformation and sufficient heat retention for tempering while preserving enough heat for tempering, with longer times up to 0.58 seconds offering diminishing returns due to slower cooling rates [59]. Varying the second pulse current in a pulsed RSW schedule can modify the weld thermal cycle and alter cooling rates during welding [58].

4.2. Heat cycle modelling of RSW

Numerical and analytical modeling is frequently used to calculate the thermal cycles [76][77] [172][173]. For example, an analytical calculation suggests that the thermal cycle is extremely fast with the cooling rate reaching up to 4000 °C/s [98][174]. FEM simulations were applied to investigate the thermal cycles of RSW, and experimental techniques for correlating welding parameters with thermal history, microstructure, and mechanical properties [59]. For instance, Finite element analysis (FEA) effectively simulated the RSW welding process, revealing a maximum cooling rate at the center of the FZ, notably, cooling rates decreased with distance from the FZ center, towards the SCHAZ [86]. FEA effectively simulated the RSW process, revealing a maximum cooling rate of 22715°C/s at the center of the FZ, cooling rates decreased with distance from the FZ center, with the (UCHAZ) averaging ~2772°C/s, the (ICHAZ) ~2082°C/s, and (SCHAZ) ~1488°C/s [86]. A temperature modeling profiles for FZ, CGHAZ, and ICHAZ illustrated that peak temperatures exceed 1600°C, 1100-1300°C, and 730-900°C respectively [58]. Ensuring the simulation results align with experimental outcomes is critical for building confidence in predictive models. However, discrepancies between simulated and actual results can arise from simplifications made during modeling, inaccuracies in input data [175][176], or due to severe conditions that may not be validated experimentally like melted weld metal [177].

SYSWELD is a FEA software, designed specifically for simulating various welding processes, including RSW. It integrates multiple physical phenomena such as thermal, metallurgical, and mechanical behaviors to provide a comprehensive analysis of the welding process, thus facilitating the optimization of welding parameters and sequences [178]. This holistic approach enables accurate predictions of weld quality and structural integrity. The software includes an extensive material database covering base metals and welding electrodes, which aids in selecting appropriate materials for specific applications [178]. The simulation of RSW involves modeling the heat generation due to electrical resistance as well as the mechanical forces acting on the materials being joined.

Combining the numerical simulation with experimental research provides a very valuable method for welding process parameters recommendation to get sound welding joints in actual production [229]. *Figure 4.2* shows a visual representation of the validation framework for the numerical models employed in RSW simulations.

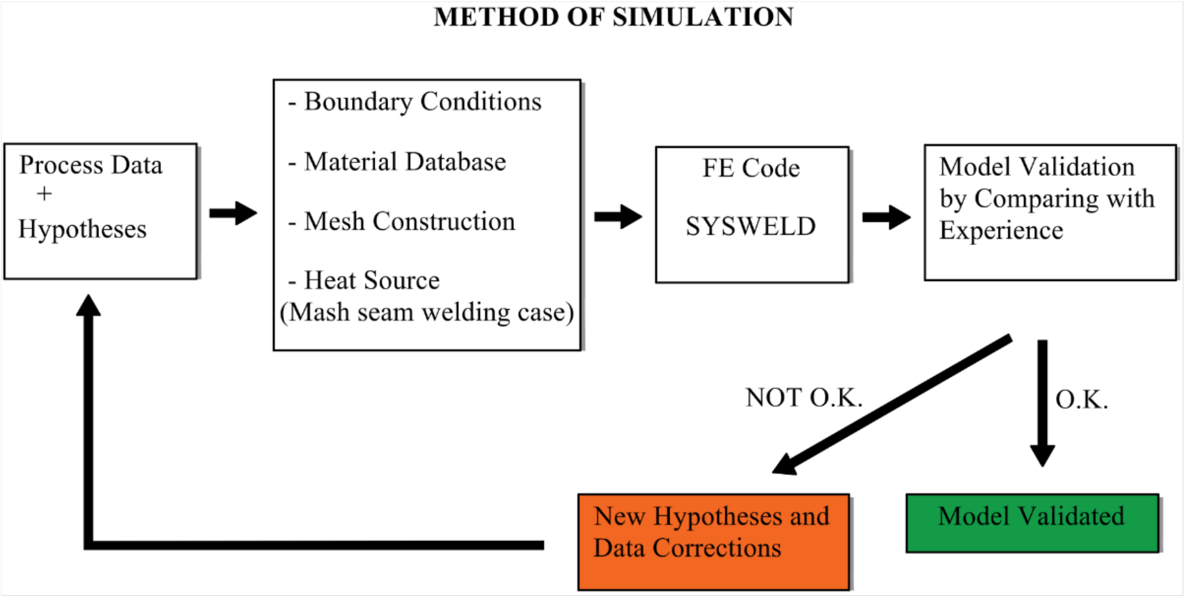

Figure 4.2. RSW simulation methodology of FEM software [177].

The researchers validated their FEM against experimental data, confirming its accuracy in predicting microstructural evolution and temperature distributions [96]. Research has shown that using SYSWELD for RSW simulations can significantly reduce design errors and improve product quality by allowing engineers to visualize potential issues before physical prototyping [179][180].

The main methods for simulating the RSW process are thermal models, electro-thermo-mechanical models, electro-thermal models with fluid flow, and Electro-thermal models combine electrical and thermal properties to show how electrical current influences heat generation within the workpieces. The models incorporate temperature-dependent properties of materials and simulate how heat affects the FZ formation and overall weld integrity [181].

The simulation software allows for the analysis of time-based temperature changes providing comprehensive thermal analysis and temperature-time profiles [182]. Modeling the RSW process requires accounting for complex thermoelectric behavior and carefully defining parameters, including boundary conditions, applied voltage, current load, electrode force, and varying convection coefficients to simulate environmental and cooling water effects accurately [15]. The meshing strategy aimed to balance accuracy and computational efficiency. The mesh density should likely be refined in areas with higher thermal gradients, such as the FZ and the HAZ regions, to capture detailed temperature distributions [183]. Continuous advancements in simulation techniques and validation methods will enhance the effectiveness of RSW simulations using SYSWELD in practical applications.

4.3. *Physical heat-cycle measurement of RSW*

Measuring the exact temperatures in RSW is quite challenging [184] due to the rapid thermal cycle, high welding currents that generate strong electromagnetic fields, and small vibrations. Thermocouples are common instruments used to measure temperature changes in the function of time during welding in heat-affected sub-zones. The data obtained from the measurement can be used to determine the peak temperature reached during the welding, the heating, and cooling rates, and the time spent at specific temperature ranges. The size of FZ and properties can be inferred from the temperature-time profile [19][185]. The AC current and associated electromagnetic fields can introduce electrical noise into the thermocouple readings in RSW. This noise might distort the actual temperature signal. Induced eddy currents and magnetic field effects can cause mechanical vibrations in the electrodes and workpiece [186]. Noise can be mitigated by using shielded thermocouple wires, placing the thermocouple away from areas with high magnetic fields, and using digital filtering techniques [187]. A detailed study of RSW on DP600 steel used three type K thermocouples positioned at 2.9, 3.5, and 4.3 mm from the weld spot to capture thermal cycles on the surface of RSW HAZ subzones (see *Figure 4.3*), revealing peak temperatures of ~900°C in the HAZ and below 600°C at farther locations, corresponding to the BM or HAZ-boundary. The rapid heating and cooling rates in the HAZ, exceeding 400°C/s, drive martensite formation, creating distinct microstructural zones influenced by significant temperature gradients (see *Figure 4.3*) [70].

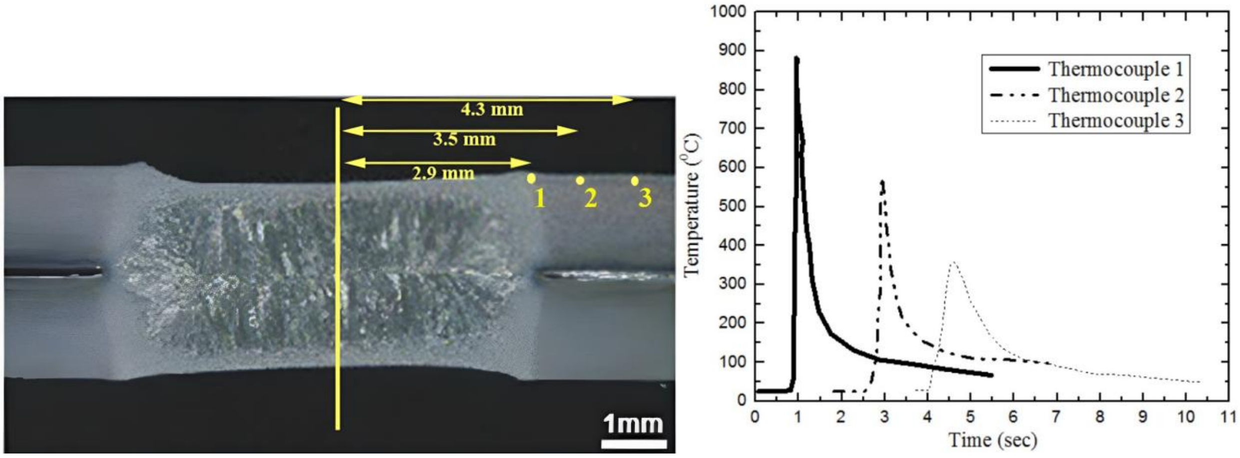

Figure 4.3. The location of the thermocouples & Temperature history of different thermocouples [70].

Z. Han et al. conducted an experimental validation of a heat transfer study on RSW. The temperature measurements were taken using thermocouples embedded into machined open slots positioned within the HAZ [185]. While this setup allowed precise monitoring of temperature changes during welding, it had a notable disadvantage. Since the slot was open to the air, heat could dissipate more quickly than it would in a real welding scenario.

5. RSW SAMPLE PREPARATION

5.1. Introduction

The integrity and reliability of RSW, a crucial process in various manufacturing industries, are significantly influenced by the quality of sample preparation. Geometrical deviation in RSW refers to the variations in the dimensions and positions of welds that occur during the welding process. These deviations can significantly impact the quality and structural integrity of the welded assemblies, particularly in precision-dependent industries like automotive manufacturing. To achieve consistent and reproducible results, it is crucial to meticulously control all welding process variables so the testing process and the temperature conditions must be the same in all samples. The quality of a spot weld is often evaluated based on the size and integrity of the FZ.

5.2. RSW electrode misalignment

Misalignment of the electrode or inconsistencies in electrode force can lead to irregularities in the nugget formation. These irregularities can complicate the measurement of nugget diameter, which is a critical parameter for assessing weld quality [188]. Electrode misalignment can significantly impact the quality and performance of RSW. Misalignment occurs when the contact surfaces of the upper and lower electrodes are not parallel (axial misalignment) or when their centers are not coincident (angular misalignment) (see *Figure 5.1*a,b,c). *Figure 5.1*d shows misaligned electrodes lead to an uneven distribution of current and heat generation at the weld interface which can result in an asymmetric or irregular FZ formation, compromising the weld's strength and integrity [189].

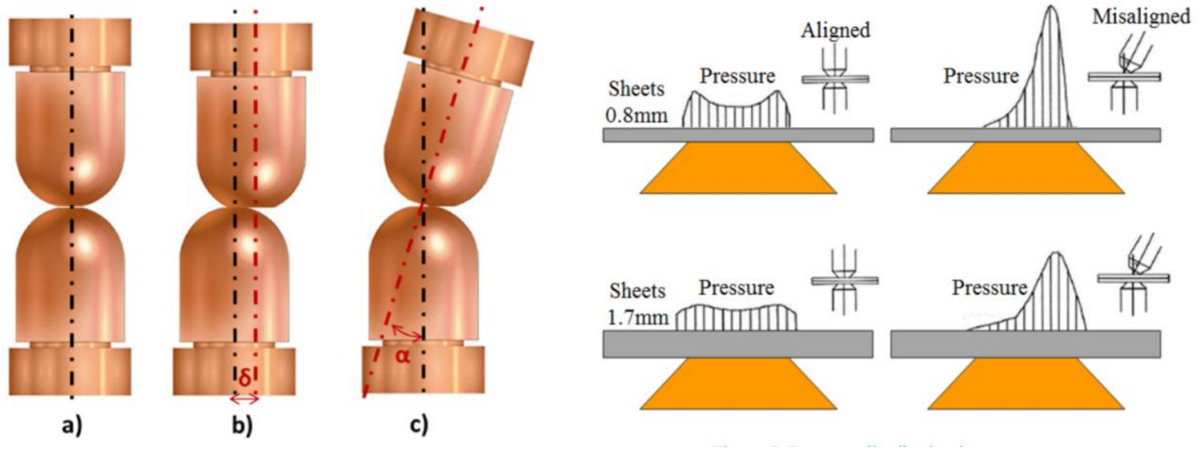

Figure 5.1. Electrode alignment status in RSW. (a) Aligned electrode. (b) Axial misalignment. (c) Angular Misalignment [190]. (d) Pressure distribution in the contact area [191].

5.3. RSW samples geometrical deviation

Geometrical deviation can impact the failure characteristics of welded joints during mechanical testing. For instance, research conducted by Mathiszik et al. [192] has demonstrated that the width of the specimen has a substantial impact on the failure behavior observed during tensile shear testing. The reason for this is that differences in the width of the specimen can change how stress is distributed and how much force the weld can handle during testing. Variations in electrode geometry can influence the transport variables during welding, which in turn affects the quality and consistency of the weld [193]. Variations in sample geometry, such as the dimensions and positioning of the FZ, can lead to stress concentrations, premature failures, and lower strength measurements.

The fatigue strength of spot welds is influenced by both the geometrical factors and their variability. Slight deviations in geometric parameters can have a substantial impact on the fatigue performance of welded structures, which is very important for ensuring their long-term durability [125].

A study highlighted that different standards and specifications recommend varying dimensions for tensile-shear testing specimens, which can lead to discrepancies in test results and interpretations of weld quality [194]. Variations in electrode geometry affect the heat distribution during the welding process, which in turn influences the microstructure and mechanical properties of the weld [193][195].

The deformation of the sheet can affect the contact pressure between the electrodes and the sheets and can influence the pattern of FZ development. *Figure 5.2* shows a schematic drawing for RSW of deformed sheets. Uneven surfaces can lead to localized overheating or insufficient heating [196][197][198][199]. This uneven heat can result in inconsistent FZ growth, which is critical for the strength and quality of the weld [200].

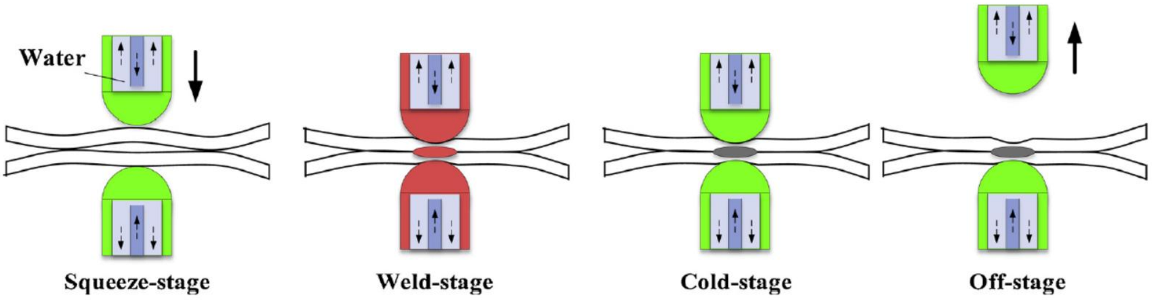

Figure 5.2. Schematic drawing of the four stages of a single RSW of a deformed sheet [201].

5.4. RSW machine calibration

Resistance spot welding machine calibration is a crucial process that ensures the welding equipment operates correctly and produces high-quality welds consistently. Regular calibration helps maintain the consistency of welding parameters, thereby ensuring uniform weld quality across multiple operations [202]. Managing the electrical aspects of the welding process through the calibration of a spot-welding machine is very important, as it directly impacts the thermal and metallurgical outcomes in the RSW [203][204]. Even slight deviations from the optimal settings can lead to defective welds or inconsistent weld quality [205][206].

Electrode geometry affects the quality and shape of fusion zones in RSW suggesting that optimal electrode geometry can enhance FZ formation and weld quality [207]. The geometry of welding electrodes, combined with appropriate thermal processes, can significantly affect the strength of the weld [208]. The impact of electrode wear on nugget formation in RSW was examined and found that electrode degradation led to decreased FZ area and tensile strength [209].

6. SUMMARY, SPECIFIC AIMS OF THE RESEARCH WORK

There is a common idiom saying, "Start where others left off," and in this research, I build upon the existing literature in main key areas, such as RSW parameter optimization and microstructural evolution. However, this approach is not applicable in all aspects, particularly where conflicting results exist such as the HCF behavior of AHSS, or in areas that have either never been investigated or were explored a long time ago, such as RSW impact force performance and HCM.
Therefore, based on the literature review, this research was undertaken to conduct comprehensive mechanical and microstructural examinations necessary for evaluating the RSW of AHSS for automotive applications. The specific aims of the research are as follows:

- Studying the effect of geometrical deviations during the preparation of RSW testing samples on the quasi-static tests of AHSS steel to determine the level of accuracy required to achieve consistent and reliable results.
- Determining the AHSS base material properties on the performance of RSW to enhance the integrity of spot welds under static, impact, and cyclic loading conditions.
- Examining the impact of optimizing welding parameters and welding technologies (1-pulse and 2-pulse) on the mechanical performance and microstructural transformations in RSW to achieve high-quality welds that meet required specifications.
- Measuring the heat cycle generated during RSW physically to understand the microstructural transformations occurring in the WN and the HAZ and validating the RSW heat cycle modeling.
- Exploring HCF loading and fatigue failure in AHSS to identify the key factors influencing RSW fatigue performance and durability.
- Measuring the force as a function of time to determine the absorbed impact energy in RSW and evaluate the behavior of spot joints under collision by implementing a new impact testing method.
- Evaluating the ability of RSW joints to withstand impact forces and analyzing impact failure under specific conditions.

7. RSW GEOMETRICAL DEVIATION

Tensile shear and cross-tension tests are standard methods for evaluating the mechanical performance of spot welds, providing essential data on the strength and failure characteristics of welded joints. The geometry of the test samples, including the size, shape, and orientation of the weld nugget, may influence the stress distribution and failure mechanisms observed during testing. The sample geometry, particularly the length and width of the sample and the positioning of the weld nugget may affect the load distribution and the identification of shear strength. Geometric deviations, such as smaller or off-centre weld nuggets can result in stress concentrations, premature failure, and lower measured strengths. In cross-tension testing, where the force is applied perpendicularly to the weld axis, the geometry of the sample dictates the mode and location of failure.

Optimal geometries can help ensure that the failure mode is consistent and reflective of the weld's inherent strength, rather than an artifact of geometrical deviations. Due to necessitating rigorous testing through tensile shear and cross-tension methods, the geometry of the samples used in these tests plays a crucial role in accurately evaluating the weld's mechanical properties. This study investigates the importance of sample geometry in tensile shear and cross-tension testing of DP and MS steel, aiming to establish guidelines for sample preparation that enhance the reliability and relevance of test outcomes.

7.1. Materials and methods

The impact of geometrical deviations on testing SSAB Docol DP600, DP800, DP1000, MS1200, and MS1400 specimens joined by RSW were investigated. Accurate specimen geometry is crucial for assessing mechanical properties, as inconsistencies can cause significant variability in test results. The research quantifies how variations in geometry affect tensile strength, displacement, and failure modes, focusing on tensile-shear and cross-tension tests. The findings highlight the need for rigorous standards in specimen preparation to ensure reliable mechanical testing data and optimize welding practices.

A series of tensile shear and cross-tension tests were conducted for the above-mentioned spot-welded base materials, each 1.0 mm in thickness and featuring various geometrical deviations. The chemical composition and mechanical properties of the DP600, DP800, DP1000, MS1200, and MS1400 steels are detailed in *Table 7.1* and *Table 7.2*, respectively.

Table 7.1. The chemical composition of the Docol steels (weight%).

Grade	C	Si	Mn	P	S	Cr	Ni	B
DP600	0.098	0.2	0.81	0.015	0.002	0.03	0.04	0.0002
DP800	0.136	0.20	1.55	0.013	0.003	0.03	0.04	0.0003
DP1000	0.132	0.19	1.50	0.010	0.003	0.03	0.03	0.0002
MS1200	0.105	0.20	1.59	0.011	0.003	0.03	0.03	0.0022
MS1400	0.22	0.46	2.46	0.016	0.003	0.03	0.12	0.00

Table 7.2. The mechanical properties of the Docol steels.

Grade	Yield strength $R_{p0.2}$ (MPa)	Tensile strength R_m (MPa)	Elongation A_8 (%)	Hardness (HV10)
DP600	448	669	18.7	204
DP800	585	871	15.5	270
DP1000	821	1074	9.5	329
MS1200	1108	1289	18.7	386
MS1400	1391	1496	4.5	470

The effect of geometrical deviations (displacement and misalignment) on the cross-tension and tensile shear tests was thoroughly investigated. Each test was categorized into three groups, with each group experiencing three distinct geometrical deviations. Each test was categorized into three groups, with each group experiencing three distinct geometrical deviations. In the cross-tension test, the first group was subjected to displacement along the sliding line (SL. disp.) within the C-T test tool, the second group faced angular misalignment (Ang. mis.), and the third group encountered displacement in the spot weld (SW. disp.) from the tension center line. The deviations for the first and third groups were 0.75 mm, 1.0 mm, and 2.0 mm, respectively, while the angular misalignment for the second group was set at 3°, 4°, and 8°, respectively. *Figure A1.1* (on the right) and *Figure A1.2* in Appendix A1, shows a schematic drawing for geometrical deviations of the C-T test. Within each group, a sample with 0.0 geometrical deviation was meticulously prepared as a reference for comparison against the other samples. *Figure A1.1* (on the left) and *Figure A1.3* in Appendix A1 illustrates the geometrical standard (0.0 geometrical deviation) for both the C-T and T-S test groups.

Regarding the tensile-shear test, it differs in the first group, the deviation is a parallel misalignment (Par. mis.) of the first sheet from the center line of the spot weld in the second sheet. Each group was compared to an accurate standard sample to determine the effect of the mentioned deviations on the test results. *Figure A1.4*, *Figure A1.5*, and *Figure A1.6* in Appendix A1 shows the drawings and values of geometrical deviation in T-S test groups.

7.2. RSW samples assembly and preparation

The BM sheets were cut to specific sizes and shapes, ensuring that they were free of burrs and deformation to guarantee correct weld positioning for the test. The jigging bolt holes in the cross-tension test and the pin holes in the tensile-shear test were precisely drilled, and any burrs resulting from drilling were removed using deburring tools. This is crucial because burrs can prevent testing parts from fitting together properly, leading to misalignment or assembly difficulties.

All standard samples were welded within a special template to ensure there was no deviation or displacement during welding. *Figure A1.7* in Appendix A1 displays the template for RSW samples used in both C-T and T-S tests.

Since surface preparation is a critical step before RSW, the BM was cleaned to remove oils, grease, oxides, and other contaminants, ensuring accurate electrical resistance across the weld interface.

A dimensionally accurate cross-tension test tool was created to apply a controlled tensile force to an RSW welded joint in a cross configuration, thereby assessing its strength and performance. *Figure A1.8* in Appendix A1 shows a 3-D drawing of the cross-tension test tool assembly.

7.3. RSW welding machine calibration and technology

The RSW was carried out using a TECNA 8007 resistance spot welding machine using AC (50 Hz) and controlled by a TE550 microprocessor-based welding control unit. The experiments were performed in constant current mode. Copper chromium zirconium (CuCrZr) welding electrodes were used with a 5 mm spherical head diameter. The radius of the electrodes with spherical head must be chosen depending on the sheet thickness to be welded. For a sheet thickness of 1 mm, R=50 mm radius was used, which is recommended in the literature [210][211] and previous experiments can contribute to the stability of the process. The design of the electrodes is presented in *Figure A1.9* in the Appendix A1

Straight edges were used to verify the alignment of the electrodes, ensuring they were parallel and centered relative to each other. The calibration of resistance spot welding machines involved utilizing specialized instruments to measure the actual output and performance of the welding machine, with these measurements then compared against desired standards. Calibrated TECNA TE1700 RSW weld testers were employed to assess the reliability of the spot-welding machine. Various probes were connected from the tester to specific points on the welding machine to measure welding current, force at the electrodes, voltage at the electrodes, energy, resistance, and thermal current. *Figure A1.10* in Appendix A1 illustrates the probes and their functions.

All RSW parameters were verified by setting specific values of welding parameters and then checking these using the TECNA TE1700 RSW measuring device. The input parameters closely matched the measured values, indicating that the welding machine did not require calibration. *Figure A1.11* in Appendix A1 presents the results of checking various RSW parameters.

The RSW parameters were optimized and selected based on comprehensive mechanical and microstructural testing. This approach ensured the production of defect-free weld nuggets, meeting the required quality and performance standards. *Table 7.3* shows The RSW parameters for the applied cross-tension and tensile-shear tests. Appendix A6 provides the welding procedure specification (WPS) for the resistance spot welding (RSW) process employed in the study.

Table 7.3. RSW welding parameters

Welding current (kA)	Welding time (ms)	Welding force (kN)
8.5	320	5

7.4. Quasi-static testing

Figure A1.12 in Appendix A1 shows the MTS 322 test frame machine utilized at a loading speed of 0.2 mm/s in the mechanical L-D tests. Cross-tension-appropriate aligned grips, capable of securely holding the specific type of sample without slipping, were attached to the machine. Calibrated load cells and displacement transducers were positioned accurately. The sample was carefully placed in the testing tool, and the screws were tightened firmly to ensure proper positioning and to prevent slipping.

The samples were installed meticulously in the grips to ensure that the weld was oriented perpendicularly to the direction of the applied force and that the sample was centered and aligned properly. For the tensile-shear test, two pins with a 5 mm diameter were inserted into the holes at the edges of the sample for proper grip and fixture alignment to securely hold the sample and apply force in the desired orientation (see *Figure A1.13* in Appendix A1). A tension load was applied gradually using a hydraulically controlled mechanism until the weld failed. The data collected during the test, including the maximum force withstood, the displacement at the break, and the failure mode, illustrated the behavior of the sample. *Figure A1.14* to *Figure A1.19* in Appendix A1 show the cross-tension test results of DP600 and MS1400 samples respectively. *Figure A1.20* to *Figure A1.25* in Appendix A1 show the tensile-shear test results of DP600 and MS1400 samples respectively.

7.5. Quasi-static tests results

From the C-T and T-S load-displacement figures shown in Appendix A1, it is evident that there is significant convergence in the load-displacement results of the cross-tension (C-T) and tensile-shear (T-S) tests of DP600 samples. However, sample number C1 exhibited a slight superiority. For the C-T test results of MS1400 samples, it is very clear that the samples with zero deviation showed superiority, and the samples with 2 mm and 8° degrees deviations showed a noticeable decrease compared to the standard samples, while the rest of the deviations showed a slight decrease. As for the T-S test of MS1400 steel, samples with 2 mm and 8° degrees deviations showed a significant decrease in force and a big similarity in the rest of the deviations. In terms of the failure mode, there is also a notable similarity in the shape and size of the failures.

As for the T-S test of samples T4, T8, and T12 (2 mm and 8-degree deviations) in parallel misalignment and angular misalignment deviations, the samples showed a noticeable decrease in the load of about 3.71, 2.3, and 3.62 kN compared with T1, T5, and T9 (0.0 mm and 0-degree deviations), respectively, and big similarity in the rest of the deviation samples in terms of load and displacement.

Table A1.1 and *Table A1.2* in Appendix A1 displays the average results of four samples each geometrical deviation demonstrating the effect of geometrical deviation on the C-T and T-S results respectively, as the type of deviation (Dev. Type), the value of geometrical deviation (Dev. Value), the average test load (Avg. Load), the percentage of load deviation value (% of Disp. Dev.) compared to the standard value (0 deviations), the average displacement (Avg. Disp.), the percentage of displacement value (% of Disp. Dev.) compared to the standard value (0 deviations), and the plug diameter (d) and partial plug diameter (d_P). In our research, since the plug failure modes resulted from C-T and T-S tests are symmetric the plug diameter (d1, d2), and the partial plug diameter (d3) are equal in each plug failure mode samples in both tests while the partial plug failure mode (P.Plug) samples have shown a difference in d3. We can notice from *Table A1.1* in Appendix A1 of MS1400 that the greater the deviation, the smaller the partial plug diameter. This means that the relationship between the geometrical deviation and the interfacial fracture area is direct. *Figure 7.3* shows the schematic drawing of the symmetric plug and partial plug diameter measurement including the interfacial fracture.

After conducting C-T and T-S tests on DP600 and MS1400 to check the geometrical deviation effect on mechanical properties, it was observed that MS1400 exhibited a significant impact on mechanical properties and failure modes. *Figure A1.26, Figure A1.27 and Figure A1.28* in the Appendix A1 illustrated how plug average diameter changes with different geometrical deviations for DP600 and MS1400 materials in C-T test. MS1400 consistently shows larger plug diameters but is more sensitive to deviation, with a steady decline across all types. In contrast, DP600 remains relatively stable or shows a slight increase, indicating greater tolerance to misalignment and displacement.

This finding underscored the necessity of further investigation into the series of steels, specifically DP800, DP1000, and MS1200, to determine up to which grade the geometrical deviations remain unaffected. The mechanical properties and chemical composition are provided in *Table 7.1* and *Table 7.2* respectively. *Figure 7.1* and *Figure 7.2* present the T-S and C-T geometrical deviation samples, respectively, alongside the standard sample for comparison as illustrated in the figures shown in Appendix A1. The results demonstrated a remarkable consistency across all grades (DP600, DP800, DP1000, MS1200) except MS1400, indicating that geometrical deviations at various levels did not influence the test outcomes. Furthermore, all samples consistently failed in the pull-out (plug) failure mode, reinforcing the conclusion that geometrical deviations do not compromise the mechanical performance within the tested range except MS1400.

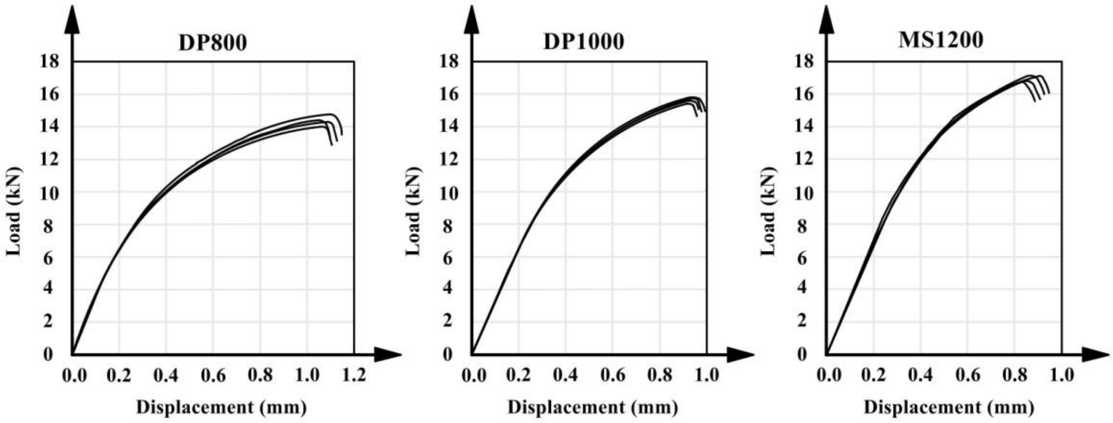

Figure 7.1. Tensile-shear test results of all geometrical deviations.

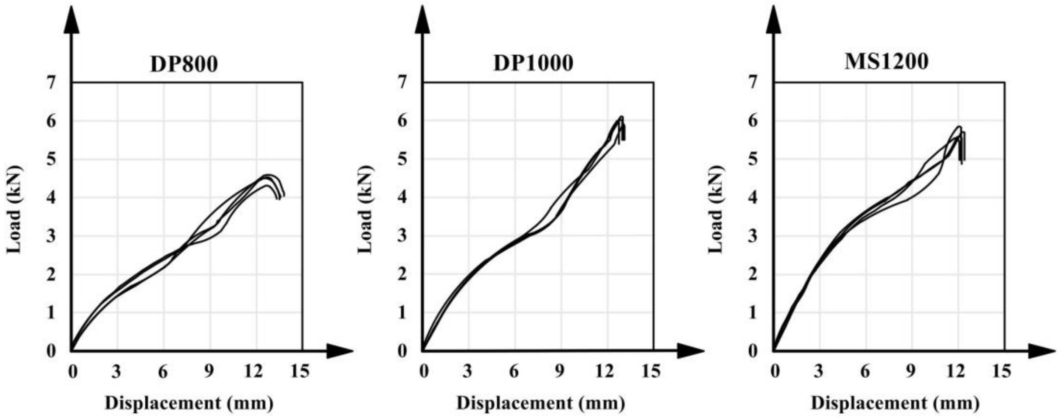

Figure 7.2. Cross-tension test results of all geometrical deviations

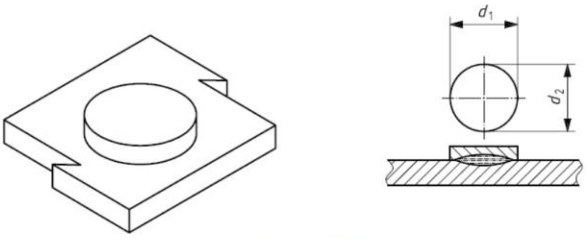

a) Symmetrical [a]

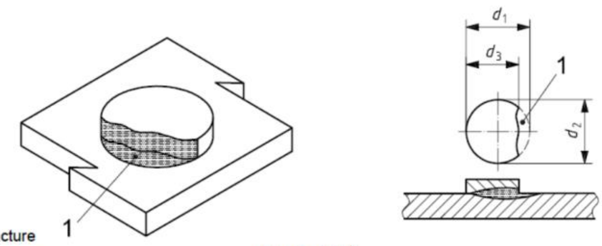

Key

1 interfacial fracture

[a] $d = d_p = (d_1 + d_2)/2$.

[b] $d = (d_1 + d_2)/2$ and $d_p = (d_2 + d_3)/2$.

b) Partial [b]

Figure 7.3. (a) Schematic drawing of the symmetric pull-out (plug), (b) partial pull-out (partial plug) diameter measurement [199].

7.6. Failure mode

In the cross-tension (C-T) test of DP600 RSW samples, all samples exhibited a symmetrical plug failure mode within the FZ boundary, except sample C12. This sample demonstrated a combined failure mode of the plug at the nugget boundary and a bump from the HAZ. *Figure 7.4.* shows that the bump formed after the failure, as depicted L-D diagram, indicating that it did not influence the outcome of the test, as detailed in *Table A1.1* in the Appendix A1.

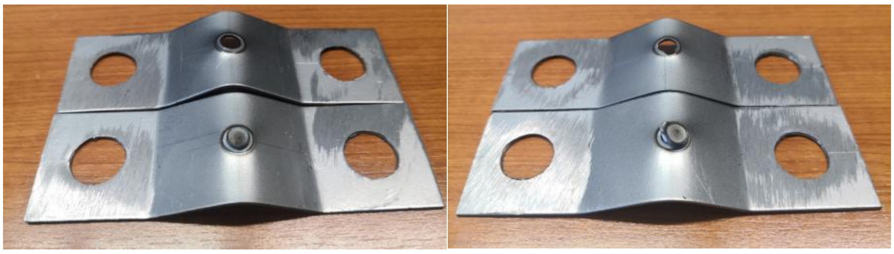

Figure 7.4. Plug failure mode in sample C1 is on the left and Plug failure mode in sample C12 is on the right in DP600 samples.

In the cross-tension (C-T) test of MS1400 RSW, C1, C5, and C9 samples exhibited a symmetrical circular plug failure mode within the nugget boundary as shown in *Figure 7.5*. As for the failure mode in the rest of the samples, it is a partial plug in different sizes and patterns. *Figure 7.6* and *Figure 7.7* shows the partial plug failure mode and the increase of interfacial fracture area in samples C3 and C4 samples, respectively, as detailed in *Table A1.1* in the Appendix A1.

Figure 7.5. Plug failure mode in sample C1 of MS1400.

Figure 7.6. Partial plug failure mode in sample C3 of MS1400.

Figure 7.7. Partial plug failure mode in sample C4 of MS1400.

It was observed that the failure mode occurred at the crest of the deformation in all samples. This phenomenon may result from how the metal's ductility responds to the direction of stresses during the test, contributing to the great similarity in results across samples. This principle also extends to the tensile-shear (T-S) test, where the ductility of metals may counteract the deformation, leading to uniform stresses on the spot weld and thus similar results across all tested samples.

In the tensile-shear (T-S) test of DP600 RSW samples, all samples exhibited failure, predominantly through the plug failure mode, except for samples T1, T2, and T5, which failed in the plug-in base metal (PBM) mode. As depicted in *Figure 7.8,* these exceptions did not influence the overall results of the test.

Figure 7.8. The failure mode in sample T1(plug-in base metal) is on the left and the failure mode in sample T3 (Plug) is on the right in DP600 samples.

In the T-S test of MS1400 RSW, the failure mode in all samples was a plug as shown in sample T5, (see *Figure 7.9*) with great similarity in size and symmetry except for sample T4, which showed a partial plug failure as shown in *Table A1.2* in the Appendix A1, *Figure 7.10* shows partial plug failure mode in sample T4. All samples that had an Expulsion that occurred because of the BM arching deformation during welding were repeated due to unacceptable results, see figures of expulsion showed in *Figure A1.29* and *Figure A1.30* in Appendix A1. The expulsion occurred due to the BM arcing resistance of the welding electrodes, which reduces the welding force, increasing the heat generated.

Figure 7.9. Plug failure mode in sample T10 of T-S test samples.

Figure 7.10. Partial plug failure mode in sample T4 of T-S test samples.

By applying the same tests under identical conditions to ultra-high-strength steel like MS1400 and due to its high hardness and strength, this type of metal does not respond as readily to the direction of deformation in samples with geometrical deviations, resulting in uneven stresses that impact the test results compared to standard samples of the same metal. A current literature review reveals limited direct information on the effect of misalignment in cross-tension and tensile shear samples, specifically in the context of RSW of any steel type. Through comparative analysis of various steel grades, it is possible to elucidate how dimensions and shapes influence stress distribution, failure modes, and overall test results. This approach provides valuable insights for optimizing sample design to accurately assess weld quality.

7.7. Conclusion

The investigation into the welded joints' strength and failure mode allows us to draw the following conclusions:

- The deviations (misalignment and displacement) did not significantly affect the outcomes of the C-T and T-S tests of DP600, DP800, DP1000, and MS1200 samples.
- The remarkable similarity in the failure modes and test results across all steel grades indicates that all samples were welded under consistent conditions, highlighting the crucial role of optimizing sample preparation in controlling spot welding quality.
- In the cross-tension test of DP steels, the failure mode was predominantly at the peak of the deformation and was almost symmetrical, reflecting the ductility response to spot weld strength.
- In MS 1400 greater geometrical deviation in C-T results produce a higher partial plug. This indicates a direct relationship between the extent of geometrical deviation and the interfacial fracture area.
- In the T-S test of MS1400, the effect of geometrical deviation was limited to reduce displacement, while it had a noticeable effect on reducing force.
- For C-T and T-S test results of MS1400 samples, the standard samples with zero deviation showed superiority, while the samples with 2 mm and 8° degrees deviations showed a noticeable drop in the RSW strength.
- Comparing MS1400 to DP600, DP800, DP1000, and MS1200 it was proven that the C-T and T-S results are more likely to be affected by geometrical deviation in higher-strength steel.

8. WELDING PARAMETER OPTIMISATION OF AHSS

The influence of welding parameters on similar RSW samples, focusing on optimizing these parameters for improved performance was investigated. The primary goal is to evaluate and compare the macrostructure and quasi-static mechanical properties of DP and MS RSW joints. This is achieved through tensile-shear tests (T-S), optical macroscopic examinations, and microhardness measurements, using various welding parameters to determine the optimal conditions for the best results.

8.1. Materials and methods

MS steel as SSAB Docol (DP600, DP800, DP1000, MS1200, MS1400) with 1 mm thickness steel sheets, *Figure A1.3* in Appendix A1 shows the schematic drawing of RSW sample geometry which complies with shear-tensile test requirements. The mechanical properties and chemical composition are provided in *Table 7.1* and *Table 7.2* respectively based on the manufacturer material certificates and the hardness was measured at the lab. All microstructural and T-S samples were prepared and tested as per Chapter 5.0, and the welding parameters are listed in *Table 8.1*. *Figure 8.1.* illustrates the three different resistance spot welding (RSW) modes utilized in this study, each characterized by specific combinations of electrode force, current, and welding time.

A squeeze time of 300 ms is initially applied to ensure proper contact at the interface prior to current application. In Figure (a), the hard work mode is presented, commonly referred to as the long-time weld. This mode is defined by a relatively high welding current of 8.5 kA, an extended weld time of 320 ms, and an electrode force of 5 kN, resulting in a high overall heat input. In contrast, Figure (c) shows the soft work mode, identified as the short-time weld. In this case, the welding current (5.8 kA), weld time (240 ms), and electrode force (3 kN) are all reduced, leading to a lower heat input. Figure (b) illustrates the Post-Heat Work mode, also referred to as the two-pulse weld. In this configuration, an initial welding pulse is immediately followed by a secondary, identical pulse (6.4 kA) after a brief cooling interval of 300 ms, with an electrode force of 3 kN maintained throughout. Following the welding process in all three modes, a hold time of 200 ms is applied to allow the weld nugget to solidify under constant electrode pressure, thereby promoting controlled cooling and improving weld quality.

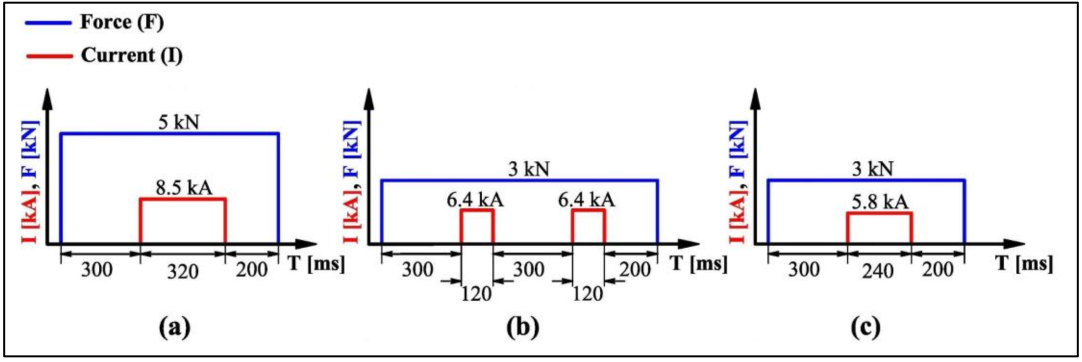

Figure 8.1. Schematic of RSW Schedules. (a) long-tome (Hard work), (b) 2-pulse (Post-heat work), and (c) short-time RSW (Soft work)

Table 8.1. RSW parameters.

Welding mode	Welding technology	Welding current (kA)	Welding time (ms)	Cooling time (ms)	Pulse no.	Welding force (kN)
Hard work	Long time	8.5	320		1	5
Post-heat work	2-pulse	6.4	120	300	2	3
Soft work	Short time	5.8	240		1	3

The RSW parameters outlined in *Table 8.1.* were selected based on insights from previous investigations into resistance spot welding (RSW) and a thorough review of relevant literature, ensuring that the chosen parameters reflect practical experience and provide a solid foundation for the research. Appendix A6 provides the welding procedure specification (WPS) for the resistance spot welding (RSW) process employed in the study.

8.2. Tensile-shear test results

T-S tests were conducted to investigate the impact of various welding technological parameters on MS and to evaluate how prolonged welding times affect different grades of DP steels.

Figure A2.1 and *Figure A2.2* in the Appendix A2 shows the tensile-shear test results for the RSW of MS1200 and MS1400 under three different welding technological parameters short time (5.8 kA), 2-pulse (6.4 kA), and long-time (8.5 kA) highlighting significant variations in load capacity, displacement, and failure modes. Short-time welding (5.8 kA) resulted in the lowest peak loads, smallest displacements, and the smallest FZ sizes. The predominant interfacial failure (IF) failure mode suggests weaker joints due to insufficient heat input and limited fusion. 2-pulse welding (6.4 kA) showed moderate improvements in peak load and displacement, though the FZ sizes were slightly smaller compared to short-time welding. The failure mode shifted to pullout failure (PF) in MS1200 and MS1400, indicating stronger fusion compared to short-time welding. Long-time welding (8.5 kA) produced the best overall results, with the highest peak loads, largest displacements, and the largest FZ sizes. The failure modes predominantly transitioned to pull-out (PF), reflecting greater weld strength, ductility, and metallurgical bonding due to higher heat input. *Table 8.2* shows T-S results details.

The results of the tensile-shear test for MS1200 and MS1400 steel joints demonstrate the significant influence of welding current on weld performance. Higher welding current improves weld strength, displacement, FZ size, and failure modes. Comparing both materials, MS1200 joints exhibit slightly higher ductility, as evidenced by the greater displacements observed, particularly under the 8.5 kA condition. Meanwhile, MS1400, being a stronger steel, exhibits less overall displacement despite similar or slightly lower peak loads. *Figure A2.3* in the Appendix A2 shows the tensile-shear test results RSW for various steel grades DP600, DP800, DP1000, MS1200, and MS1400 conducted at a welding current of 8.5 kA with a long welding time technological parameter. All samples experienced a pull-out failure mode, indicating strong weld integrity and adequate fusion between the sheets. The load-displacement curves show a clear distinction in mechanical performance based on the material grade. DP600 exhibits the lowest peak load, attributed to its lower strength among the tested materials, while MS1400 achieves the highest peak load due to its superior mechanical properties. As the steel grade increases in strength, the peak load also rises, showing a proportional relationship between material strength and load-bearing capacity. However, the ductility, represented by the total displacement at failure, generally decreases for higher-grade steels like MS1400, reflecting a trade-off between strength and deformation capability.

Table 8.2. Tensile-shear test results of MS steel

Grade	Welding technology	Cooling time (cycle)	Peak load (kN)	Displ (mm)	Failure mode
MS1200	Short time		11.49	0.54	IF
MS1200	Short time		10.54	0.54	IF
MS1200	Short time		11.04	0.48	IF
MS1200	2-pulse	15	12.34	0.67	PF
MS1200	2-pulse	15	11.50	0.61	PF
MS1200	2-pulse	15	11.53	0.61	PF
MS1200	Long time		17.98	0.79	PF
MS1200	Long time		18.14	0.90	PF
MS1200	Long time		17.99	1.04	PF
MS1400	Short time		12.09	0.55	IF
MS1400	Short time		11.40	0.49	IF
MS1400	Short time		11.41	0.50	IF
MS1400	2-pulse	15	12.61	0.52	PF
MS1400	2-pulse	15	13.09	0.56	PF
MS1400	2-pulse	15	12.67	0.50	PF
MS1400	Long time		17.59	0.90	PF
MS1400	Long time		17.31	0.64	PF
MS1400	Long time		17.47	0.68	PF

8.3. *Macrostructural and microhardness evaluation*

Figure A2.4 to *Figure A2.9* in Appendix A2 presents the microhardness distribution profiles and illustrates the results of the hardness distribution across the FZ and HAZ, represented by the green line in each graph. The base metal hardness values for the respective materials are shown using colored lines pink, orange, and brown. The horizontal axis indicates the distance from the nugget center in millimeters (mm) and the vertical axis displays the Vickers hardness measurements in HV0.2 unit. For welding technological parameters, MS1200 and MS1400 RSW long-time samples with 8.5 kA current parameter showed a significant softening in the SCHAZ and ICHAZ of up to 120 HV less than the BM, and a very slight increase in the hardness was observed in the FZ. The samples that were welded with a current of 5.8 kA showed the same pattern in the hardness diagram but with a difference in softening value less than the samples that were welded with a current of 8.5 kA. While in the 2-pulse two softening zones were observed, the first zone located in SCHAZ, ICHAZ, and the recrystallization fusion zone (Rex-zone), there was a small increase in the hardness located between the two softening zones as a result of double pulses weld.

Table 8.3 presents data from T-S RSW tests regarding the effect of long-time 8.5kA on the MS and DP, focusing on the mechanical and hardness properties of different steel grades. The RSW peak load follows an upward trend, with MS1400 exhibiting the highest load capacity, while DP600 has the lowest. However, as the strength of the steel increases, the displacement before failure decreases, showing reduced ductility in higher-strength materials.

Table 8.3. Results of tensile-shear and microhardness tests of long-time RSW parameter.

Sample grade	Nugget size (mm)	BM hardness HV0.2	Softening measurement HV0.2	FZ AVG. hardness HV0.2	Peak load (kN)	Displacement (mm)	Failure mode
DP600	6.8	210	N/A	428	11.46	1.53	PF
DP800	6.9	280	N/A	449	14.65	1.02	PF
DP1000	6.8	330	287	451	15.4	0.9	PF
MS1200	6.9	414	306	453	16.76	0.83	PF
MS1400	6.9	460	340	505	17.4	0.78	PF

The microhardness test results for RSW of the five different steel materials MS1400, MS1200, DP1000, DP800, and DP600 are presented in *Figure A2.8* to *Figure A2.12* in the Appendix A2. The results of the RSW microhardness testing reveal a clear relationship between the softening effect and the strength of the base metal. The most significant softening occurred in MS1400 as shown in *Table 8.3*, while no softening was observed in DP600. In both DP600 and DP800, there was a noticeable gradient of hardening from the SCHAZ toward the FZ, with the FZ in DP600 exhibiting nearly double the hardness of the base metal. The findings indicate that the FZ size remains consistent across different base metals welded under identical welding parameters. This suggests that the type of base metal has minimal influence on the FZ size, while the welding parameters play a dominant role in determining its dimensions. All samples failed in a pull-out failure mode, which is desirable as it indicates a strong weld nugget and sufficient joining strength between the sheets, ensuring the reliability of RSW joints under tensile loading.

8.4. Conclusion

RSW joints were investigated with tensile-shear tests, microhardness tests, and an optical microscope and the following conclusions can be drawn:

- The best tensile-shear test results were achieved with long-time welding with the highest welding current and welding force. The FZ size was the biggest, in this case, almost twice the diameter like with other parameters.
- As a result of the RSW of MS1200 and MS1400, softening occurs in ICHAZ and SCHAZ in every case of the two welding technological parameter comparisons (long-time and 2-pulse), but the value and area of the softening are different. The long-time welding showed the softening in the HAZ, but this zone is relatively narrow. In the case of pulse technology, the softening area is wider.
- In all cases long-time welding with high welding current and welding force shows the best results since the FZ diameter is the biggest therefore it's worth checking the 2-pulse technology with the same FZ diameter.
- The base metals of DP and MS steels play a major role in the HAZ softening and FZ Hardening results of welded samples with the same parameters.

9. HIGH CYCLE FATIGUE OF DP & MS STEELS

The fatigue investigations explored two key aspects of HCF testing, the evaluation of RSW mechanical properties of RSW and the analysis of fatigue behavior across various advanced steel grades. Since FZ size is a crucial factor in assessing RSW quality, this comparison allows for a detailed analysis of how welding technological parameters influence performance. The second part examines the HCF behavior of different steel grades, including DP600, DP800, DP1000, MS1200, and MS1400, welded in the same welding parameters and conditions to determine the impact of steel grade on the HCF performance.

The fatigue life of RSW joints is mainly investigated by fatigue tests and the generated load-cycle number (L-N) curve is used to confirm endurance limit and HCF resistance. As a precursor to HCF analysis, T-S and microstructural tests were conducted, and failure mechanisms have been discussed.

9.1. Materials and methods

In the HCF analysis of the different DP and MS steels the welding parameter combinations namely long-time as shown in *Table 8.1* were applied on Docol DP600, DP800, DP1000, MS1200, and MS1400 steel sheets with a thickness of 1 mm. The chemical composition and mechanical properties of the base metals are shown in *Table 7.1* and *Table 7.2*, respectively. All RSW joints were examined by T-S, microhardness, and macroscopic tests to evaluate the HCF test results and its failure mode. All mentioned tests and RSW joints were conducted according to Chapter 5.0

Lap shear samples with 1 mm sheet thickness were prepared for HCF tests. Twenty samples of each grade were prepared for more reliable results. Two spacers, the same as the sample BM by material and thickness, were welded in the grip area to eliminate the misalignment resulting from the overlap. Two pin holes located in the grip area were drilled to increase the grip restriction and ensure accurate sample positioning during the HCF test. *Figure 9.1* shows the sample geometry schematic drawing.

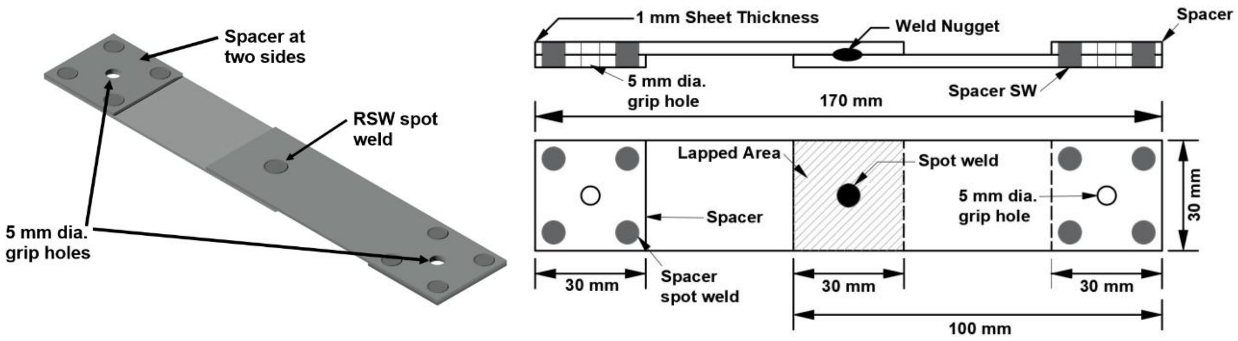

Figure 9.1. Sample geometry drawing: 3D in view (left) and 2D top view schematic drawing (right).

9.2. RSW Mechanical properties investigations

Hardness distribution and macrostructure examination characterize the properties of the spot weld as a prior step of HCF evaluation. The hardness measurement in the FZ followed a descending order from MS1400, which exhibited the highest hardness, to DP600, which showed the lowest. However, the hardening ratio of the weld nugget to the BM hardness showed the opposite trend, being lowest in MS1400 and highest in DP600. A minimal softening occurred in DP1000 HAZ while no softening was measured in DP600 and DP800. In MS steels a significant softening occurs in HAZ started in ICHAZ until SCHAZ. Appendix A2 shows the microhardness distribution across (MS1400, MS1200, DP1000, DP800, and DP600) steels. *Table 8.3* summarize the microhardness and T-S results of long-time DP and MS RSW.

In the HCF analysis of the different DP and MS steels the T-S test was conducted to evaluate the HCF. *Figure A2.3* in Appendix A2 shows the load-displacement curves for tensile-shear (T-S) tests of targeted steels welded with 8.5kA, long-time. Failure mode investigations are very important along with load-displacement curves, as it give us information concerning the spot weld mechanical properties such as ductility and the ability to absorb energy. All failure modes observed were pull-out across all steel grades, with BM deformation evident in each case, highlighting the ability of spot welds to effectively transfer loads to the adjacent areas, a compelling reason to advance the study of HCF. The deformation followed the same pattern as the displacement, with the highest deformation occurring at DP600 and gradually decreasing to the lowest deformation at MS1400. *Figure 9.2* shows the failure mode and BM deformation for MS1400 samples as an example.

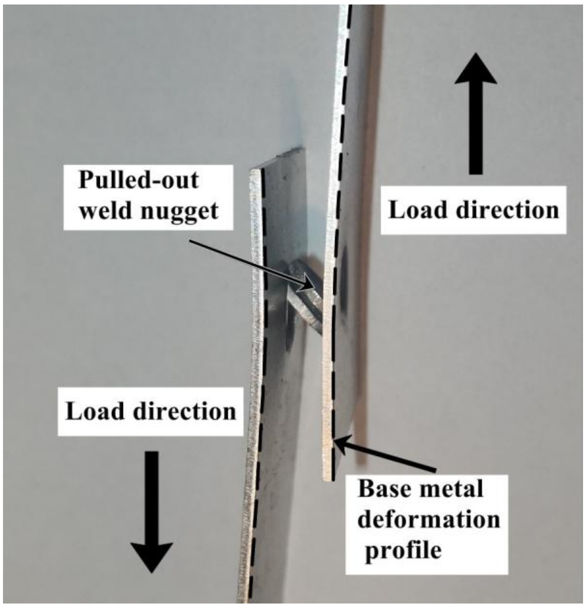

Figure 9.2. MS1400 tensile-shear test pull-out failure mode and BM deformation.

9.3. High cycle fatigue testing

HCF tests were carried out by MTS 322.41 electro-hydraulic universal materials test frame. Tension-tension sinusoidal cyclic load controlled by MTS FlexTest 40 hardware controller at load ratio (L_{min}/L_{max}) of R=0.1 with frequency f = 30 Hz. During the HCF tests several load levels were applied to the samples at room temperature. *Figure 9.3* shows the sample installation setup in the materials testing equipment.

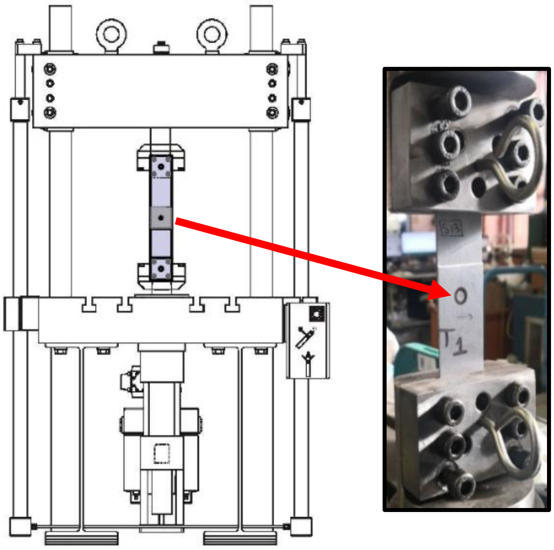

Figure 9.3. Schematic drawing of MTS 322 materials testing equipment (left) with the fractured sample after a fatigue test (right).

Fatigue testing was conducted with axial loading generating only tensile-tensile loads cycled between a maximum and a minimum tensile load. Applied loads were described by the range of loads, which is the difference between the maximum and minimum loads in one cycle, load range $\Delta L = (L_{max}-L_{min})$. The results of fatigue testing were plotted by load range to a number of cycles to failure using a logarithmic scale for the number of cycles in the (L-N) curve.

It was worth looking for the results of practical experiments in other research to enlarge the comparison cycle with different testing conditions. It was found that many studies showed that most of the samples that were loaded with a 1000-3000 N failed in more than 50000 cycles [62][128][134][135][212][213]. Although the base metals and the fatigue testing conditions are not identical to the study, the convergence between the fatigue results in the research is a good indicator of the FZ performance in terms of HCF.

9.4. HCF results of RSW of DP and MS steels

The parameters of the "Mean" S-N curves were calculated using the Basquin equation [149]. Basquin's Law provides a fundamental relationship between stress range ($\Delta\sigma$) and fatigue life (N) in high-cycle fatigue analysis. This equation captures the inverse relationship between stress and the number of cycles to failure as fatigue life increases, the applied stress decreases.

In the realm of high-cycle fatigue analysis, the Basquin equation plays a pivotal role in establishing the relationship between stress amplitude (S) and the number of cycles to failure (N). This power-law relationship is expressed as $S = S_f' \cdot (N)^b$, where S_f' is the fatigue strength coefficient which defines the stress at one cycle to failure and represents the material's initial fatigue strength and b is the fatigue strength exponent, typically a negative value indicating the slope of the S-N curve in log-log space indicating how quickly fatigue strength decreases with increasing cycles.

Since high fatigue resistance is a result of the material's ability to resist crack initiation and propagation under cyclic loading, selecting materials with higher fatigue resistance after RSW is advantageous, especially in applications like automotive structures, where durability and safety are critical. *Figure 9.4* represents fatigue test data for the investigated materials, illustrating the relationship between the load range (ΔL) in Newtons and the number of cycles to failure on a logarithmic scale. The curves generally exhibit a downward trend, indicating that as the load range decreases, the number of cycles to failure increases. This is a typical behavior in fatigue testing, where higher loads lead to faster failure. A plateau appears at higher cycle counts (beyond 1000000 cycles), suggesting the fatigue limit or endurance limit, below which the material can theoretically withstand infinite cycles without failure. In DP steels the fatigue resistance improves as the grade of the material increases (DP600 < DP800 < DP1000). For the same number of cycles DP600 (black line) shows a lower load range indicating lower fatigue resistance, DP800 (green line) shows moderate performance, and DP1000 (red line) is the highest load range. In martensitic MS1200 (blue line) the curve exhibits the lowest endurance limit followed by MS1400 (orange line) despite the highest base material strength.

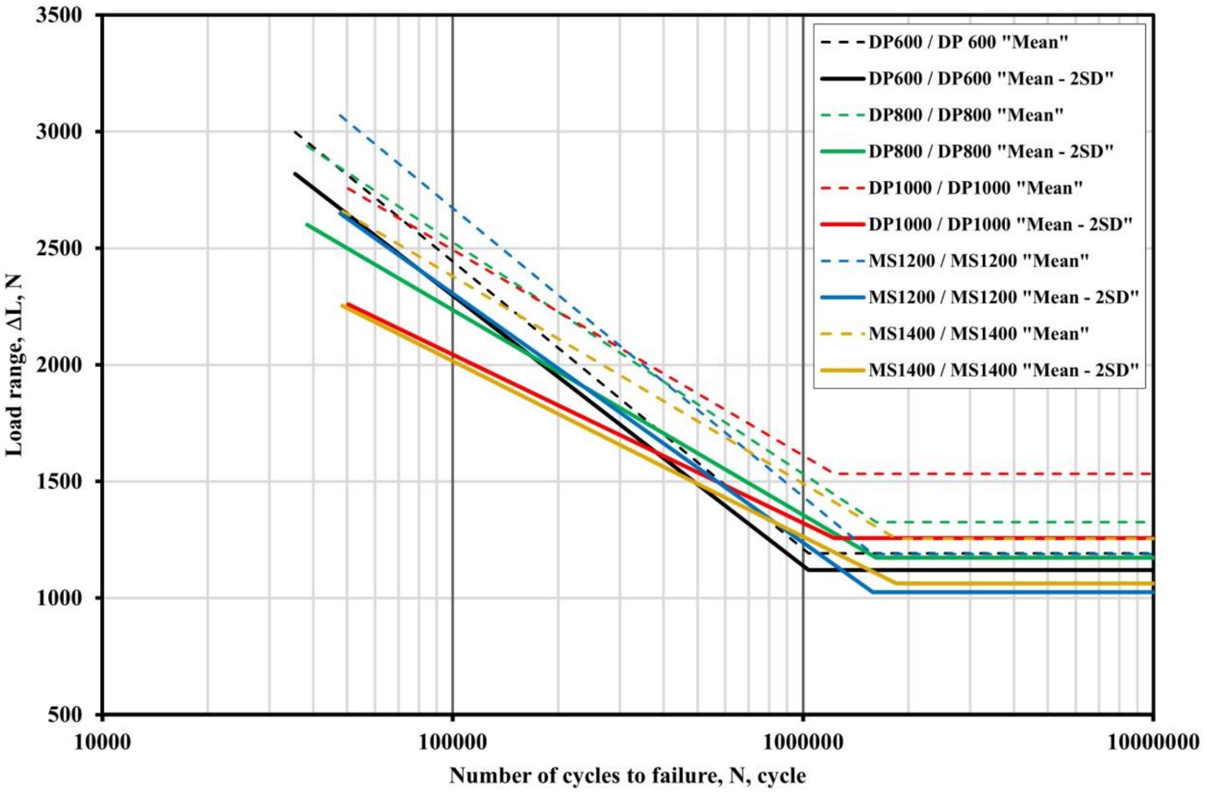

*Figure 9.4. Load range-number cycle to failure (*ΔL-*N) curve.*

The T-S test results can be partially connected to the analyzed fatigue results, specifically to explain why MS1200 exhibited the lowest endurance limit in fatigue tests. As shown in Figure *Figure 9.4*. The displacement at failure for MS steel is lower than that of DP steels, indicating poor energy absorption capacity compared to DP steels. On the contrary, DP1000 steel showed the highest fatigue with the lowest displacement amongst DP steels, followed by DP800 and then DP600 steels makes the interpretation of fatigue results more complicated. *Table 8.3*. presents the RSW results, highlighting hardness, softening, FZ diameter, and failure mode but no clear correlation was found to explain the observed fatigue behavior.

The poor fatigue resistance of MS RSW joints makes them less suitable for components subjected to cyclic loads. Use MS steels (e.g., MS1200) for applications requiring high static strength but avoid them for components exposed to significant cyclic loading such as suspension parts or structural members in vehicles. DP steels are better suited for components requiring a balance of fatigue resistance and ductility in welded joints.

9.5. *Fatigue crack*

The fatigue fracture behavior and crack growth characteristics of RSW were observed in all different grades, including DP600, DP800, DP1000, MS1200, and MS1400. Despite variations in material grades, the fatigue crack growth mechanism remains consistent across all these steel grades, as shown in *Figure 9.5*. The figure highlights that the crack initiation point is localized at the tongue and notch area within the FZ. This region experiences stress concentration due to the geometry of the weld nugget and the inherent microstructural variations caused by the welding process. The notch-like features at the weld boundary act as initiation sites for cracks under cyclic loading conditions.

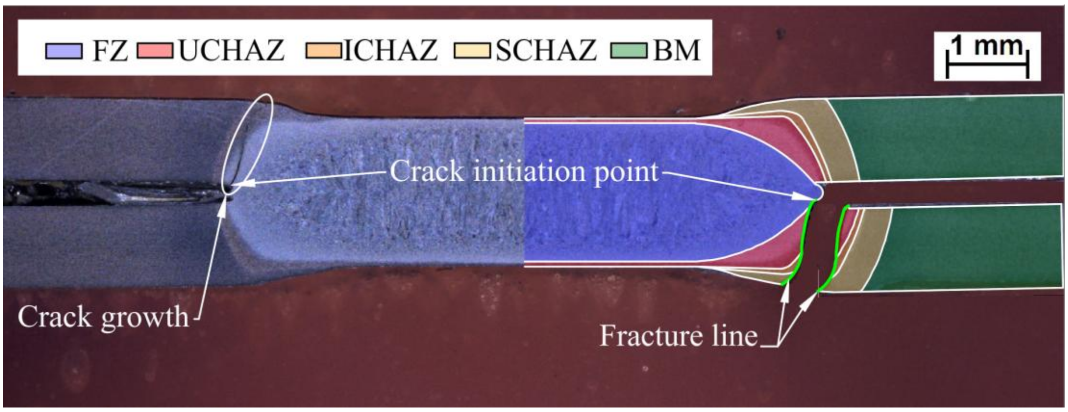

Figure 9.5. Fatigue failure of all investigated steels.

Once initiated, cracks propagate predominantly through the FZ, as depicted by the outlined fracture line where the material typically has a higher hardness and lower toughness compared to the base metal. The fatigue crack growth follows a path dictated by the microstructural and mechanical properties of the weld zone, including the interaction between the UCHAZ, ICHAZ, and SCHAZ. The transition of the crack into adjacent HAZ regions further validates the importance of the metallurgical characteristics in determining fatigue performance. The consistent fracture pattern across all the steel grades suggests that the localized stress concentration and microstructural heterogeneity in the tongue and notch area are primary factors governing fatigue failure in resistance spot welds.

From a top-view perspective, all samples exhibited an eyebrow-shaped failure pattern (see *Figure 9.6*), highlighting that the crack propagation followed the same mode across all grades. This consistent failure behavior suggests a similar fracture mechanism, emphasizing the uniformity of crack initiation and growth under the given testing conditions.

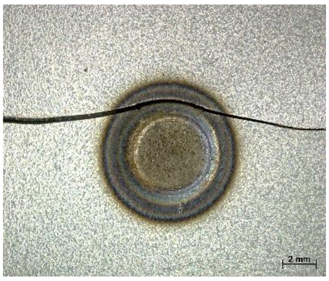

Figure 9.6. Top view of eyebrow shape crack propagation in MS1400 steel

To investigate whether the base metal grade influences the HCF results in addition to notch stress concentration, microhardness tests were conducted on the tongue (crack initiation point). The *Table 9.1* presents HV0.2 hardness measurements at the tongue (crack initiation point) for DP and MS steel. Notably, the HCF mean-2SD values follow the same sequence as the hardness results at the tongue, reinforcing the idea that steel grade significantly affects HCF performance. This consistency highlights the influence of material properties on fatigue resistance, providing clear evidence of the correlation between steel grade and HCF behavior.

Table 9.1. HV0.2 hardness measurements at tongue (crack initiation point) and endurance limit.

Base metal grade	DP600	DP800	DP1000	MS1200	MS1400
Hardness (HV)	419	435	441	386	392
Endurance limit (N)	1120	1173	1256	1025	1062

9.6. Conclusion

The different base metals of RSW pulse technology affect the mechanical properties and HCF performance of RSW joints can be concluded.

- While higher-strength steels provide advantages in short-life, high-load fatigue conditions, their benefits diminish in long-life scenarios, highlighting the need for a balanced approach that considers material properties, joint design, and service conditions.
- The yield and tensile strengths of the base metal contribute similarly to fatigue performance, yet the critical factors influencing fatigue life are NOT consistent between DP and MS steels.
- DP steels demonstrated higher fatigue resistance compared to MS steels. This suggests that while MS steels are suitable for applications requiring high strength, they may not be ideal for components subjected to high cyclic loads.
- Optimizing weld geometry, controlling stress concentrations, and understanding localized material properties, particularly the hardness at the tongue, are essential for improving HCF performance.
- Selecting ultra-high-strength steels does not guarantee improved performance; proper RSW design, material compatibility, and loading conditions matter.
- The analysis of fatigue crack nucleation and propagation underscores the complexity of these processes and the need to address competing failure modes through improved joint design and material selection, ensuring more predictable and durable welded structures.
- A typical fatigue behavior where increased load ranges correlated with reduced cycles to failure, establishing a fatigue limit beyond which materials could theoretically withstand infinite cycles without failure.
- The HCF results aligned with the hardness results at the tongue, confirming a correlation emphasize that steel grade affects HCF performance.

10. DYNAMIC LOADING CAPACITY OF DP RSW

A new approach to dynamic testing has been introduced, accompanied by the development of specialized equipment for impact-bending tests. This innovation provides precise numerical results to quantify the resistance of spot-welded joints under dynamic loading conditions. This method is used to evaluate resistance spot-welded joints made on DP600 and DP800 steels with three different technological parameters, comparing long-time welding, short-time welding, and 2-pulse welding. According to the literature overview, there are several trials to find a good method to determine the behaviour of resistance spot welded joints during dynamic loading. A developed instrumented impact-bending test was used to investigate these properties, where the loading direction is similar to in the case of a car crash. RSW joints are subjected to dynamic loads during their lifetime, either randomly or as a result of an extraordinary event (e.g., crash), and thus should be welded with welding parameters that are also optimized for dynamic loads, so in this investigation, different RSW joints were compared on DP600 and DP800 steels.

10.1. Testing method

It is important to know the absorbed impact energy and also need to know the area under the curve of the force-time diagrams, as well as the shape of the curve, to determine the deformation behaviour of spot-welded joints made of high-strength steels. However, this requires an instrumental impact test of the spot-welded joints on the overlapped thin sheets. In order to get a more accurate and thorough picture of the dynamic behaviour of spot-welded joints in automotive steel sheets, a special instrumented testing method was developed.

Figure 10.1 depicts the setup for an instrumented impact test, a method used to evaluate the toughness and fracture behavior of materials under dynamic loading. In this setup, a pendulum swings down, with its striker impacting the specimen held firmly in a specimen holder. During the impact, a strain gauge attached to the striker measures the force applied to the specimen. This force is converted into an electrical voltage signal that represents the magnitude of the impact force. Simultaneously, triggering flags attached to the pendulum pass through a photogate, which measures the time intervals during the pendulum's striking motion. The signals from both the strain gauge and the photogate are sent to an amplifier, which boosts their strength to ensure accurate interpretation. Finally, these amplified signals are processed by an oscilloscope, which plots a force-time diagram. This diagram provides critical insights, such as the maximum force applied, the duration of impact, and the energy absorbed by the specimen during fracture. The setup integrates mechanical motion with precise electronic measurement, enabling a detailed analysis of material properties.

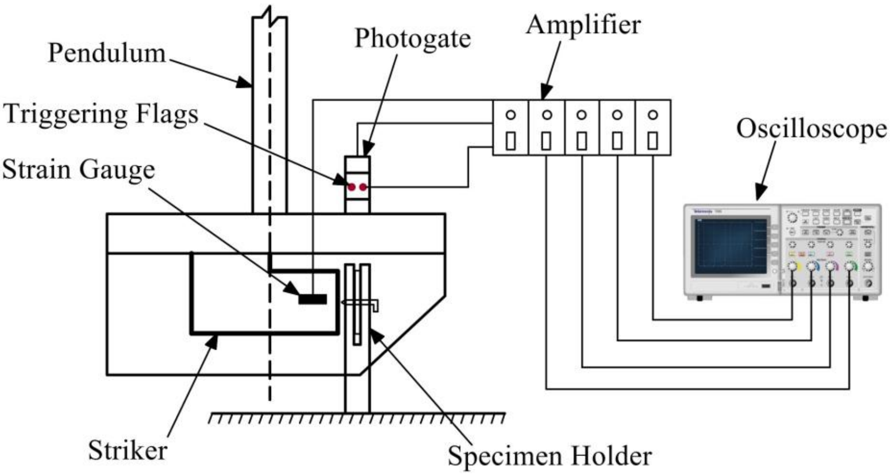

Figure 10.1 Instrumented RSW impact test setup

The usual impact velocity of the Charpy test is 3-6 m/s [214][215][216]. The kinetic energy is used for the forming of the specimens and the breaking of the joints during the dynamic (three-point) bending that causes the specimens to fail. The pendulum hammer with m = 19.794 kg falling weight and a height of fall h = 1.545 m used for conventional standard tests has a maximum impact energy of 300 J with an impact velocity of 5.5 m/s. However, the experience of the preliminary experiments showed that even for 1 mm + 1 mm overlapped joints of high-strength DP steels, this falling weight and the maximum impact energy of 300 J are too high, so the Charpy impact test machine was modified to measure the force, a strain gauge was placed in the impact edge of the striker and the weight of the hammer was reduced, thus the maximum impact energy was changed to 118.25 J. To examine the spot-welded joints as accurately as possible, the design is also modified as shown in *Figure 10.2*.

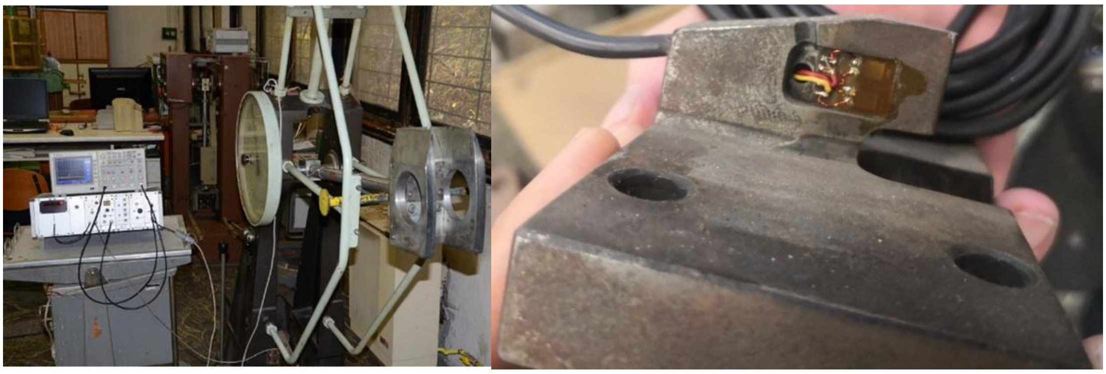

Figure 10.2. The testing equipment and the modified hammer [71]

During the development of the geometry of the specimen, an optimal bridge width was determined, which can provide an overall view of the dynamic behaviour of the whole welded joint (nugget + heat-affected zone + base material), considering the avoidance of base material failure around the fixing points. The results of the initial experiments showed that the effect of the base material on the test result is still quite negligible at a bridge width of 20 mm. The specimen geometry and the prepared specimen are shown in *Figure 10.3* [71].

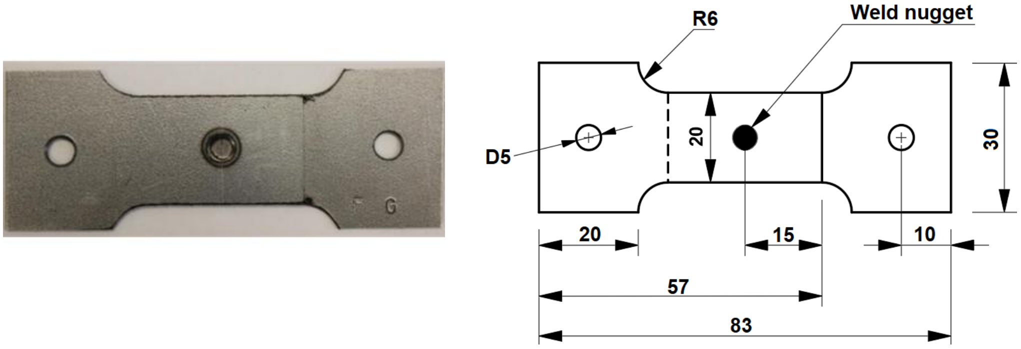

Figure 10.3. The prepared specimen and its geometry [71].

Due to the specimen geometry, it was also necessary to design and manufacture a new specimen holder, that would be suitable for holding the spot-welded specimen. The new specimen holder developed for the test is shown in *Figure 10.4*.

Figure 10.4. The new RSW specimen's holder [71].

Figure 10.5 shows a schematic drawing of how this method works and the behaviour of the specimen failure during striking.

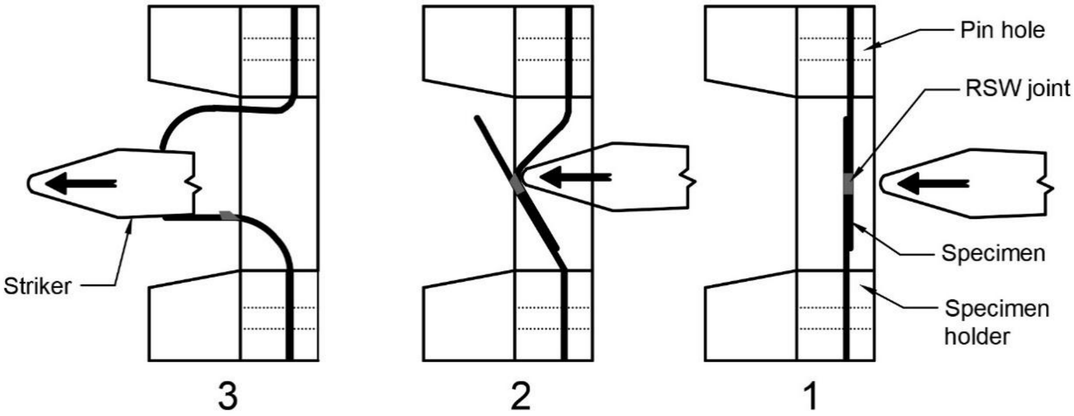

Figure 10.5. Schematic drawing of impact-bending test: (1) the specimen is fixed in the specimen holder, (2) the striker hits the specimen, (3) the striker goes through the specimen and causes weld plug and base material bending.

10.2. RSW sample preparation

In our study, sheets of 1 mm sheets thickness of two different grades of SSAB Docol DP steels (DP600 and DP800) were used as a base material in RSW joints. The chemical and mechanical properties provided by the manufacturer in material certificates are shown in *Table 7.1* and *Table 7.2*.

In this experiment, three different welding technologies were applied to the two steel grades. After preliminary experiments, long-time welding with high welding current and welding force (No. 1), 2-pulse welding with lower welding force (No. 2), and short-time welding with lower welding force (No. 3) were used. The cooling time means the time between pulses in the case of 2-pulse welding. *Table 8.1* shows the welding parameters of the used RSW technologies (long-time, 2-pulse, and short-time).

For the impact-bending test, the previously described method was used. For the impact testing, eleven specimens were made for the investigation of the same welding technology in one base material, which means a total of 66 tested specimens. The tests were performed at 25 °C room temperature.

10.3. Results and discussions

This test is very fast, so a high sample rate was necessary for the determination of force-time diagrams during the fracture. The sample time was 5 ms and 2500 samples were made within this time. This high sampling rate gave exact results. *Figure 10.6* shows the three typical failures of the spot-welded joints. In the case of long-time welding base material failure occurs instead of button pull failure, while in other cases the spots failed in pull-out with different sizes. The partial pull-out and full failure modes are typical failures on resistance spot welded joints and have been reported in several publications [217][218][219][220].

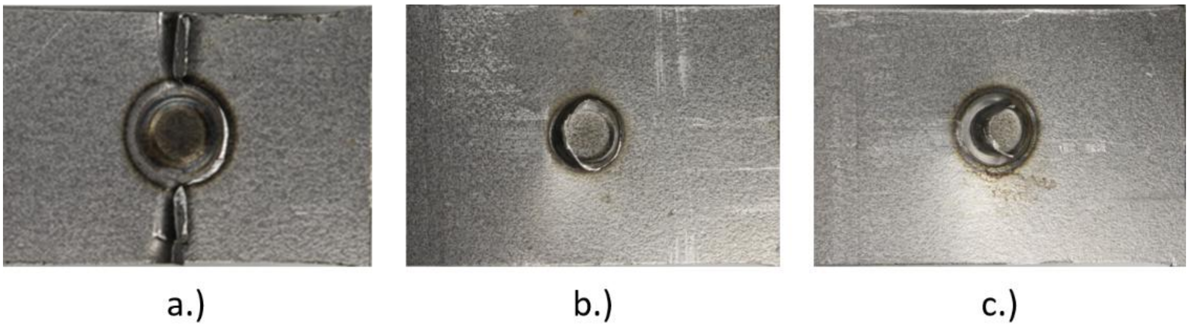
a.)
b.)
c.)

Figure 10.6. Typical failure modes: (a) "half" plugging with base material failure (long-time welding), (b) fully plugged (2-pulses technology), (c) partially plugged (short-time welding)

In *Table 10.1* the impact-bending test results of DP600 are summarized and statistically evaluated. In every case, the impact energy and the maximum impact force were measured. Standard deviations (SD) and the coefficient of standard deviations (SD_c) were calculated. The plug diameters (after the test) were measured on the fractured specimens, perpendicularly to the hammer edge.

Table 10.1. Impact-bending test results of RSW joints on DP600

Welding technology	Average impact energy (J)	SD of impact energy (J)	SDc of impact energy (%)	Average impact force (kN)	SD of impact force (kN)	SDc of impact force (%)	Plug diameter (mm)
Long-time	65.95	2.99	4.54	9.97	1.28	12.84	7.4 – 7.7*
2-pulse	36.31	1.50	4.14	5.74	0.52	9.07	4.5 – 5.1
Short-time	34.31	1.05	3.26	5.05	0.21	4.29	3.7 – 4.1

* Only one side can be measured due to the base material failure

The results of resistance spot-welded DP600 show that there are big differences between the long-time welding and the other two technologies for both impact energy and maximum impact forces. The short-time welding shows the worst results, but the deviation is the lowest.

There are slight differences in impact energy and maximum impact force between short-time welding and 2-pulse welding; however, the plug diameter differs significantly. Generally, the standard deviations of all results are acceptable. *Figure 10.7* shows the impact force-time curves of these tests.

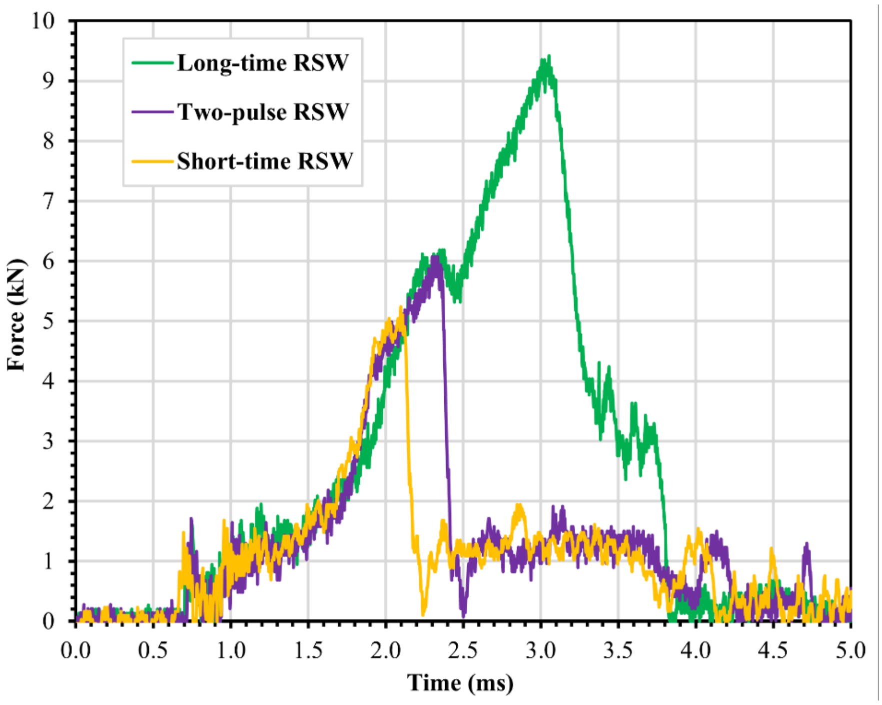

Figure 10.7. Impact force – time curves on DP600 welded by different welding parameters

The explanation of the curve:

- the first phase from 0 to 0.7 ms shows nothing important because the hammer has not yet reached the specimen.
- the second phase from 0.7 to 1.5 ms: the hammer reaches the specimen, the base material forming, but no fracture,
- the third phase from 1.5 to the end of wave: FZ fracture (in the case of long-time welding half FZ, half base material),

- the last phase from the end of wave to 5 ms: base material forming after FZ fracture.

The curves clearly show the differences in impact energies especially in the case of long-time welding. The curve of long-time welding (grey) shows two waves of maximum forces, the first wave shows the half-broken spot, and the bigger second wave is the base material failure. The difference between short-time welding (blue) and 2-pulse welding (orange) is clearly seen; the 2-pulse welding shows better maximum impact force and better elongation too. *Table 10.2* shows the results for the DP800 base material.

Table 10.2. Impact-bending test results of resistance spot welds on DP800

Welding technology	Average impact energy (J)	SD of impact energy (J)	SDc of impact energy (%)	Average impact force (kN)	SD of impact force (kN)	SDc of impact force (%)	Plug diameter (mm)
Long-time	60.95	3.96	6.49	9.55	0.93	9.75	7.2 – 7.6*
2-pulse	50.77	3.36	6.63	7.79	0.44	5.64	4.3 – 4.8
Short-time	41.18	1.90	4.62	6.49	0.34	5.34	3.7 – 4.1

* only one side can be measured due to the base material failure

Both impact energy and maximum impact force show clear differences between the welding technologies. Short-time welding is the worst, with low values for both impact energy and impact force. 2-pulse welding is much better, and long-time welding is again the best. The standard deviations are good in all cases, for both impact energy and impact force too. *Figure 10.8* shows the impact force-time curves of the three technologies for the DP800 base material.

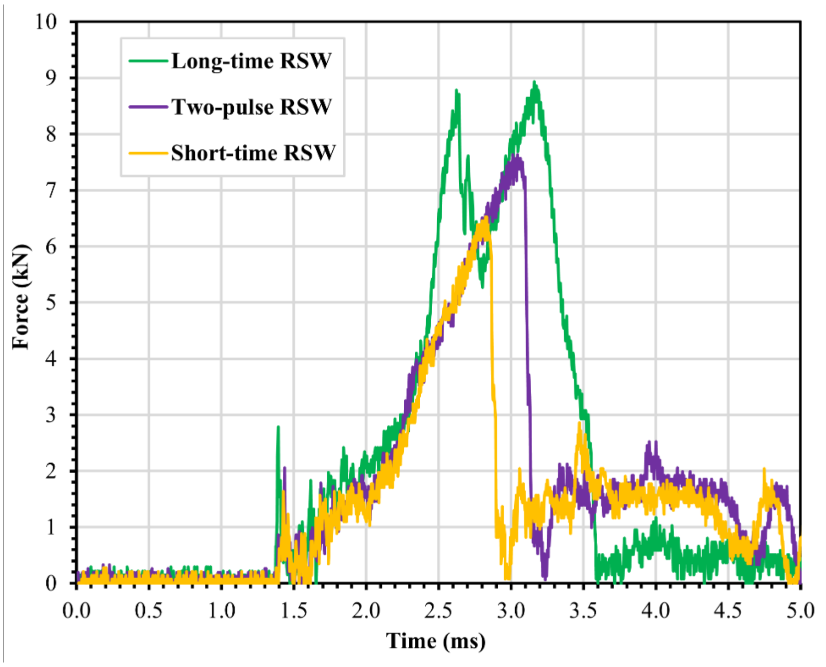

Figure 10.8. Impact force – time curves on DP800 welded by different welding parameters

The curves clearly show the differences in maximum impact forces as well as time differences. The shape of the long-time welding curve is somewhat different than that of DP600. The long-time welding curve shows two well-separated waves, and it can be assumed that the first wave is caused by the failure of the half joint, while the second wave occurs because the base material has broken. As expected, the short-time welding shows the worst results.

Table 10.3 illustrate the comparison of the impact resistance of RSW joints across the DP steel, highlighting both their average performance and the consistency of that performance. The curves shows how much energy the welds can absorb before failing under impact, showing that DP1000 and DP600 exhibit similar average impact energy (65.23J and 65.95J, respectively) while DP800 absorbs less impact energy on average (60.95J). The consistency of these results, with DP600 welds showing the least variation in impact energy and the highest variation in the impact force. DP1000 demands more force for it to break (10.78 kN).

Table 10.3. Impact-bending test results of long-time RSW

Steel grade	Average impact energy (J)	SD of impact energy (J)	SDc of impact energy (%)	Average impact force (kN)	SD of impact force (kN)	SDc of impact force (%)
DP1000	65.23	5.22	8.00	10.78	1.09	10.11
DP800	60.95	3.96	6.49	9.55	0.93	9.75
DP600	65.95	2.99	4.54	9.97	1.28	12.84

To investigate the effect of the RSW parameter on impact performance, a long-time technological parameter was applied to DP steel grades (DP600, DP800, and DP1000). *Figure 10.9* illustrate the impact force over time for each material during the test. DP1000 exhibits the highest peak force, followed closely by DP800 and DP600. The DP600 material demonstrates a more gradual force and a relatively sustained peak before a rapid drop, while DP1000 and DP800 display sharper increases and decreases in force. These variations highlight the distinct mechanical responses of each material under impact loading, with higher-strength steels showing greater resistance before failure.

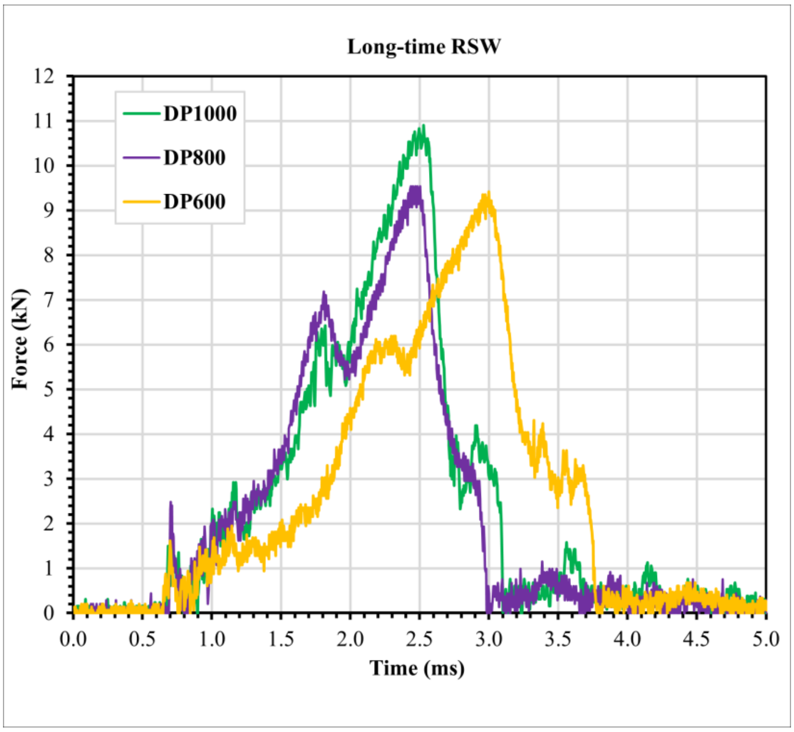

Figure 10.9. Impact force – time curves on samples welded by Long-time RSW parameter.

From the impact-bending tests, three absolutely different failure modes can be distinguished, which clearly depend on the applied welding technology. To check where the failure occurs in the joints, cross-sectional macroscopic tests were made. *Figure 10.10*, *Figure 10.11* and *Figure 10.12* show the cross-sections and hardness curves of RSW joints made by respectively long-time, 2-pulse, and short-time welding, respectively. Below the cross-sections and hardness curves, the cross-sections of the impact-bending tested specimens can be seen. All cross-sections and hardness measurements were made on DP800 base material. The Vickers hardness measurements were made by a Mitutoyo microhardness tester, the loading was 200g and the distance between measurements was 0.2 mm.

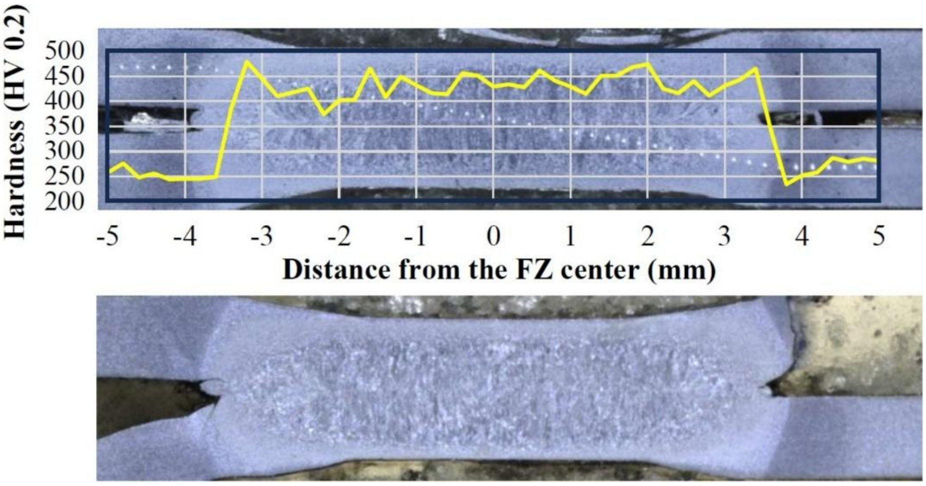

Figure 10.10. Cross-section of long-time welding technology on DP800 before (above, with hardness curve) and after (below) impact-bending test

In the case of long-time welding, the fracture occured in the outer part of the HAZ (which is called the SCHAZ, and it continued on the base material. Because of this, only one side fracture can be seen in *Figure 10.10*. Based on hardness distribution values, this is the most softened area, so the resistance against dynamic loading is the smallest here (252 HV). Basically, the value of softening and the plug diameter determine the maximum impact force in this case.

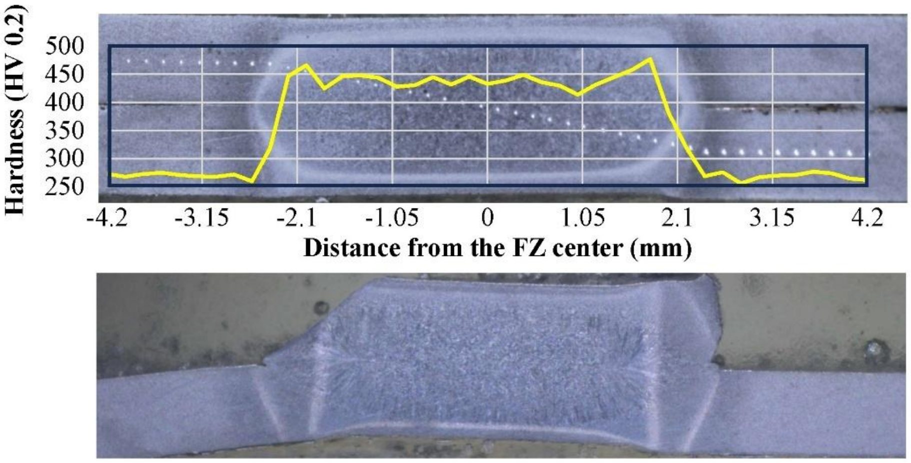

Figure 10.11. Cross-section of 2-pulse welding technology on DP800 before (above, with hardness curve) and after (below) impact-bending test

Figure 10.11 shows the hardness distribution and the failure of 2-pulse welding specimens. The hardness distribution is similar to that of the long-time welding technology, but in the SCHAZ, the hardness is slightly higher. The fracture was started in the same place on the right side of the photo, the hardness is a little bit higher here, than for long-time welding (276 HV). The left side shows the end of the fracture. There is a clear difference between the 2 sides, on the left side the crack is not perpendicular to the sheet surface. This is because the direction of loading changed during the test and shearing happened on the left side. Here the crack goes from the HAZ to the FZ, so the crack direction is determined by the loading direction, and the hardness has no effect on this.

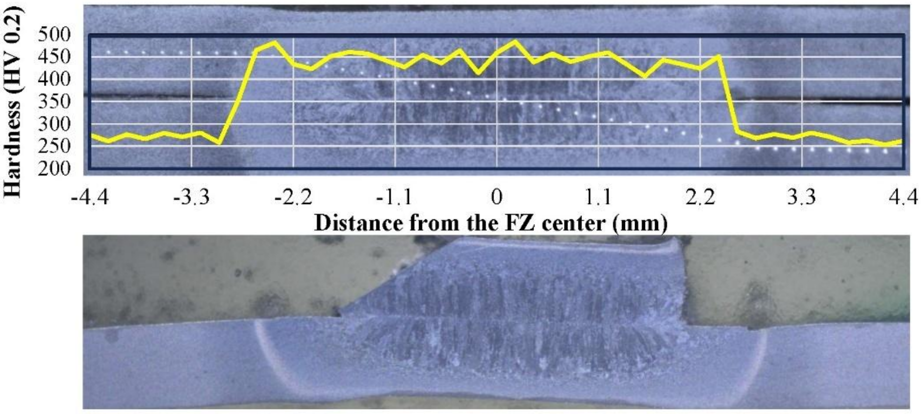

Figure 10.12. Cross-sections of short-time welding technology on DP800 before (above, with hardness curve) and after (below) impact-bending test

In the case of short-time welding technology, the hardness distribution is similar to that of 2-pulse welding, but the failure started from the edge of FZ and finished in the FZ too, so it is a partial weld button. *Figure 10.12* shows the hardness distribution and the failure of short-time welding specimens. This can be caused by imperfect fusion on the edge of the FZ. The shape of the left side is similar to that of 2-pulse welding, but the plugged diameter is the smallest, so it causes the worst result of the impact-bending test.

10.4. Conclusion

Based on the experimental results, the following conclusions can be drawn:

- It can be stated that the developed impact-bending test method can be applied to compare different RSW technologies and/or different base materials.
- The bigger diameter nugget requires a bigger width of the base material in the impact zone. Therefore, the data for the 7.2 mm nugget diameter do not show the exact results, however, the best results come from this type of weld.
- In terms of impact energy there are significant differences between the three technological combinations on DP800.
- For DP600, short-time welding has shown the lowest impact force results, followed by 2-pulse welding, while long-time welding produced the best outcomes.

- The plugged weld diameter is not correlated with the impact energy and impact force for 2-pulse welding. The plugged diameter is significantly smaller in short-time welding, but this does not cause so much impact force and impact energy loss in the case of DP600.
- The RSW joints of DP800 show bigger differences between technological parameter combinations. It clearly identified that short-time welding has the worst resistance against impact loading, 2-pulse welding is next, and long-time welding has the best results. The impact energies and impact forces are almost perfectly correlated with the FZ diameters.
- Three typical failure modes occur during the tests. In the case of 2-pulse welding and long-time welding of DP800, the failures start from the HAZ in the most softened part. In the case of short-time welding, the failure starts from the FZ.
- All test results show that bigger FZ diameters cause better impact energies and impact forces, but the differences are not perfectly correlated.

11. PHYSICAL HEAT CYCLE MEASUREMENT OF RSW

Heat cycle measurement (HCM) demonstrates the welding consequences in terms of the change in mechanical properties and microstructural formations. The accuracy of cooling rate measurements including $t_{8/5}$ cooling time is very important to predict the microstructural evolution in the HAZ, however, the thermocouple measurement raises numerous challenges due to the high temperature gradient and small weld and HAZ size.

Difficulties were encountered in the experimental work as a result of the instantaneous welding time and the vibration resulting from the passage of alternating electrical current between the two electrodes. A magnetic field is generated that affects the thermocouple measurement and appears as a noisy curve that is filtered out and smoothed. Joule heat, interfacial heat generation, and cooling effects of electrodes are also considered in the experiment.

11.1. Materials and methods

Docol MS1400 steel sheets with a thickness of 1 mm were used as a BM in our experimental study of HCM. The chemical composition and mechanical properties of MS1400 are shown in *Table 7.1* and *Table 7.2*, respectively. The RSW process was performed according to chapter 5.0

The sample's geometry comprises a base sheet with dimensions of 100×30 mm, both the thermocouple sheet and the confining sheet, measuring 50×30 mm each, interface with this base sheet. The thermocouple sheet incorporates the RSW within the base sheet. Positioned directly opposite the thermocouple sheet, the confining sheet has a notch facing the thermocouple to minimize interference. The notch is filled with an insulating filler material to prevent the heat generated by the RSW from radiating beyond the boundaries of the heat-affected subzones, where the heat cycle is to be measured. *Figure 11.1* shows the geometrical parameters of the HCM samples.

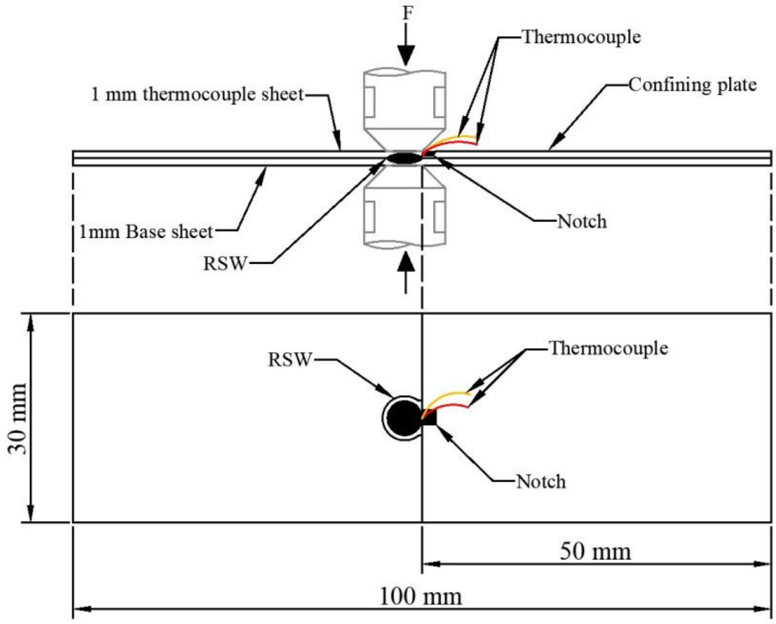

Figure 11.1. Experimental setup for thermocouple measurement

The sample geometry design's objective is to encase the FZ, preventing both expulsion and bulging that result from RSW at the edge. *Figure 11.2* shows the bulge and expulsion as a result of edge welding. A beaded micro K-type thermocouple (Chromel/Alumel) is welded onto the cross-section centre of the thermocouple sheet using a specialized micro-thermocouple welding device, see *Figure 11.3*.

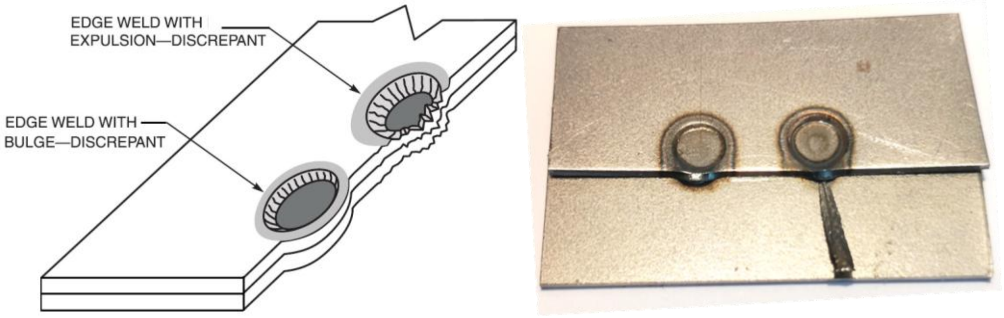

Figure 11.2. Edge RSW results schematic drawing left [221], bulge and expulsion during an experiment without confining plate in the right.

Several samples were conducted in such a way that the electrodes are positioned at a location that results in RSW, where the HAZ intended for measuring the heat cycle encompasses the thermocouple. In the HAZ, as presented in *Figure A5.1*, *Figure A5.2*, and *Figure A5.3* in Appendix A5 thermal cycles were measured using K-type thermocouples, which were embedded inside the base materials in different positions of the HAZ. The thermocouples were welded to the sheet (not on the surface, but inside the base material) and positioned near the weld. This ensured accurate measurement of the thermal cycles in various parts of the HAZ.

It was necessary to place the thermocouples away from the immediate vicinity of the weld to avoid interference from high currents and electromagnetic fields. For each welding technology, three thermal cycles were measured, in the UCHAZ, in the ICHAZ, and in the SCHAZ.

To determine the exact zone for the measured heat cycle, a microscopic examination of the RSW cross-section was conducted, revealing the FZ and the heat-affected subzones. The distance from the thermocouple to the centre of the nugget was measured and compared symmetrically to the opposite side of the FZ with the same distance, as the heat conduction transferred symmetrically from the FZ up to the thermocouple. The quality of spot weld formation is determined by the thermal symmetry in the place of the weld formation [222]. *Figure 11.3* shows the thermocouple welding process.

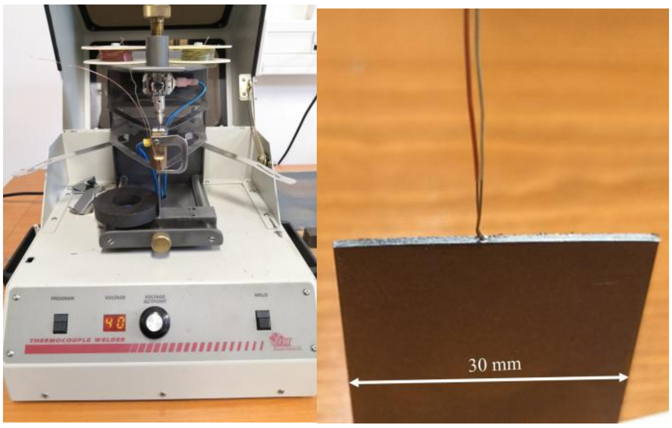

Figure 11.3. Thermocouple weld device in left and welded micro K-type thermocouple in right

A series of measures were taken to reduce the noise arising from vibration and the magnetic field generated due to RSW. These attempts include shortening the thermocouple and insulating it from the electromagnetic field (EMF) by passing it through the least magnetic field space possible. The heat cycle was measured using the HBM Spider8 modular acquisition system. Its high-speed data acquisition capability makes it ideal for measuring thermal changes that occur rapidly over time as in RSW. All measurements were conducted at room temperature and the acquired HCM were filtered out and smoothed by Excel. Two RSW welding technologies were applied on 1 mm MS MS1400 high-strength steels, a 2-pulse and a long-time technology. The welding parameters are presented in *Table 8.1*. *Figure 11.4* shows HCM samples for 2-pulse RSW and long-time RSW after measurements.

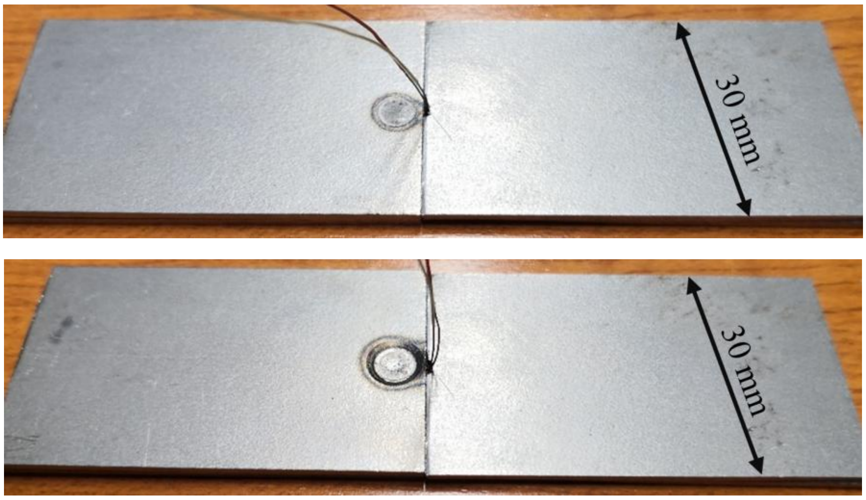

Figure 11.4. HCM sample for 2-pulse RSW on the upper side and for long-time RSW on the lower side

11.2.Investigating mechanical properties of RSW joints

While short-time welding leads to minimal softening in the HAZ, long-time welding is favoured as it produces a larger FZ size with the same electrode tip diameter and welding parameters. This larger FZ size compensates for the softening effect. In general, superior outcomes have been achieved with the long-time methods [51][223].

In both welding techniques, three distinct heat cycles were recorded at the UCHAZ, ICHAZ, and SCHAZ. *Figure A5.1, Figure A5.2, and Figure A5.3* in Appendix A5 show schematic drawings of the heat-affected subzones resulting from the HCM, the thermocouple positions for the 2-pulse (short time) RSW, and long-time RSW technologies are shown too. The hardness distribution of the RSW joint cross-section of 1 mm MS1400 shows notable variations in hardness values between single-pulse and 2-pulse welding. Substantial softening occurs in the FZ during 2-pulse RSW, a result of the heat treatment effect from the second pulse. The hardness distribution of 1 mm MS1400 RSW in both technologies is illustrated in Appendix A2.

In addition to the hardness test, the welding parameters are optimized based on the tensile-shear (T-S) test and FZ dimensions. The tensile-shear load-displacement results of long-time and 2-pulse RSW parameters are shown in *Table 8.2*. The T-S test results have shown lower strength and displacement compared to long-time RSW samples. These results with two RSW technologies produced two different FZ diameters where the lower diameter of the 2-pulse RSW is 1.24 mm less than the long-time RSW, see *Figure 11.5* and *Figure 11.6*.

11.3. Results and discussion

In a long-time RSW, the duration of the electrical current application is extended. This results in more heat in the weld zone. While this can ensure better fusion, especially in thicker materials, it also carries risks such as base material degradation. The longer the metal remains at high temperatures, the more pronounced to the thermal gradients. This can lead to the build-up of residual stresses, which can impact the structural integrity of the weld and surrounding material.

HCMs have shown that the peak temperature reached during the long-time RSW was considerably high, approaching the melting point of steel. The cooling rate was relatively slow, allowing for larger grain growth in the HAZ. The FZ was observed to be large with visible grain growth. The HAZ in steel welding can be broadly divided into multiple subzones, primarily based on the temperature reached during welding and the resulting microstructural changes. The size of the HAZ subzones is a direct reflection of the heat input and control in the RSW process. While long-time RSW might produce broader HAZ subzones due to the extended heat application, the 2-pulse RSW method typically results in narrower and more controlled HAZ subzones, primarily due to the second-pulse intermediary cooling phase and the ability to regulate the heat input better.

Figure A5.1, *Figure A5.2*, and *Figure A5.3* in Appendix A5 show schematic drawings for HCM samples and the heat-affected subzones size. The peak temperature in the 2-pulse RSW was also high, but slightly lower than that of the long-time RSW due to the shorter time at elevated temperatures between pulses. Comparison between the measured maximum heat at specific points may be inaccurate due to the heat value varying within the heat-affected subzone, especially in RSW, due to the small size of the weld. The cooling rate was notably faster between the pulses, which hindered excessive grain growth in the HAZ. *Figure 11.5* and *Figure 11.6* show the HCM results at the heat-affected subzones of the two RSW technologies. At UCHAZ The cooling rate in 2-pulse RSW (7500°C/s) is five times faster than the long-time RSW (1500 °C/s). The cooling time from 800 °C to 500 °C ($t_{8/5}$) of 2-pulse RSW at UCHAZ is 0.04 s and 0.2 s of the long-time welding. The FZ was smaller as compared to the long-time RSW with more refined grain structures.

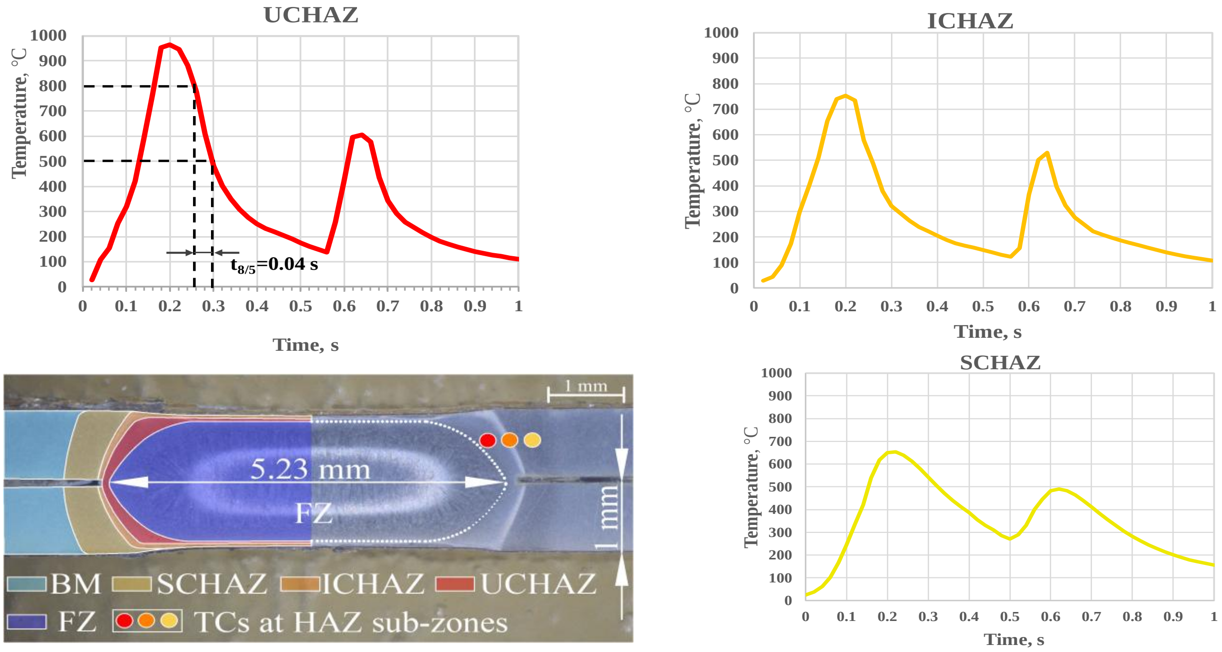

Figure 11.5. HCM of 2-pulse RSW at heat-affected subzone (1 mm MS1400).

In the first pulse, it is clear from the HCM figures that the cooling time at the heat-affected subzones in 2-pulse RSW is less than their counterparts welded with long-time RSW. The second pulse is considered as a reheating to improve the mechanical properties of the RSW. However, in long-time welding, it is clear that the diameter of the FZ is larger. The superiority in the T-S test, as mentioned earlier, is attributed significantly to the difference in the spot weld size.

By comparing the heat cycle measurements shown in *Figure 11.5* and *Figure 11.6*. obtained from physical measurements with those generated using the FEM for RSW, as shown in *Figure 12.2* and *Figure 12.3*, under the same welding parameters and conditions, a significant similarity was observed in the HAZ-subzones.

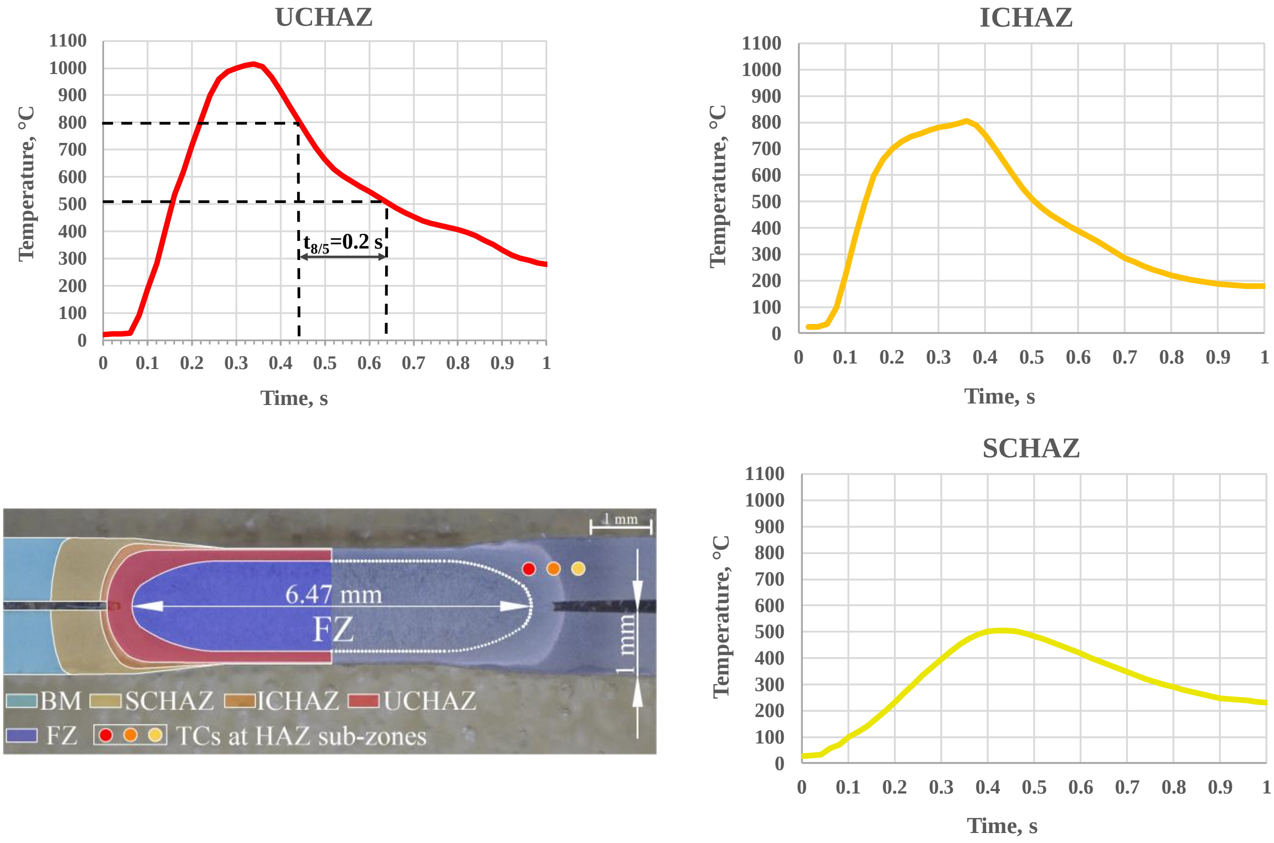

Figure 11.6. HCM of long-time RSW at heat-affected subzones (1 mm MS1400).

Rapid heating and cooling, especially in long-time RSW, can introduce significant thermal gradients, leading to residual stresses and possible distortion of the welded components. The essential feature of the 2-pulse method is the short cooling interval between the two pulses. This brief cooling period allows the FZ to solidify partially before the second pulse, which refines the grain structure. The distribution of heat in the 2-pulse method is more controlled. The first pulse primarily serves to heat the material, while the second pulse ensures proper fusion. The temperature gradient plays a crucial role in determining the mechanical properties of the welded joint. In a long-time RSW, the peak temperature reached very close to the melting point of steel at UCHAZ, which can lead to excessive grain growth and reduce the toughness of the welded joint [224].

The rapid cooling in the 2-pulse RSW method reduces the time available for grain growth in the HAZ. Smaller and more refined grains generally yield better mechanical properties in steel. A larger FZ, as seen in the long-time RSW, can be beneficial for certain applications requiring higher load-bearing capacities. However, it is essential to ensure that the grain size within the nugget is controlled to prevent embrittlement. Further tests would be needed to measure the tensile strength, hardness, and impact toughness of the joints produced by both methods. The 2-pulse method, with its quicker cooling rate, might be more suitable for applications requiring refined grain structures and superior mechanical properties. In contrast, the long-time RSW might be more appropriate for applications where the size of the FZ is more critical than the grain structure.

11.4. Conclusion

The heat cycle of long-time and double-pulse RSW welding was successfully physically measured using a thermocouple in the depth of HAZ sub-zones. The following conclusions can be drawn:

- Thermocouple measurements in depth of the heat cycle in the RSW of steels revealed distinct differences between long-time and 2-pulse welding techniques. Long-time RSW exhibited a prolonged and steady rise in temperature, resulting in a broader HAZ due to the extended heat application. On the other hand, the 2-pulse method demonstrated a more controlled heat input, with an intermediary cooling phase, considering these observations, the 2-pulse RSW appears to offer better control over the weld's thermal profile, potentially leading to superior weld quality in steel joints.
- Thermal history captured by thermocouples successfully validated the thermal FEM modeling in Chapter 9, where a heat cycle similarity between the two methods was found in the HAZ.

12. HEAT CYCLE MODELLING OF RSW

A thermal simulation of the RSW process was conducted using a two-dimensional (2D) axisymmetric finite element model (FEM) developed with the software, SYSWELD, to simulate temperature distributions for two welding technological parameters, single pulse long-time and double pulse weld various weld stages, and to evaluate the effects of welding parameters such as current, time, and electrode force.

The input data (electrode shape, plate thickness, and welding parameters) used in the simulation is identical to the experiments conducted previously in physical thermal measurement research to validate the simulation outcomes and demonstrate the consistency between predicted and observed thermal cycle under RSW conditions.

12.1.Materials and methods

The thermal cycle within the FZ was simulated using the FEM, while direct measurements were taken in the different heat-affected subzones. For the numerical simulation, Sysweld software (ESI group) was used, which features a special RSW module. In this module, the accurate input of welding parameters and geometries (electrode and sheet metal) can be used. A 2-dimensional model was selected for the simulation due to the round-shaped weld joint. Both quadratic and triangular element shapes were used, with varying element sizes, smaller elements for the FZ, and larger elements for the HAZ and base material.

Two-dimensional axisymmetric thermal-electrical (transient heat conduction) FEM was applied to simulate the welding process of DP600 steel with 1 mm thickness, using the SYSWELD finite element software. The chemical composition and the mechanical properties of DP600 a product of SSAB are shown in *Table 7.1* and *Table 7.2*, respectively. The 2-pulse and long-time welding parameters used in both experiments and simulations are listed in *Table 8.1*.

These distinct parameters were chosen to investigate their influence on the microstructural characteristics and mechanical properties of the welded joints, particularly focusing on the trade-offs between FZ size and softening in the HAZ (see Chapter 11.)

12.2.Finite element modelling (FEM)

The FEM model was employed to simulate the RSW process to quantitatively understand the effects of the process parameters on temperature distribution at two different welding technological parameters (long-time single pulse and double pulse). Temperature-dependent physical and mechanical properties of materials, including thermal conductivity, coefficient of thermal expansion, electrical resistance, specific heat, density, enthalpy, elasticity of yield stress, and Poisson’s ratio, were implemented for electro-thermal RSW simulation. The temperature distribution was considered an increment from fully coupled electrical thermal FEA. The electrical and thermal boundary conditions were also considered in the model. Although the nature of the heat flow is three-dimensional, it can also be simulated in the form of the two-dimensional axisymmetric model, because the circular section of the electrode can be applied to both current and compressive force at the same time [225].

12.3. Results and discussion

The simulation outcomes present visual analyses of thermal cycle histories during RSW, showcasing temperature distributions in contour plots and graphs depicting temperature vs time curves for different zones under double-pulse and long-time welding conditions, facilitating an in-depth examination of heat propagation and dissipation.

In a 2-pulse weld simulation, the contour plot indicates temperature distribution in the workpiece, with a temperature scale on the left ranging from approximately 12 °C to over 1600 °C. The hottest region, shown in magenta and red, corresponds to the FZ, with peak temperatures above 1600 °C. This region is where melting and potential fusion occur, forming the core of the weld. Surrounding the FZ there are HAZs depicted in gradient colors (orange, yellow, and green). These areas experience significant temperature exposure but remain below the melting point, affecting the microstructure without full melting. The contour plot also indicates how far the heat extends into the surrounding material, transitioning to lower temperatures (blue areas) as the distance from the weld center increases. *Figure 12.1*b shows a simulation of a 2-pulse RSW process.

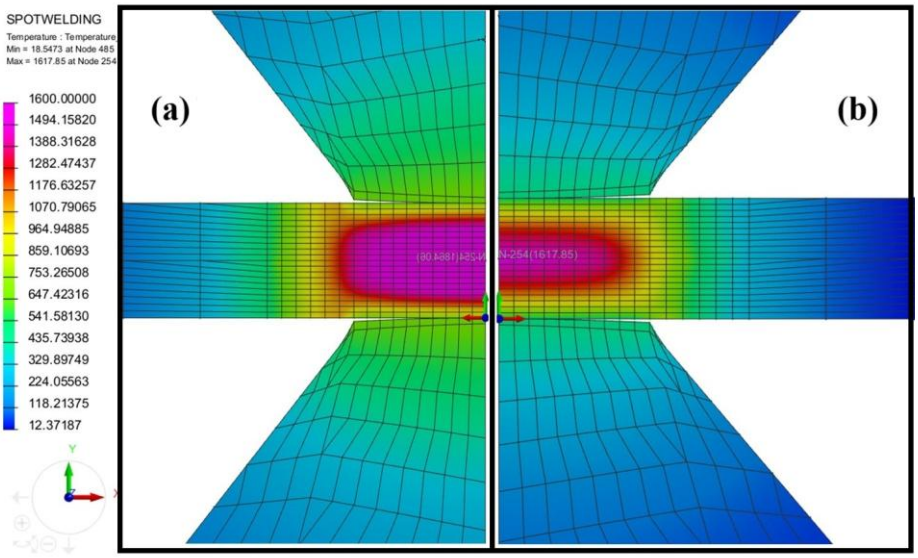

Figure 12.1.(A) Simulation of a long-time RSW, (B) Simulation of a 2-pulse RSW process.

In long-time weld simulation, the temperature profile in this case exhibits a broader and more uniform distribution compared to the 2-pulse weld. The FZ still has the highest temperature region, indicated by magenta and red, but the heat spreads further into the material, shown by the wider extent of orange and yellow colors. The maximum temperature is similarly high (above 1600 °C), but the longer heating duration allows for greater heat penetration and slower cooling throughout the material. HAZ extends further, with gradual temperature gradients transitioning from the FZ high temperature to lower temperatures across the workpiece. *Figure 12.1*a shows a simulation of a long-time RSW process.

As can be seen in *Figure 12.2*, in the case of the double-pulse weld thermal cycle history, the red curve (FZ) shows two significant temperature peaks, indicating the application of two distinct heating pulses. The highest peak surpasses 1500 °C, representing the molten state of the FZ. The other zones (UCHAZ, ICHAZ, and SCHAZ) experience smaller, smoother temperature profiles. The UCHAZ reaches a notable peak temperature above 1000 °C, while the ICHAZ and SCHAZ have progressively lower peaks, indicating less heat influence as the distance from the weld center increases. The thermal cycle of the FZ demonstrates rapid heating and cooling during the first pulse, followed by a secondary heating pulse, which contributes to reinforcing the weld.

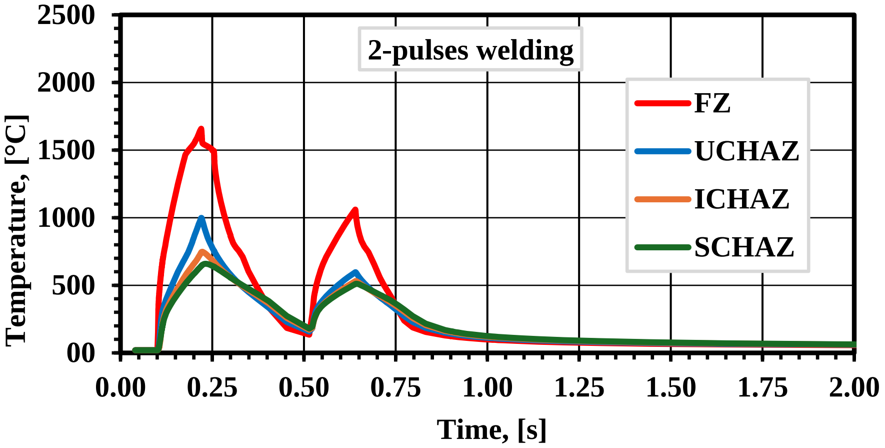

Figure 12.2. Thermal cycle history of different zones in double-pulse RSW.

As shown in *Figure 12.3*, in the case of the long-time weld thermal cycle history, the red curve (FZ) has a single, substantial temperature peak that exceeds 2000 °C, showing a continuous heating phase indicative of a longer welding cycle. The UCHAZ, ICHAZ, and SCHAZ curves reflect different levels of heat penetration. The UCHAZ reaches approximately 1000 °C, implying significant thermal exposure but less than the FZ. The ICHAZ and SCHAZ curves peak at progressively lower temperatures, with SCHAZ remaining below 500 °C. The longer duration of heat application results in slower cooling rates, especially noticeable in the UCHAZ and SCHAZ curves. This sustained heat allows more extensive microstructural changes to occur in the HAZ. The long-time welding approach results in a higher peak temperature for the FZ and more gradual cooling for the HAZs than double pulse weld, potentially leading to larger HAZ and greater microstructural transformations.

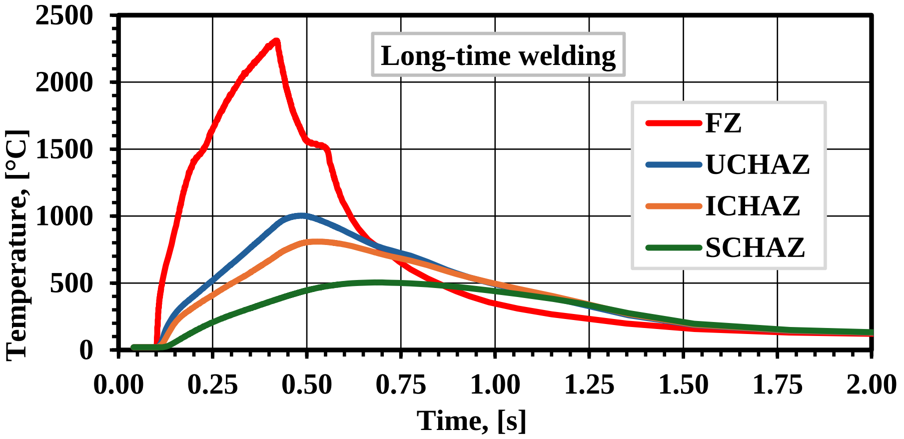

Figure 12.3. Thermal cycle history of different zones in long-time RSW.

These thermal cycle diagrams can help to understand the thermal gradients and cooling rates during different welding processes, which are crucial for predicting the resulting microstructure and mechanical properties of the weld.

The thermal cycle history of the RSW double-pulse and long-time process from the FEM model has been compared with the experimental physical thermal cycle measurement result of the author [178]. A big similarity was found regarding the peak temperatures and cooling rates in the heat-affected subzones while the physical measurement of FZ thermal history could not be successful due to severe temperature which the author found difficult to position the thermocouple in FZ. To maintain consistency, the dimensions of the workpiece, material properties, welding conditions, and boundary conditions used were the same as in the case of the previous results [178]. It indicates a good agreement between the calculated results and measured data. The correlation between the measured and simulated thermal cycles in these HAZ subzones demonstrated a good agreement, validating the accuracy of the simulation model.

12.4. Conclusion

RSW of long-time and 2-pulse welding was thermally modeled in the HAZ and FZ by FEM SYSWELD. Based on the outcomes the following conclusions can be drawn:

- The peak temperatures and cooling curves have logical values compared to the microstructural evaluation. The thermal cycles show significant differences between the long-time and 2-pulse welding, which causes different microstructures and HAZ dimensions.
- The gradient transitions in both simulation images show how heat dissipates through conduction. The sharper gradient in the 2-pulse weld suggests faster cooling and localized heat, while the long-time weld shows a more diffused heat distribution.
- The simulation measured the thermal cycle in the FZ, which is difficult to measure physically due to melting and the difficulty of positioning the measurement instrument in the faying surface.

13. MICROSTRUCTURAL ANALYSIS OF MS1400 RSW TECHNOLOGIES

The microstructural evolution of 1400 MPa MS steel welded using both long-time and 2-pulse RSW techniques were compared. The aims are to provide a detailed understanding of the microstructural changes, aided by thermal cycles analysis, and to compare one- and 2-pulse RSW technologies in MS steel. The results showed notable differences between the two welding technologies, and potential underlying mechanisms were discussed.

13.1. Materials and methods

Docol 1400M steel sheets with a thickness of 1 mm, produced by SSAB, were used as the base material. The chemical composition and mechanical properties of the steel are listed in *Table 7.1* and *Table 7.2*, respectively.

The employed welding parameters for the RSW technologies (2-pulse and long-time) are detailed in *Table 8.1*. These distinct parameters were chosen to investigate their influence on the microstructural characteristics and mechanical properties of the welded joints, particularly focusing on the trade-offs between FZ size and softening in the HAZ.

13.1.1. Thermodynamic modeling

JMatPro (v12.2) was utilized for constructing a continuous cooling transformation (CCT) diagram of the studied steel. The inputs for the simulation were the chemical composition of the steel, austenitization temperature, and grain size. An austenitization temperature of 860 °C and grain size of 30 μm were used for the calculation. CCT diagram predicts the microstructure and hardness of steel after various cooling rates.

13.1.2. Microstructural characterization

For more in-depth characterization, a field-emission scanning electron microscope (FESEM, Zeiss Sigma) equipped with an electron backscatter diffraction (EBSD) was used. The EBSD measurements were performed using an acceleration voltage of 15 kV, a working distance of 15 mm, and a scanning step size of 0.2 μm. The data were collected from an area size of 110 μm x 110 μm.

To further enhance the identification and quantification of the microstructural component, Image Quality (IQ) data derived from the EBSD results (EBSD-IQ) were analyzed based on the methodology by DeArdo [38][42][226][227]. It has been previously reported [66][69][184][228][229][230] that different phases and microstructural constituents exhibit distinct IQ values in EBSD measurements, largely influenced by the sharpness of the pattern, variations in surface topology, and dislocation networks within each phase. Therefore, quantitative analysis of microstructures can be performed by analysing the numerical values of EBSD-IQ. The method involved normalizing the IQ histograms and deconvolving them into multiple peaks, each representing different phases by assuming a normal distribution for each peak. Each peak was assigned to a specific microstructure component based on its position in the normalized IQ value axis. Eventually, the fraction of each microstructural constituent was calculated as the ratio of the area below each peak to the total normalized IQ area.

Ferrite and pearlite transformation occurs only after very slow cooling, whereas MS microstructure is a probable result after fast cooling. Calculated austenite start temperature (A_1) and austenite finish temperature (A_3) temperatures of 687.8 °C and 780.4 °C indicate that the microstructure is partly austenitic between these temperatures.

13.2.Results and discussion

13.2.1. Microstructural characterization by SEM

In the case of long-time welded joints, the microstructure were examined from various regions, including the FZ, and subzones within the HAZ. The micrographs are presented in *Figure 13.1*.

As observed, pointed by arrows, the martensite and tempered martensite are the main microstructural components within the FZ, UCHAZ, ICHAZ and SCHAZ. Several types of martensite were seen in the microstructure: untempered or fresh martensite (FM), fully tempered martensite (FTM), and partially tempered martensite (PTM). This is in line with the CCT diagram obtained by numerical simulation, which indicated martensite formation unless the cooling is very slow. However, in the current study, the cooling rates were extremely fast as shown in chapter 10.

In the FZ of long-time welding, the peak temperature is approximately 2300 °C but only a second later the temperature has cooled down to approximately 300 °C. This means that within a second the steel transforms from liquid phase to austenite and subsequently to martensite. In the UCHAZ region with the peak temperature exceeding 1000 °C the steel is fully austenitized and subsequently cooled very fast to 200 °C resulting again as MS microstructure. In ICHAZ the peak temperature is between A_1 and A_3 temperatures meaning that the steel is partly austenitized. As a result, some of the carbon diffusion from martensite forming carbon-rich and carbon-depleted regions. In SCHAZ the peak temperature is below A_1, so only a quick tempering may occur within the original MS microstructure.

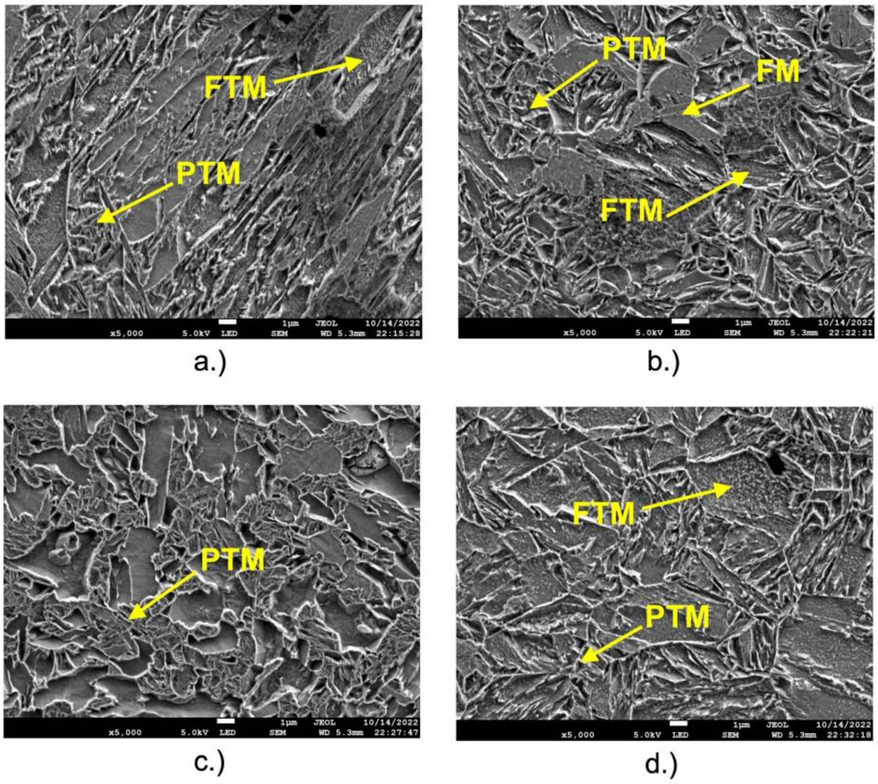

a.) b.)

c.) d.)

Figure 13.1. SEM images of long-time welded joint (MS1400): a.) FZ, b.) UCHAZ, c.) ICHAZ, d.) SCHAZ.

The microstructures after 2-pulse welding are presented in *Figure 13.2*. The microstructural features are similar to those of long-time welding. The difference to the long-time welding is the additional thermal cycle caused by the second pulse. Therefore, the FZ is divided into two distinctive regions with differences in the microstructure. The inner fusion zone (FZ2) is in the middle of the joint where the peak temperature exceeded 1600 °C. After fast cooling to about 200 °C, the temperature rose again to over 1000 °C due to the second pulse. This caused rapid austenitization and subsequent fast cooling all in less than one second. The recrystallization zone (Rex-zone) is at the boundary of the inner fusion zone (FZ2) where the first temperature peak was slightly above the liquidus temperature of the steel, and the second pulse peaked at about 900 °C. In UCHAZ, ICHAZ, and SCHAZ the second pulse remained below the A_1 resulting in only additional rapid tempering compared to the long-time welding. More detailed characterization will be discussed later using the EBSD-IQ results.

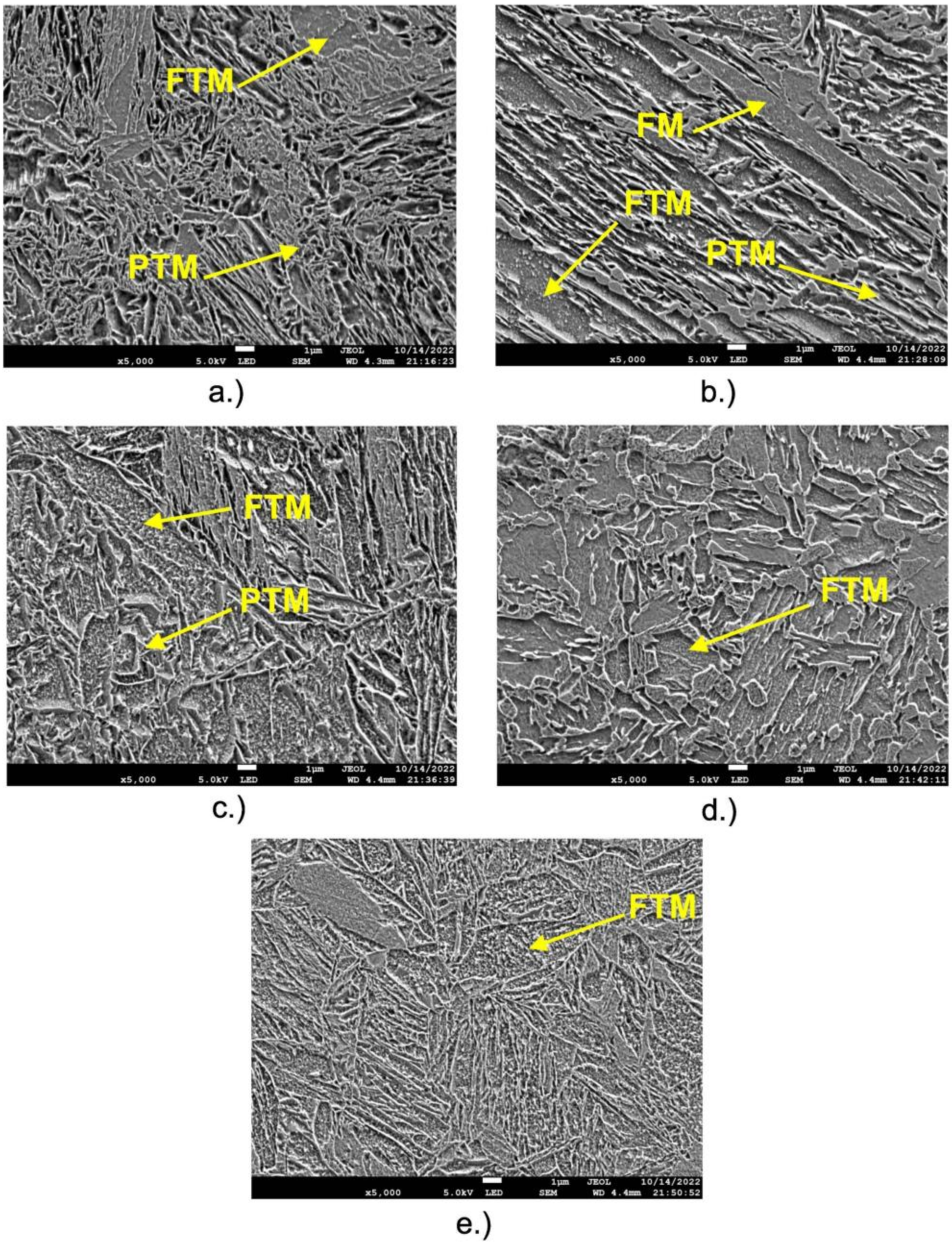

Figure 13.2. SEM images of 2-pulse welded joint (MS1400): a) FZ2, b) Rex-zone, c) UCHAZ, d.) ICHAZ, e) SCHAZ.

13.2.2. EBSD and IQ analyses

EBSD measurement and IQ analyses were performed in RSW joints made by long-time welding and 2-pulse welding. The analyses focused on the FZ (and FZ2 and Rex-zone in case of 2-pulse welding) and the subzones of HAZ like UCHAZ, ICHAZ, and SCHAZ. The percentages of phases were determined precisely. *Figure 13.3* and *Figure 13.4* shows the EBSD inverse pole figure (IPF) maps in the different zones.

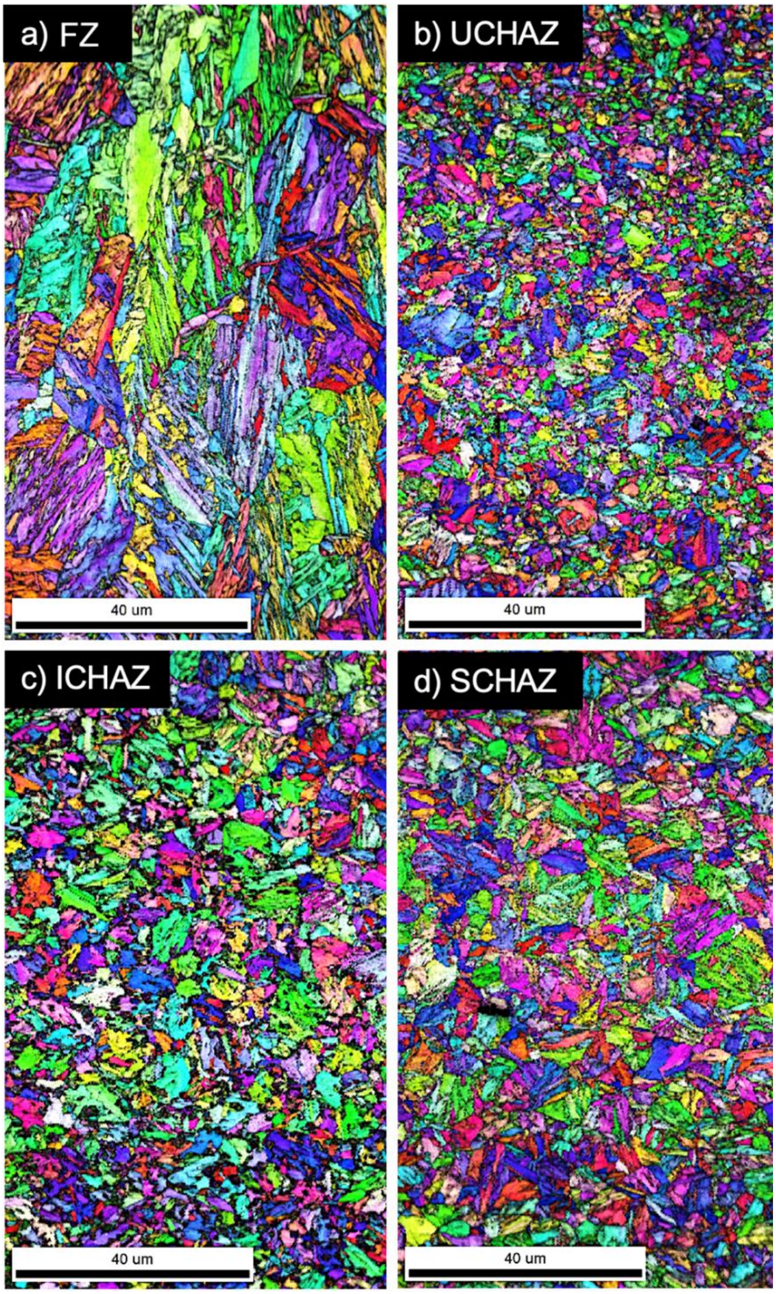

Figure 13.3. EBSD-IPF maps of long-time welded joint (MS1400): a) FZ, b) UCHAZ, c) ICHAZ, d) SCHAZ.

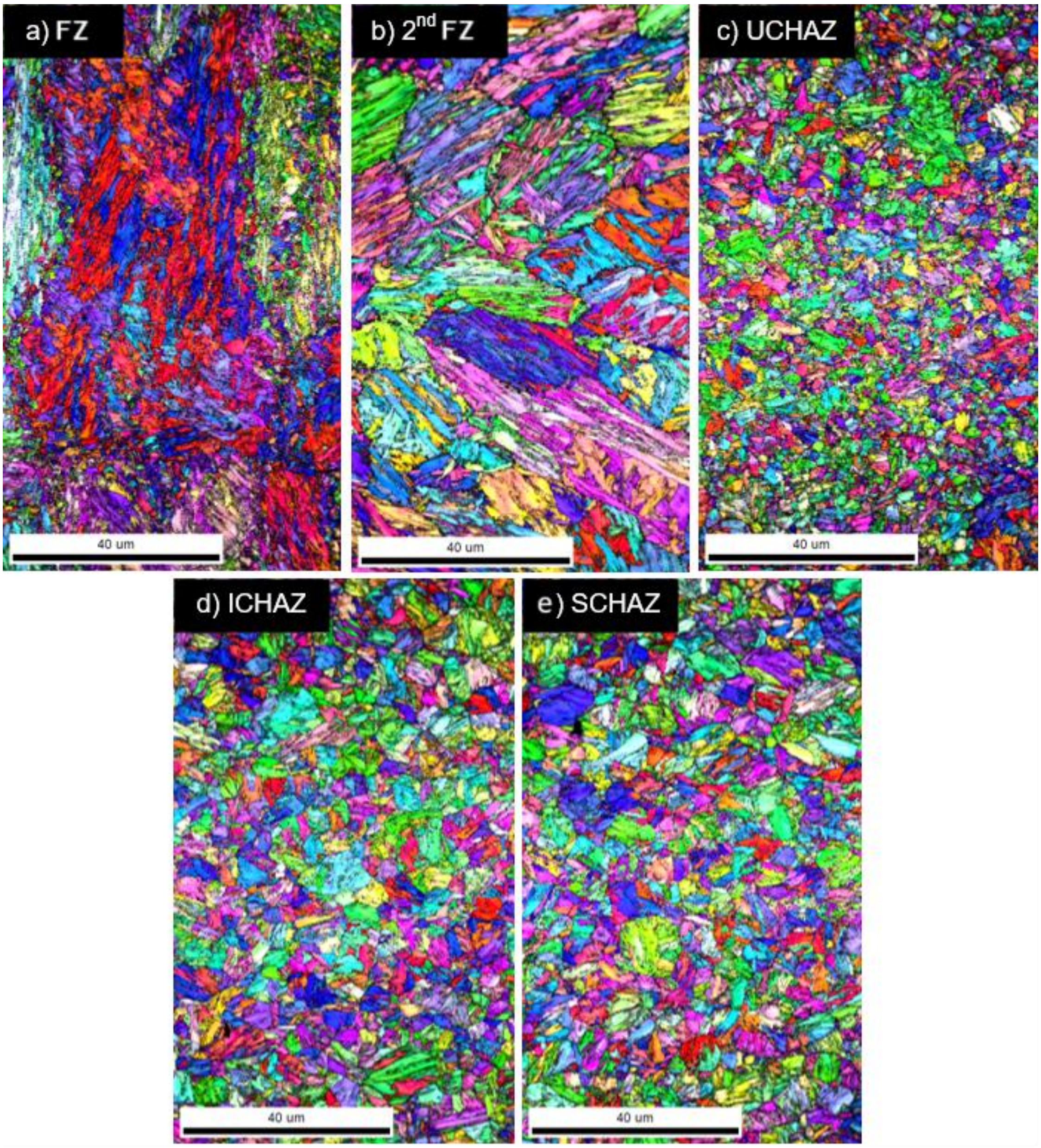

Figure 13.4. EBSD-IPF maps of 2-pulse welded joint (MS1400): a) FZ2, b) Rex-zone, c) UCHAZ, d) ICHAZ, e) SCHAZ.

Figure 13.5 helps to compare the fractions of microstructures in the subzones between long-time and 2-pulse welding. IQ maps obtained from the EBSD measurements can potentially reveal more structural features than secondary electron images since they represent the quality of acquired diffraction patterns. IQ values might be affected by microstructural characteristics, surface topology, local chemistry, or residual plastic deformations [46][47][231][232]. Consequently, compared to typical SEM images, IQ analysis can provide more information about the microstructural features. In general, accumulated strains in a crystal lattice are the primary parameter that alters IQ values throughout the lattice microstructure. These strains are predominantly caused by dislocations, and there is a direct relationship between the strain values and dislocation densities. Consequently, changes in IQ values can also represent fluctuations in dislocation densities. Hence, a microstructure component with a high dislocation density result in a low IQ-valued region in its EBSD measurements and vice versa [233].

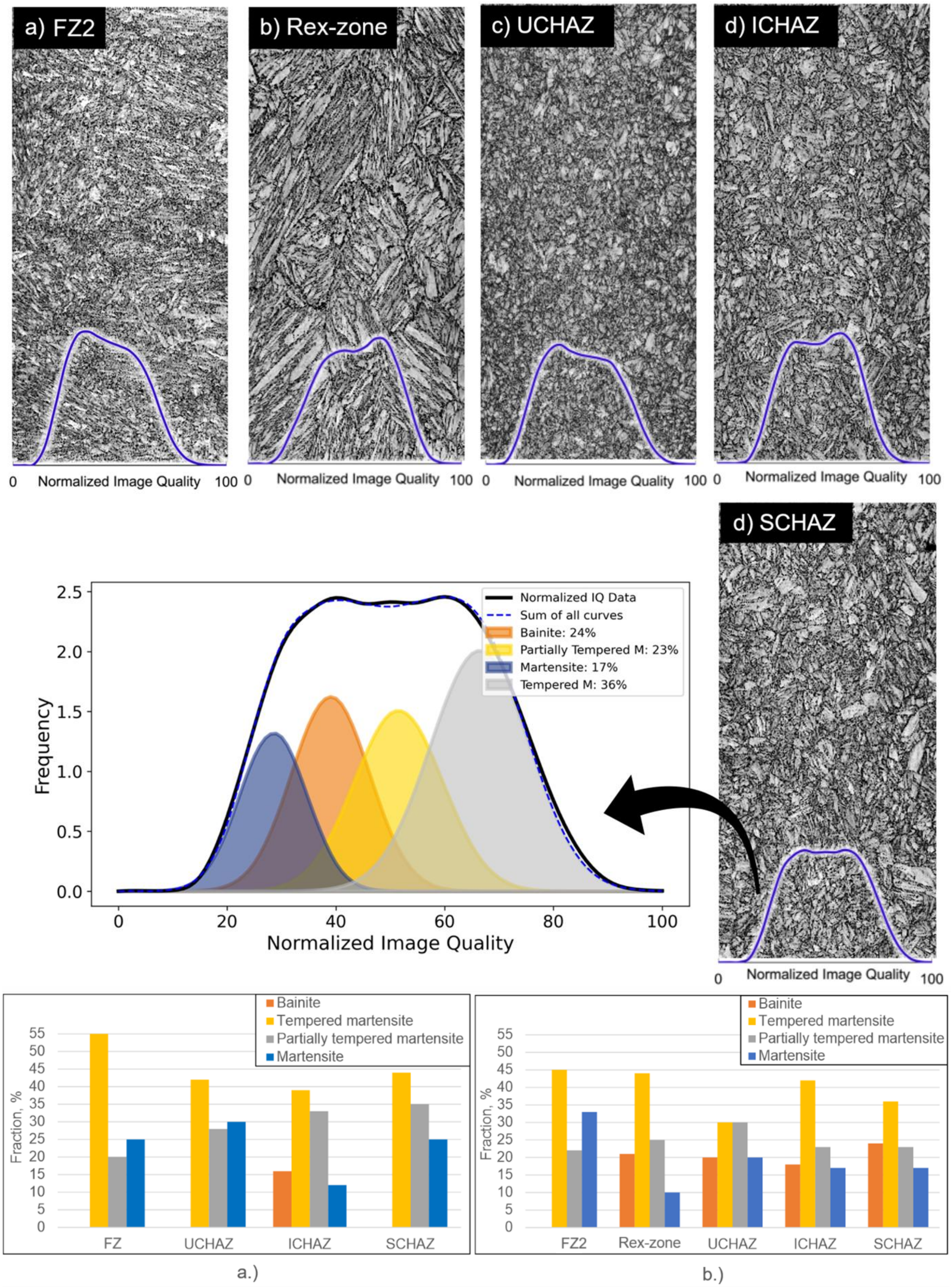

Figure 13.5. Fractions of different microstructural constituents in the subzones of RSW joints: a.) Long-time welding, b.) 2-pulse welding.

The effect of microstructural constituents can be more understandable with hardness measuring (Vickers) results, the appendix A2 show the hardness distribution along the spot welds cross-section.

In the FZ (center of the joint) in the case of long-time welding the percentage of martensite is much lower than in 2-pulse welded FZ2, but the fraction of tempered martensite is much higher. It obviously results from the longer welding time, which causes a longer thermal cycle providing more time for martensite tempering. The 2-pulse welded joint contains a Rex-zone part, where the fraction of martensite drastically decreased and bainite appeared. The UCHAZ of long-time welded joint contains more martensite than 2-pulse welded joint, but the fraction of tempered and partially tempered martensite is slightly bigger. Here the 2-pulse welded joint contains 20% of bainite. The hardness in this subzone shows a big difference in the case of long-time welding, it is 497 HV, while in the case of 2-pulse welding, it is 401 HV. Therefore, the bainite has also a softening effect next to the tempered martensite. The ICHAZ is the most softened zone in the long-time welded joint (322 HV), whereas 2-pulse welding causes here a slightly higher hardness value (341 HV). According to the analysed fractions of microstructures, it can be caused by the lowest fraction of martensite and the formation of bainite in the case of long-time welding. The 2-pulse welding technology caused a higher fraction of martensite, so the ICHAZ is less softened in this case. The SCHAZ shows a higher fraction of martensite in the case of long-time welding without bainite, whereas in the case of 2-pulse welding less martensite and the highest fraction of bainite was determined. There are no significant differences between hardness values in this subzone.

13.2.3. Grain size measurement

Grain sizes of the different subzones were measured too, because they affect the mechanical properties of the joints. *Figure 13.6* shows the results of average grain size measurement in the subzones. Effective (high-angle grain boundary) grain size is the average equivalent circular diameter (ECD) of the grains in micrometers. $D_{90\%}$ value describes the effective grain size at 90% in the cumulative size distribution.

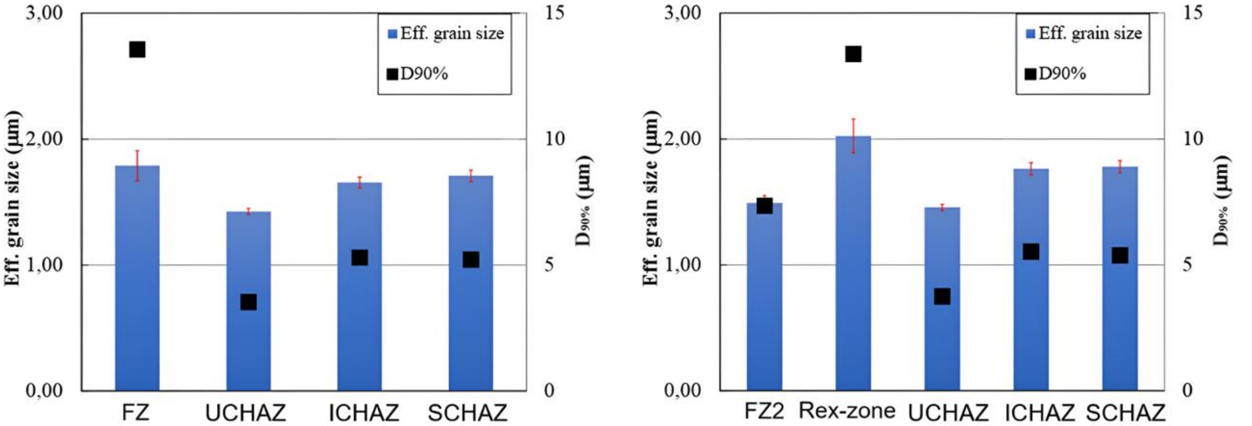

Figure 13.6. Grain sizes of the subzones: a.) long-time welding, b.) 2-pulse welding.

The term effective high-angle grain boundary (HAGB) grain size refers specifically to the average grain size calculated using only high-angle grain boundaries, defined as those with a misorientation angle greater than 15°, following the commonly accepted threshold [234].

The misorientation angle range examined was from 0° to 60°, but for the calculation of effective grain size, only boundaries above 15° were considered. The $D_{90\%}$ value represents the equivalent circular diameter (ECD) of grains at the 90% of the cumulative grain size distribution. It means that 90% of the measured grain areas (by frequency) are smaller than the $D_{90\%}$ value, effectively excluding the largest 10% to focus on the dominant grain population affecting mechanical behavior.

Regarding the average effective grain sizes the differences are relatively small between the different HAZ regions. In the long-time welded joint the coarsest average effective grain size is in the FZ (1.79±0.12 μm), while it is the smallest in the UCHAZ (1.43±0.02 μm). Average effective grain sizes in the ICHAZ and SCHAZ are between the aforementioned (1.66±0.04 μm and 1.71±0.05 μm, respectively). However, when comparing the coarsest grains in the regions i.e. the $D_{90\%}$ value, the differences are more pronounced. In the FZ the $D_{90\%}$ is 13.56 μm, whereas in the UCHAZ it is only 3.54 μm. In the ICHAZ and SCHAZ, the $D_{90\%}$ is slightly higher than in UCHAZ (5.30 μm and 5.22 μm, respectively). Interestingly, in the 2-pulse welded joint the Rex-zone has the most coarsened grains (average effective grain size 2.02±0.13 μm and $D_{90\%}$ 13.38 μm). In the FZ2, the average effective grain size is even smaller than in the ICHAZ and SCHAZ (1.49±0.06 μm vs. 1.76±0.05 μm and 1.78±0.05 μm, respectively). However, the $D_{90\%}$ is higher in the FZ2 than in the ICHAZ and SCHAZ (7.35 μm vs. 5.53 μm and 5.38 μm, respectively). Similarly, as in case of the long-time welding, the smallest grain size in the 2-pulse welded joint is in the UCHAZ (average effective grain size 1.46±0.02 μm and $D_{90\%}$ 3.75 μm). Generally, the grain sizes in the UCHAZ, ICHAZ and SCHAZ are comparable between the two welding methods. However, the difference is notable in the FZ, where two different regions were formed as a result of the 2-pulse welding. The inner fusion zone (FZ2) has a relatively small grain size, while in the outer FZ (Rex-zone), the grain size values resemble those of the FZ in long-time welding.

13.3. Conclusions

According to the results of the investigation, the following conclusions can be drawn:

- Fractions of each microstructural component were determined by EBSD and IQ analyses in the FZ and subzones of HAZ. The results show a correlation with thermal cycles and hardness values.
- In the case of long-time welding the FZ contains basically tempered/partially tempered martensite and untempered martensite, which can cause high hardness values. In the UCHAZ the types of microstructural components are the same, and there is no significant difference in their fractions. This observation is by the hardness distribution: the hardness of these zones is more or less the same. In the ICHAZ the 16% fraction of bainite appears, which causes hardness drop. The martensite content is the smallest in this subzone, while tempered and partially tempered martensite is present in high volume. In the SCHAZ the volume of martensite has increased again, whereas the volume of tempered and partially tempered martensite did not differ from other subzones. It can be concluded that the presence of bainite contributes to the biggest hardness drop in long-time welding technology.
- In the case of 2-pulse technology the FZ is separated into two zones and the microstructure in the inner fusion zone (FZ2) consists of martensite and tempered/partially tempered martensite, and no other microstructural component was found there. In the outer ring-shaped part (Rex-zone) 21% of bainite appeared next to the martensite causing softening according to the hardness test. In all subzones of HAZ, the bainite formed during welding in relatively the same volume (between 18 – 24 %).
- The effect of bainite is significant in the case of 2-pulse welding and it causes wider softened part than long-time welding. The ICHAZ is the weakest part of the long-time welded joint.
- In the case of 2-pulse welding it results slightly higher hardness, probably because of the higher fraction of martensite.

- In the case of long-time welding the largest grains are in the FZ, while the UCHAZ is fine-grained, and the ICHAZ and the SCHAZ have slightly coarser grain sizes.
- In the case of 2-pulse technology in the HAZ the tendency of grain sizes is approximately the same, but in the FZ2 the grain size in the core is much smaller than in the outer ring-shaped part (Rex-zone). Generally, the 2-pulse welding causes a slightly larger grain size than the long-time welding.

14. THESES – NEW SCIENTIFIC RESULTS

T1. After investigating the effect of the geometrical deviation on tensile-shear (T-S) and cross-tension (C-T) tests of resistance spot welded under consistent conditions, the following was found (4) (8):

- a. The results revealed that geometrical deviations have no significant influence on the strength, displacement, and failure mode for DP600, DP800, DP1000, and MS1200.
- b. In contrast, MS1400 samples displayed reduced performance, with 2 mm and 8° degrees deviations showing a noticeable drop in the strength and displacement, while the failure mode showed more response to the geometrical deviation compared to the standard sample, proving that the higher strength of steel is more likely to be affected by the geometrical deviation and suggesting the importance of precise geometry of samples.

T2. The effects of welding parameters and base metal strength on the tensile-shear (T-S) test performance of resistance spot welding (RSW) were investigated and found (2) (3) (9) (17):

- a. The comparative analysis of long-time, 2-pulse, and short-time RSW technologies on martensitic steels (MS1200 and MS1400) revealed that, despite all methods induced relatively similar softening values, the long-time welding emerged as the most effective welding technology, producing superior fusion zones (FZ) with the largest diameters, optimal strength, and favorable pull-out failure modes compared to 2-pulse and short time RSW. The findings suggest that welding parameters technologies play critical role in determining RSW T-S strength.
- b. The comparative assessment of dual-phase (DP) and martensitic (MS) steels welded using the long-time resistance spot welding (RSW) process revealed that, while martensitic steels (MS1200 and MS1400) exhibited pronounced softening in the heat-affected zone (HAZ), they achieved the highest T-S strength and the lowest displacement. In contrast, dual-phase steels (DP600, DP800, and DP1000) demonstrated greater displacement before failure and lower T-S strength, with minimal softening observed only in DP1000. The findings suggest that base metal strength play critical role in determining RSW T-S strength.

T3. The high cycle fatigue (HCF) demonstrated consistent heat-affected zone (HAZ) failure modes within the two groups, dual-phase (DP) and martensitic (MS) steels. The steel grade significantly influences HCF behavior, as different grades exhibit varying hardness levels, which directly affect their fatigue performance. The HCF performance in case of mean-2 standard deviation (mean-2SD) follows a sequential trend supported by hardness measurements in the tongue (crack initiation zone). Specifically, lower hardness in this region corresponds to a lower endurance limit force (MS1200 and MS1400), while higher hardness corresponds to a higher endurance limit force (DP600, DP800, and DP1000) leads to improved fatigue resistance (5) (16).

T4. Based on the experimental results, by the developed impact-bending test method on dual-phase (DP) steels the different resistance spot welding (RSW) technologies and base materials can be effectively compared. For acceptable results, the plug diameter should be under 5.1 mm, as larger diameters may cause base material failure (7).

a. The welding technique and steel grade play crucial roles in determining the impact energy of resistance spot welds. Long-time welding consistently outperforms other methods (2-pulse and short-time), producing the highest impact energy and force across all tested steel grades. Additionally, while DP600 and DP1000 exhibit similar impact energy levels, DP1000's superior impact force suggests greater overall impact safety.

b. The comparison of the impact energy and impact force between DP600 and DP800, reveals notable differences influenced by the welding technology used. In the long-time welding, the impact energy of DP600 is approximately 5% higher than DP800's. In contrast, for the 2-pulse, DP600 records a significant reduction in energy absorption compared to DP800 and the short-time welding showed a similar trend for 2-pulse RSW. These variations highlight the influence of material properties and welding parameter on joint performance in impact loading resistance.

T5. A physical heat cycle measuring method was further developed to physically measure the heat cycle in depth within the heat-affected subzones of resistance spot welding (RSW). The method accurately assesses the heat cycle facilitating the correlation between thermal cycles and microstructural transformations thuse optimizing welding parameters. The recorded heat cycle for both long-time and 2-pulse RSW revealed significant differences in thermal profiles, including temperature gradients, cooling rates, and peak temperatures across the heat-affected subzones of both technologies. In the upper critical heat-affected zone (UCHAZ), the $t_{8/5}$ (time to cool from 800°C to 500°C) in the 2-pulse RSW process was observed to be five times faster than that of long-time welding. The measured heat cycle closely correlates with finite element modeling (FEM), providing a reliable validation of the simulation's accuracy in predicting thermal behavior during welding (6) (10) (14).

T6. A comparative microstructural analysis of MS1400 steel long-time and 2-pulse welding revealed notable differences in microstructural evolution (15).

a. The microstructure of weld zones varies significantly between long-time and 2-pulse welding. In the long-time, bainite appeared only in the inter-critical heat subzone (ICHAZ). However, in the 2-pulse welding, bainite formed in all heat-affected subzones and the recrystallized zone (Rex-zone), except the inner fusion zone. Notably, bainite fraction reduced the overall martensite fraction compared to zones without bainite, influencing the mechanical properties between long-time and 2-pulse spot joint welding

b. The effect of welding parameters on 90% of the cumulative grain size distribution ($D_{90\%}$) reveals a tendency for different heat-affected subzones to exhibit significant similarity in effective grain size between long-time and 2-pulse welding technologies. In long-time welding, the fusion zone (FZ) has the largest grain size, while in 2-pulse welding, the Rex-zone experiences the most coarsening. Notably, 2-pulse welding results in a distinct grain size variation within the FZ, forming an outer (Rex-zone) and inner fusion zone (FZ2) zones with different microstructural characteristics.

15. SUMMARY

RSW is a key joining method in the automotive and aerospace industries, valued for its efficiency, speed, and ability to create strong joints in sheet metal structures. The rise of AHSS is crucial for reducing vehicle weight while maintaining crashworthiness, particularly in electric vehicles (EVs), which are significantly heavier due to their batteries. However, welding AHSS poses challenges due to its high hardness and heat sensitivity, necessitating the development of optimized RSW techniques. The performance of spot welds depends on stress conditions, which vary across vehicle and aircraft structures. Engineers must carefully select AHSS grades and tailor welding parameters to balance strength, ductility, impact, and fatigue resistance. This research provides valuable insights into the RSW of dual-phase and martensitic steels, with applications extending beyond automotive and aerospace to industries, where AHSS is widely used.

Optimizing welding parameters is crucial for enhancing joint strength, durability, and defect prevention in RSW focuses on welding current, time, force, and pulsation technology to improve weld quality, particularly in AHSS. By controlling the RSW geometry, failure mode and HAZ softening, these optimizations ensure superior mechanical performance.

Optimizing sample quality to enhance the accuracy of predictive models, improve welding techniques, and refine spot weld designs for AHSS in automotive applications. The research highlights the importance of sample geometry in determining mechanical properties and failure behavior. By precisely controlling these factors, engineers can improve weld performance, ensuring durability and consistency in both research and industrial-scale production. The geometrical deviations in MS1400 steel significantly impact C-T and T-S test results, emphasizing the importance of precise sample preparation for higher-strength steel RSW.

Simulating heat cycles and validating them through physical measurements play a crucial role in optimizing resistance spot welding. FEM enables engineers to develop predictive models that refine welding parameters, minimize experimental costs, and enhance efficiency in industrial applications. By analyzing thermal history, engineers can optimize cooling rates, particularly in requiring precise thermal control.

The research underscores the difference between of long-time weld and 2-pulse RSW in refining weld microstructures in MS1400 steel, enhancing mechanical properties, and ensuring long-term structural reliability. Advanced microstructural characterization technologies, reveal key phase transformations and grain refinement processes in the WN and HAZ, emphasizing the role of martensite and ferrite distribution in determining weld strength. This knowledge aids in the development of next-generation AHSS with improved weldability and fatigue resistance, supporting safer and more durable engineering designs.

The fatigue performance of HCF in RSW for AHSS is influenced by a combination of factors, primarily the steel grade and weld geometry so it essential to carefully consider both material selection and welding design in engineering automotive applications.

To understand the behavior of RSW in DP steels during collisions in automotive engineering, instrumented impact testing serves as a sophisticated method to evaluate dynamic fracture behavior, capturing real-time data on how materials respond to sudden impact forces.

Figure 15.1 illustrates the complex relationship between welding parameters and the microstructural and mechanical properties of AHSS. The figure synthesizes findings from both literature and the experimental research to establish clear correlations between welding conditions and mechanical properties. These parameters significantly impact the microstructure of both the weld zone and heat-affected zone, influencing properties such as tensile strength, fatigue resistance, impact toughness, and hardness.

The base metal's is another essential factor that impacts the final properties of the weld. By integrating welding parameters, material properties, and geometrical factors, the figure provides a comprehensive understanding of how to achieve the desired performance in AHSS spot welds.

The figure also highlights the critical role of weld geometry, particularly the weld nugget size and notch angle, in determining the strength and durability of RSW. All RSW geometries influence the failure mode and contribute to an increase in mechanical testing strengths, except expulsion.

Despite softening occurring from DP1000 to MS1400 and hardening from DP600 to MS1400, as shown in the figure, the mechanical testing strengths, such as cross-tension strength (CTS) and tensile-shear strength (TSS), further reveals the behavior of AHSS spot welds in terms of loading direction and WN geometry. The tensile shear strength (TSS) of spot-welded joints demonstrates a positive correlation with base steel strength, while TSS increases with higher steel tensile strength a trend supported by empirical correlations between hardness and tensile properties of AHSS. For components experiencing predominantly in-plane tensile loading, such as T-S joint configurations, UHSS like MS1200 and MS1400 are optimal due to their enhanced load-bearing capacity. Conversely, cross-tension specimen (CTS) applications involving perpendicular tensile forces benefit from lower-strength steels, as their greater ductility accommodates complex stress states and mitigates brittle fracture risks. Displacement characteristics further influence joint design, with T-S configurations typically exhibiting limited deformation capacity prior to failure compared to C-T joints, a critical consideration for energy absorption requirements in dynamic loading scenarios. This strength-ductility contrast underscores the necessity for application-specific steel selection in automotive body-in-white assemblies, where joint performance must balance structural integrity with crashworthiness demands.

In long-time welding DP1000 steel exhibits exceptional high-cycle fatigue (HCF) performance due to its well-balanced combination of strength and ductility, making it particularly suitable for automotive and aerospace components subjected to prolonged cyclic loading. In contrast, martensitic steels (MS1200 and MS1400), despite their higher strength, show comparatively lower HCF performance. Since the most critical factors influencing HCF behavior, fusion zone (FZ) size and notch angle at weld edges were consistent across all grades, the key differentiating factor was the hardness of the crack initiation zone. The observed trend aligned with HCF strength, where lower hardness at crack initiation zone corresponded to lower fatigue performance.

By applying three different welding parameters, samples welded with a longer duration and higher current exhibited superior impact resistance compared to those welded using 2-pulse or short-time parameters. This improvement is attributed to the larger fusion zone (FZ) formed under higher welding current and extended duration, making these welds particularly suitable for components subjected to sudden loads, such as crash-sensitive areas. Among DP steels, DP1000 demonstrated slightly higher impact force while maintaining the same impact energy as DP600 in long-time welding conditions, highlighting the dominant role of FZ size in determining the impact resistance of spot welds in DP steels.

The complexity in evaluating RSW of AHSS necessitates rigorous pre-design analysis of weld locations to account for variable mechanical demands. AHSS welding parameters and multi-pulse welding techniques, must be applied for each application due to the material’s hardenability, and susceptibility to localized stress concentrations. These factors, combined with site-specific loading conditions (static, dynamic, or combined stresses), complicate joint design. Achieving reliable and consistant RSW samples, is the demand of the mechanical and microstructural standardized testing to evaluate failure modes, weld geometry, and base metal interactions. Additionally, HCM and simulation can refine parameters to balance production efficiency with joint integrity.

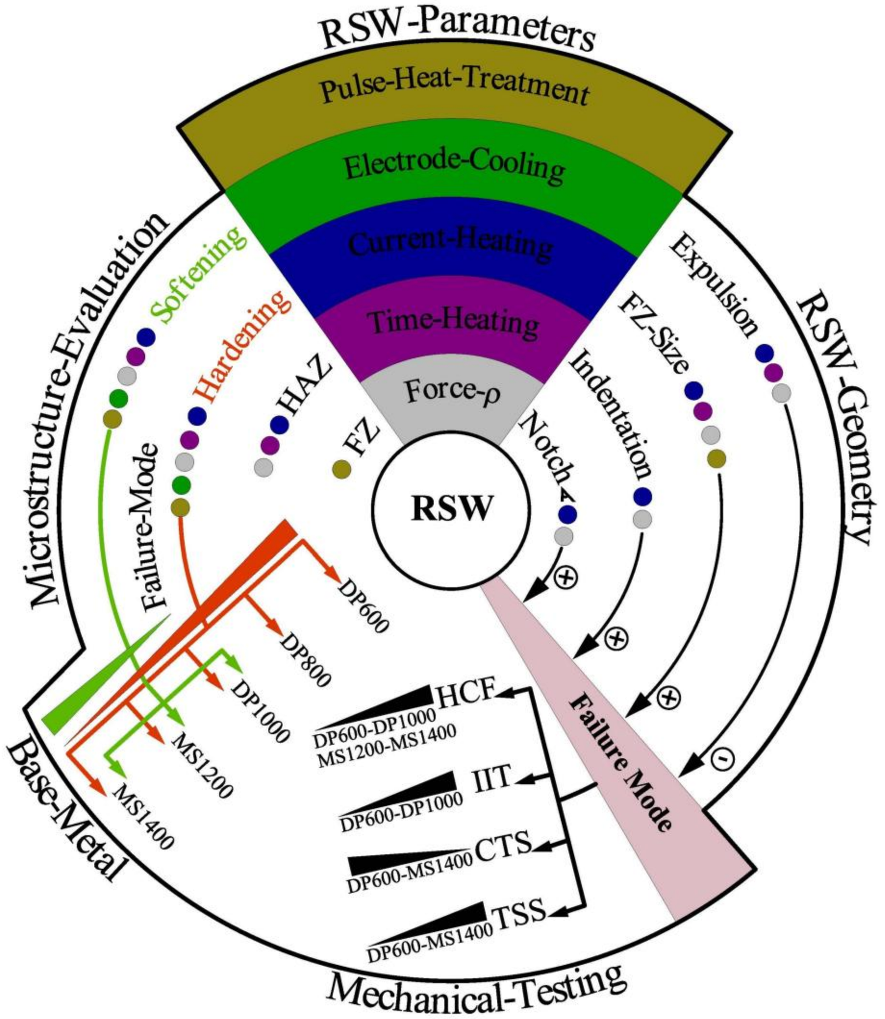

Legend

●	Pulsation
●	Electrode geometry
●	Welding current
●	Welding time
●	Welding force
⊕	Increasing mechanical testing strength
⊖	Decreasing mechanical testing strength
◢	Mechanical testing strength increases
◣	Mechanical testing strength decreases
◢	RSW softening increases (DP1000-MS1400)
◢	RSW hardening increases (DP600-MS1400)

Figure 15.1. The complex evaluation of RSW parameters and RSW outcomes.

ACKNOWLEDGEMENTS

With profound sorrow and enduring gratitude, I dedicate this work to the memory of my beloved mother. Her unwavering love, strength, and belief in me guided every step of my journey. Even though she passed away before witnessing the completion of this dissertation, her presence continues to shape my life and inspire my perseverance. Her support was not limited to the moments she lived it extended far beyond; through every challenge I faced and every achievement I earned. I owe this milestone to the foundation she built with her sacrifices and unconditional care. I am deeply grateful to my sister, whose boundless support and emotional strength have given me the courage to continue even in the most difficult times. She has been my anchor, my source of energy, and a constant reminder that I was never alone in this journey. To my father, who has always stood with quiet pride behind each of my academic achievements thank you for your faith in me. Your encouragement and confidence in my abilities have been a powerful force driving me forward.

I would like to express my sincere appreciation to my supervisors for their constant support and guidance throughout my doctoral journey. I am especially thankful to Dr. Ákos Meilinger, who stood by me step by step over the course of four years. His continuous encouragement, patience, and mentorship were instrumental not only in shaping this research but also in helping me grow as an independent researcher. My deep gratitude also goes to Prof. Dr. Marcell Gáspár, whose insightful guidance and steady support were invaluable in every phase of this work. His constructive feedback and belief in my potential made a significant difference in both the academic and personal aspects of this journey.

I am also truly grateful to my colleagues at the university, whose presence made this journey not only productive but also meaningful and enjoyable. Their camaraderie, shared knowledge, and everyday support turned challenges into opportunities and transformed the demanding moments of doctoral life into lasting memories. I am especially thankful to Dr. Lukács Zsolt and Prof. Dr. Lukács János for their efforts, support, and invaluable cooperation throughout this endeavor.

A very special thanks goes to my dear friend Gábor Molnár, whose big heart, constant motivation, and brotherly support meant more to me than words can express. He stood by me not only as a friend but as family, offering encouragement during the toughest times and always reminding me of my strength and purpose. His belief in me played a key role in helping me push forward and complete this long journey.

Finally, I would like to extend my sincere gratitude to the University of Miskolc and the Faculty of Mechanical Engineering and Informatics for providing me with the academic foundation, research facilities, and a supportive environment essential for completing this PhD.

I am also thankful to Hungary, a country that welcomed me with warmth and safety, and gave me the opportunity to pursue my academic dreams in a peaceful and inspiring setting. This journey would not have been possible without the stability, kindness, and opportunities I found here.

REFERENCES

[1] N. Fonstein, “Evolution of Advanced High Strength Steels (AHSS) for Automotive Industry 1.”

[2] M. Tisza, “Development of Advanced High Strength Automotive Steels,” *Acta Materialia Transylvanica*, vol. 4, no. 1, pp. 9–17, 2021, doi: 10.33923/amt-2021-01-02.

[3] B. Palotás, I. Zemankó, and R. Rózsahegyi, “Ferrites-martenzites DP- acélok ellenállás ponthegesztés,” Dunaújváros: Kohászat 2014 Konferencia Kiadvány, 2014, pp. 40–43.

[4] S. S. Nayak, Y. Zhou, V. H. Baltazar Hernandez, and E. Biro, “Resistance spot welding of dual-phase steels: Heat affected zone softening and tensile properties,” *ASM Proceedings of the International Conference: Trends in Welding Research*, pp. 641–649, 2013.

[5] L. Kaščák, E. Spišák, and I. Gajdoš, “Influence of welding parameters on the quality of resistance spot welded joints of DP600 steels,” in *Key Engineering Materials*, Trans Tech Publications Ltd, 2015, pp. 143–146. doi: 10.4028/www.scientific.net/KEM.635.143.

[6] A. K. Perka, M. John, U. B. Kuruveri, and P. L. Menezes, “Advanced High-Strength Steels for Automotive Applications: Arc and Laser Welding Process, Properties, and Challenges,” Jun. 01, 2022, *MDPI*. doi: 10.3390/met12061051.

[7] X. Hu and Z. Feng, “Advanced High-Strength Steel-Basics and Applications in the Automotive Industry,” 2021. [Online]. Available: www.osti.gov

[8] “https://www.media.volvocars.com/global/en-gb/media/photos/148215/volvo-xc90-body-structure.”

[9] S. A. Jadhav and M. A. Venkatesh, “A Review Paper On Optimization Of Process Parameter Of Spot Welding By Multi Objective Taguchi,” *International Research Journal of Engineering and Technology*, 2016, [Online]. Available: www.irjet.net

[10] H. L. Jaber, M. Pouranvari, R. K. Salim, F. A. Hashim, and S. P. H. Marashi, “Peak load and energy absorption of DP600 advanced steel resistance spot welds,” *Ironmaking and Steelmaking*, vol. 44, no. 9, pp. 699–706, Oct. 2017, doi: 10.1080/03019233.2016.1229880.

[11] K. Aydin, M. Hidiroglu, and N. Kahraman, “Characterization of the Welding Zone of Automotive Sheets of Different Thickness (DP600 and DP800) Joined by Resistance Spot Welding,” *Transactions of the Indian Institute of Metals*, vol. 75, no. 5, pp. 1279–1291, 2022, doi: 10.1007/s12666-021-02482-5.

[12] A. Karafakioglu, F. Bedir, S. Yalçinkaya, S. İnan Öz, and A. Uludağ, “A Review on the Effects of Resistance Spot Welding Process Parameters on Welding Strength Used in Automotive Industry,” *International Refereed Journal of Engineering and Sciences*, vol. 0, no. 18, pp. 0–0, 2022, doi: 10.17366/uhmfd.2022.18.8.

[13] C. Rajarajan, P. Sivaraj, and V. Balasubramanian, “Microstructural analysis of weld nugget properties on resistance spot-welded advance high strength dual phase (α+α /) steel joints,” *Mater Res Express*, vol. 7, no. 1, 2020, doi: 10.1088/2053-1591/ab654d.

[14] E. Javaheri, J. Lubritz, B. Graf, and M. Rethmeier, “Mechanical properties characterization of welded automotive steels,” *Metals (Basel)*, vol. 10, no. 1, pp. 1–19, 2020, doi: 10.3390/met10010001.

[15] H. Lebbal, L. Boukhris, H. Berrekia, and A. Ziadi, “Thermomechanical analysis of the resistance spot-welding process,” *Computational Thermal Sciences*, vol. 10, no. 5, pp. 449–455, 2018, doi: 10.1615/ComputThermalScien.2018020490.

[16] N. T. Williams, *Resistance spot welding* , vol. ASM handbook 6. 1993.

[17] R. Sreenivasulu, “Joining of Dissimilar alloy Sheets (Al 6063&AISI 304) during Resistance Spot Welding Process: A Feasibility Study for Automotive industry,” *Independent Journal of Management & Production*, vol. 5, no. 4, Dec. 2014, doi: 10.14807/ijmp.v5i4.231.

[18] E. Wintjes *et al.*, “Effect of Multiple Pulse Resistance Spot Welding Schedules on Liquid Metal Embrittlement Severity,” *J Manuf Sci Eng*, vol. 141, no. 10, Oct. 2019, doi: 10.1115/1.4044099.

[19] H. Zhang and J. Senkara, *Resistance Welding Fundamentals and Applications*. CRC Press, 2006.

[20] M. Stadler, “Chair of Design of Steels Resistance Spot Welding of Third Generation Advanced High Strength Steels,” 2021.

[21] M. Hamedi and M. Atashparva, “A review of electrical contact resistance modeling in resistance spot welding,” *Welding in the World*, vol. 61, no. 2, pp. 269–290, Mar. 2017, doi: 10.1007/s40194-016-0419-4.

[22] Y. G. Kim, I. J. Kim, J. S. Kim, Y. Il Chung, and D. Y. Choi, “Evaluation of surface crack in resistance spot welds of zn-coated steel,” *Mater Trans*, vol. 55, no. 1, pp. 171–175, 2014, doi: 10.2320/matertrans.M2013244.

[23] M. Pouranvari and S. P. H. Marashi, “Failure mode transition in AHSS resistance spot welds. Part I. Controlling factors,” *Materials Science and Engineering: A*, vol. 528, no. 29–30, pp. 8337–8343, 2011, doi: 10.1016/j.msea.2011.08.017.

[24] C. D. Horvath, *Advanced steels for lightweight automotive structures*. LTD, 2021. doi: 10.1016/b978-0-12-818712-8.00002-1.

[25] J. Liang, H. Zhang, X. Qiu, and Y. Shi, “Characteristics of the resistance spot welding joints in dissimilar thickness dual-phase steels,” *ISIJ International*, vol. 55, no. 9, pp. 2002–2007, 2015, doi: 10.2355/isijinternational.ISIJINT-2015-151.

[26] G. Avramovic-Cingara, Y. Ososkov, M. K. Jain, and D. S. Wilkinson, “Effect of martensite distribution on damage behaviour in DP600 dual phase steels,” *Materials Science and Engineering: A*, vol. 516, no. 1–2, pp. 7–16, Aug. 2009, doi: 10.1016/j.msea.2009.03.055.

[27] I. A. Soomro, S. R. Pedapati, M. Awang, and M. A. Alam, “Effects of double pulse welding on microstructure, texture, and fatigue behavior of DP590 steel resistance spot weld,” *International Journal of Advanced Manufacturing Technology*, vol. 125, no. 3–4, pp. 1271–1287, 2023, doi: 10.1007/s00170-022-10704-3.

[28] A. Chabok, E. van der Aa, J. T. M. De Hosson, and Y. T. Pei, “Mechanical behavior and failure mechanism of resistance spot welded DP1000 dual phase steel,” *Mater Des*, vol. 124, pp. 171–182, 2017, doi: 10.1016/j.matdes.2017.03.070.

[29] V. H. Baltazar Hernandez, S. S. Nayak, and Y. Zhou, “Tempering of martensite in dual-phase steels and its effects on softening behavior,” *Metall Mater Trans A Phys Metall Mater Sci*, vol. 42, no. 10, pp. 3115–3129, Oct. 2011, doi: 10.1007/s11661-011-0739-3.

[30] World auto steel, “AHSS Application Guideline, https://ahssinsights.org/metallurgy/steel-grades/ahss/dual-phase/”.

[31] G. Béres and Z. Weltsch, “Estimation of strength properties from microhardness results in dual phase steels with different martensite volume fraction,” *Periodica Polytechnica Transportation Engineering*, vol. 47, no. 3, pp. 206–212, 2019, doi: 10.3311/PPtr.12113.

[32] M. S. Rashid, “DUAL PHASE STEELS +8665,” 1981. doi: 10.1146/annurev.ms.11.080181.001333.

[33] G. R. Speich, V. A. Demarest, and R. L. Miller, “Formation of Austenite During Intercritical Annealing of Dual-Phase Steels.” doi: https://doi.org/10.1007/BF02643686.

[34] M. Tisza, “Development of Lightweight Steels for Automotive Applications.” [Online]. Available: www.intechopen.com

[35] Y. Mazaheri, A. Kermanpur, and A. Najafizadeh, “Strengthening mechanisms of ultrafine grained dual phase steels developed by new thermomechanical processing,” *ISIJ International*, vol. 55, no. 1, pp. 218–226, 2015, doi: 10.2355/isijinternational.55.218.

[36] M. Tisza, “Three Generations of Advanced High Strength Steels in the Automotive Industry,” in *Lecture Notes in Mechanical Engineering*, Springer Science and Business Media Deutschland GmbH, 2021, pp. 81–94. doi: 10.1007/978-981-15-9529-5_7.

[37] J. Ayres, D. Penney, P. Evans, and R. Underhill, “Effect of intercritical annealing on the mechanical properties of dual-phase steel,” *Ironmaking and Steelmaking*, vol. 49, no. 8, pp. 821–827, 2022, doi: 10.1080/03019233.2022.2062163.

[38] M. Kekik, F. Özen, E. İlhan, and S. Aslanlar, “Microstructural Evaluation and Influence of Welding Parameters on Electrode Plunge Depth in Resistance Spot Welded Dissimilar DP800HF/1200M Steel Joints,” *Academic Platform Journal of Engineering and Science*, vol. 9, no. 2, pp. 284–291, May 2021, doi: 10.21541/apjes.859623.

[39] R. Kuziak, R. Kawalla, and S. Waengler, “Advanced high strength steels for automotive industry: A review,” 2008, *Oficyna Wydawnicza Politechniki Wroclawskiej*. doi: 10.1016/s1644-9665(12)60197-6.

[40] H. Mohrbacher, “Martensitic Automotive Steel Sheet - Fundamentals and Metallurgical Optimization Strategies,” *Adv Mat Res*, vol. 1063, pp. 130–142, Dec. 2014, doi: 10.4028/www.scientific.net/amr.1063.130.

[41] P. Du Bois *et al.*, *Vehicle Crashworthiness and Occupant Protection*. Southfield, Michigan: Automotive Applications Automotive Applications Committee American Iron and Steel Institute, 2004.

[42] H. Ghadbeigi, C. Pinna, and S. Celotto, “Failure mechanisms in DP600 steel: Initiation, evolution and fracture,” *Materials Science and Engineering: A*, vol. 588, pp. 420–431, Dec. 2013, doi: 10.1016/j.msea.2013.09.048.

[43] N. Nadimi, M. Pouranvari, R. Ansari, and M. Pouranvari, “Understanding fusion zone hardness in resistance spot welds for advanced high strength steels: Strengthening mechanisms and data-driven modeling,” *Journal of Materials Research and Technology*, vol. 26, pp. 5549–5565, Sep. 2023, doi: 10.1016/j.jmrt.2023.08.251.

[44] G. E. Totten, Ed., *Steel Heat Treatment*. CRC Press, 2006. doi: 10.1201/NOF0849384523.

[45] G. Krauss, “Martensite in steel: strength and structure,” 1999. [Online]. Available: www.elsevier.com/locate/msea

[46] H. Bhadeshia and R. Honeycombe, *Microstructure and Properties*. Elsevier, 2017. doi: 10.1016/B978-0-7506-8084-4.X5000-6.

[47] M. Kimchi and D. H. Phillips, *Resistance Spot Welding*. Cham: Springer International Publishing, 2018. doi: 10.1007/978-3-031-79576-3.

[48] Y. Ma *et al.*, “Fracture modeling of resistance spot welded ultra-high-strength steel considering the effect of liquid metal embrittlement crack,” *Mater Des*, vol. 210, Nov. 2021, doi: 10.1016/j.matdes.2021.110075.

[49] S. Mathi, P. Bamberg, A. Schiebahn, and U. Reisgen, “Estimation of the Incidence of Liquid Metal Embrittlement Crack in 3rd Generation Advanced High Strength Steel During Resistance Spot Welding using 2D and 3D Weld Lobe Curve.” [Online]. Available: www.ijert.org

[50] P. Kah, M. Pirinen, R. Suoranta, and J. Martikainen, “Welding of ultra high strength steels,” in *Advanced Materials Research*, 2014, pp. 357–365. doi: 10.4028/www.scientific.net/AMR.849.357.

[51] Y. Li, H. Tang, and R. Lai, “Microstructure and mechanical performance of resistance spot welded martensitic advanced high strength steel,” *Processes*, vol. 9, no. 6, Jun. 2021, doi: 10.3390/pr9061021.

[52] O. Siar, S. Dancette, T. Dupuy, and D. Fabrègue, “Impact of liquid metal embrittlement inner cracks on the mechanical behavior of 3rd generation advanced high strength steel spot welds,” *Journal of Materials Research and Technology*, vol. 15, pp. 6678–6689, Nov. 2021, doi: 10.1016/j.jmrt.2021.11.100.

[53] J. Tian, W. Tao, and S. Yang, “Investigation on microhardness and fatigue life in spot welding of quenching and partitioning 1180 steel,” *Journal of Materials Research and Technology*, vol. 19, pp. 3145–3159, Jul. 2022, doi: 10.1016/j.jmrt.2022.06.083.

[54] W. Dong, M. Lei, H. Pan, K. Ding, and Y. Gao, “Role of the internal oxidation layer in the liquid metal embrittlement during the resistance spot welding of the Zn-coated advanced high strength steel,” *Journal of Materials Research and Technology*, vol. 21, pp. 3313–3326, Nov. 2022, doi: 10.1016/j.jmrt.2022.10.154.

[55] A. R. H. Midawi *et al.*, “A novel technique to measure the local mechanical properties of third generation advanced high strength steel resistance spot welds,” *Forces in Mechanics*, vol. 9, Dec. 2022, doi: 10.1016/j.finmec.2022.100150.

[56] P. Zhang, J. Xie, Y. X. Wang, and J. Q. Chen, “Effects of welding parameters on mechanical properties and microstructure of resistance spot welded DP600 joints,” *Science and Technology of Welding and Joining*, vol. 16, no. 7, pp. 567–574, Oct. 2011, doi: 10.1179/136217110X12813393169732.

[57] *Processes Description Resistance Spot Welder Resistance Spot Welding Handbook for Resistance Spot Welding*. [Online]. Available: www.MillerWelds.com

[58] L. Khan, M. L. Kunts, Y. Zhou, K. Chan, and N. Scotchmer, “Monitoring the Effect of RSW Pulsing on AHSS using FEA (SORPAS) Software.”

[59] I. A. Soomro, S. R. Pedapati, and M. Awang, “Optimization of postweld tempering pulse parameters for maximum load bearing and failure energy absorption in dual phase (DP590) steel resistance spot welds,” *Materials Science and Engineering: A*, vol. 803, Jan. 2021, doi: 10.1016/j.msea.2020.140713.

[60] S. Aslanlar, “The effect of nucleus size on mechanical properties in electrical resistance spot welding of sheets used in automotive industry,” *Mater Des*, vol. 27, no. 2, pp. 125–131, 2006, doi: 10.1016/j.matdes.2004.09.025.

[61] D. W. Zhao, Y. X. Wang, L. Zhang, and P. Zhang, “Effects of electrode force on microstructure and mechanical behavior of the resistance spot welded DP600 joint,” *Mater Des*, vol. 50, pp. 72–77, 2013, doi: 10.1016/j.matdes.2013.02.016.

[62] H. Cho, S. Nam, I. Hwang, J. H. Oh, M. Kang, and Y. M. Kim, “Fatigue behaviors of resistance spot welds for 980 MPa grade TRIP steel,” *Metals (Basel)*, vol. 9, no. 10, 2019, doi: 10.3390/met9101086.

[63] X. Wan, Y. Wang, and P. Zhang, “Effects of welding schedules on resistance spot welding of DP600 steel,” *ISIJ International*, vol. 54, no. 10, pp. 2375–2379, 2014, doi: 10.2355/isijinternational.54.2375.

[64] C. Ma, D. L. Chen, S. D. Bhole, G. Boudreau, A. Lee, and E. Biro, “Microstructure and fracture characteristics of spot-welded DP600 steel,” *Materials Science and Engineering: A*, vol. 485, no. 1–2, pp. 334–346, Jun. 2008, doi: 10.1016/j.msea.2007.08.010.

[65] U. Özsaraç, Y. S. Aslanlar, M. Kekik, Z. Barlas, S. Aslanlar, and H. Aslan, “Effect of Weld Nugget Diameter on Tensile-Shear Force in Resistance Spot Welded 1200M-DP800HF Joint.”

[66] M. Advanced, H. Strength, S. Resistance, and S. Welds, “The Role of HAZ Softening on Cross-Tension Mechanical Performance of The Role of HAZ Softening on Cross-Tension Mechanical Performance of Martensitic Advanced High Strength Steel Resistance Spot

Welds," *Metallurgical and Materials Transactions A*, no. January, 2021, doi: 10.1007/s11661-020-06104-5.

[67] T. Moolevliet *et al.*, "Performance of resistance spot-welded joints in advanced high-strength steel in static and dynamic tensile tests," *Welding in the world*, Jul. 2012.

[68] A. Chabok, E. van der Aa, and Y. Pei, "A study on the effect of chemical composition on the microstructural characteristics and mechanical performance of DP1000 resistance spot welds," *Materials Science and Engineering: A*, vol. 788, no. April, p. 139501, 2020, doi: 10.1016/j.msea.2020.139501.

[69] M. Tamizi, M. Pouranvari, and M. Movahedi, "The Role of HAZ Softening on Cross-Tension Mechanical Performance of Martensitic Advanced High Strength Steel Resistance Spot Welds," *Metall Mater Trans A Phys Metall Mater Sci*, vol. 52, no. 2, pp. 655–667, 2021, doi: 10.1007/s11661-020-06104-5.

[70] A. Ramazani, K. Mukherjee, A. Abdurakhmanov, M. Abbasi, and U. Prahl, "Characterization of Microstructure and Mechanical Properties of Resistance Spot Welded DP600 Steel," pp. 1704–1716, 2015, doi: 10.3390/met5031704.

[71] L. Prém, Á. Meilinger, S. A. Abd Al Al, and M. Gáspár, "Comparion of RSW technologies on DP steels with modified instrumented Charpy impact test," *Welding in the World*, vol. 67, no. 8, pp. 1911–1922, Aug. 2023, doi: 10.1007/s40194-023-01526-2.

[72] K. Zhou and L. Cai, "Online nugget diameter control system for resistance spot welding," *International Journal of Advanced Manufacturing Technology*, vol. 68, no. 9–12, pp. 2571–2588, Oct. 2013, doi: 10.1007/s00170-013-4886-0.

[73] B. han Ma, D. fang Ma, H. ran Wang, D. nian Chen, and F. hua Zhou, "Ballistic impact response of resistance-spot-welded (RSW) double-layered plates for Q&P980 steel," *Defence Technology*, vol. 18, no. 6, pp. 1052–1064, Jun. 2022, doi: 10.1016/j.dt.2021.04.010.

[74] P. Eftekharimilani, E. M. van der Aa, M. J. M. Hermans, and I. M. Richardson, "The microstructural evolution and elemental distribution of a 3rd generation 1 GPa advanced high strength steel during double pulse resistance spot welding," *Welding in the World*, vol. 61, no. 4, pp. 691–701, Jun. 2017, doi: 10.1007/s40194-017-0459-4.

[75] A. Chabok, H. Cao, E. van der Aa, and Y. Pei, "New insights into the fracture behavior of advanced high strength steel resistance spot welds," *J Mater Process Technol*, vol. 301, Mar. 2022, doi: 10.1016/j.jmatprotec.2021.117433.

[76] Y. ZHANG, C. FU, R. YI, and J. JU, "Optimization of double-pulse process in resistance spot welding of hot stamped steel sheet," *ISIJ International*, vol. 60, no. 6, pp. 1284–1290, Jun. 2020, doi: 10.2355/isijinternational.ISIJINT-2019-579.

[77] K. Zhou, W. Yu, G. Wang, and M. Ivanov, "Comparative analysis between multi-pulse and constant welding current for resistance spot welding process," *J Mater Sci*, vol. 58, no. 6, pp. 2853–2875, Feb. 2023, doi: 10.1007/s10853-023-08191-2.

[78] I. A. Soomro, S. R. Pedapati, and M. Awang, "Double pulse resistance spot welding of dual phase steel: Parametric study on microstructure, failure mode and low dynamic tensile shear properties," *Materials*, vol. 14, no. 4, pp. 1–19, 2021, doi: 10.3390/ma14040802.

[79] L. Prém, Z. Bézi, and A. Balogh, "Development of Resistant Spot Welding Technology for Automotive Ferrite-Martensitic Dual-Phase Steels with Joint Application of Finite Element Modelling and Experimental Research," *Adv Mat Res*, vol. 1138, pp. 43–48, Jul. 2016, doi: 10.4028/www.scientific.net/amr.1138.43.

[80] K. Májlinger, L. T. Katula, and B. Varbai, "Prediction of the Shear Tension Strength of Resistance Spot Welded Thin Steel Sheets from High- to Ultrahigh Strength Range," *Periodica Polytechnica Mechanical Engineering*, vol. 66, no. 1, pp. 67–82, 2022, doi: 10.3311/PPME.18934.

[81] S. alden Abd al al and Á. Meilinger, “Investigation of Resistance Spot Welded Joints Made on Ultra-high-Strength Steel Sheets,” in *Vehicle and Automotive Engineering* , vol. 4, 2023, pp. 981–994. doi: 10.1007/978-3-031-15211-5_82.

[82] M. Stadler, M. Gruber, R. Schnitzer, and C. Hofer, “Microstructural characterization of a double pulse resistance spot welded 1200 MPa TBF steel,” *Welding in the World*, vol. 64, no. 2, pp. 335–343, Feb. 2020, doi: 10.1007/s40194-019-00835-9.

[83] P. Eftekharimilani, E. M. van der Aa, M. J. M. Hermans, and I. M. Richardson, “Microstructural characterisation of double pulse resistance spot welded advanced high strength steel,” *Science and Technology of Welding and Joining*, vol. 22, no. 7, pp. 545–554, Oct. 2017, doi: 10.1080/13621718.2016.1274848.

[84] C. Ali, V. A. DER Ellen, D. HOSSON Jeff, and P. Yutao, “Microstructural Evolution and Mechanical Performance of Resistance Spot Welded DP1000 Steel With Single and Double Pulse Welding,” *Metal*, May 2017.

[85] C. Rajarajan, T. Sonar, P. Sivaraj, S. Raja, and N. Mathiazhagan, “The Effect of Resistance Spot Welding Parameters on Microstructure and Strength of DP800 Steel Joints Using Response Surface Methodology,” *Advances in Materials Science*, vol. 22, no. 3, pp. 53–78, 2022, doi: 10.2478/adms-2022-0013.

[86] S. Pawar, A. K. Singh, L. Kaushik, K. S. Park, J. H. Shim, and S. H. Choi, “Characterizing local distribution of microstructural features and its correlation with microhardness in resistance spot welded ultra-low-carbon steel: Experimental and finite element characterization,” *Mater Charact*, vol. 194, Dec. 2022, doi: 10.1016/j.matchar.2022.112382.

[87] “Pittner et al. - 2019 - Mechanical properties characterization of resistance spot welded DP1000 steel under uniaxial tensile tests”.

[88] A. A. Zisman, N. Y. Zolotorevsky, S. N. Petrov, and N. Y. Ermakova, “Effect of cooling rate on the bainite fraction in low carbon martensitic steel: combined analysis of transformation kinetics and crystal curvature,” *Letters on Materials*, vol. 13, no. 1, pp. 67–72, Mar. 2023, doi: 10.22226/2410-3535-2023-1-67-72.

[89] J. G. Speer, E. De Moor, K. O. Findley, D. K. Matlock, B. C. De Cooman, and D. V. Edmonds, “Analysis of microstructure evolution in quenching and partitioning automotive sheet steel,” in *Metallurgical and Materials Transactions A: Physical Metallurgy and Materials Science*, Dec. 2011, pp. 3591–3601. doi: 10.1007/s11661-011-0869-7.

[90] R. W. Rathbun, “Fatigue Behavior of Spot Welded High Strength Sheet Steels,” 2018.

[91] H. Rezayat, H. Ghassemi-Armaki, S. Sriram, and S. S. Babu, “Correlation of Local Constitutive Properties to Global Mechanical Performance of Advanced High-Strength Steel Spot Welds,” *Metallurgical and Materials Transactions A*, vol. 51, no. 5, pp. 2209–2221, May 2020, doi: 10.1007/s11661-020-05714-3.

[92] A. Chabok, E. van der Aa, I. Basu, J. De Hosson, and Y. Pei, “Effect of pulse scheme on the microstructural evolution, residual stress state and mechanical performance of resistance spot welded DP1000-GI steel,” *Science and Technology of Welding and Joining*, vol. 23, no. 8, pp. 649–658, 2018, doi: 10.1080/13621718.2018.1452875.

[93] S. M. Manladan, Y. J. Jang, and Y. Do Park, “Effect of paint baking on the halo ring and mechanical behavior of 30MnB5 hot-stamped steel resistance spot welding joints,” *Journal of Materials Research and Technology*, vol. 24, pp. 4756–4761, May 2023, doi: 10.1016/j.jmrt.2023.04.144.

[94] M. H. Amini-Chelak, R. Miresmaeili, M. Askari-Paykani, H. Aliyari, and H. R. Shahverdi, “Resistance spot weldability of Fe66Cr16.5Ni14.1Si3.4 advanced high strength steel using D-optimal design of experiment method,” *Journal of Materials Research and Technology*, vol. 25, pp. 5615–5632, Jul. 2023, doi: 10.1016/j.jmrt.2023.06.262.

[95] T. K. Pal and K. Chattopadhyay, “Resistance spot weldability and high cycle fatigue behaviour of martensitic (M190) steel sheet,” *Fatigue Fract Eng Mater Struct,* vol. 34, no. 1, pp. 46–52, Jan. 2011, doi: 10.1111/j.1460-2695.2010.01489.x.

[96] M. Eshraghi, M. A. Tschopp, M. Asle Zaeem, and S. D. Felicelli, “Effect of resistance spot welding parameters on weld pool properties in a DP600 dual-phase steel: A parametric study using thermomechanically-coupled finite element analysis,” *Mater Des,* vol. 56, pp. 387–397, 2014, doi: 10.1016/j.matdes.2013.11.026.

[97] A. Chabok, E. Galinmoghaddam, J. T. M. De Hosson, and Y. T. Pei, “Micromechanical evaluation of DP1000-GI dual-phase high-strength steel resistance spot weld,” *J Mater Sci,* vol. 54, no. 2, pp. 1703–1715, Jan. 2019, doi: 10.1007/s10853-018-2886-z.

[98] M. Pouranvari, S. Sobhani, and F. Goodarzi, “Resistance spot welding of MS1200 martensitic advanced high strength steel: Microstructure-properties relationship,” *J Manuf Process*, vol. 31, no. January, pp. 867–874, 2018, doi: 10.1016/j.jmapro.2018.01.009.

[99] H. Rezayat, H. Ghassemi-Armaki, and S. S. Babu, “Effects of Heat Affected Zone Softening Extent on the strength of Advanced High Strength Steels Resistance Spot Weld,” Sep. 07, 2018. doi: 10.31224/osf.io/e2679.

[100] M. Mansouri, H. Abadi, and M. Pouranvari, “Failure-Mode Transition in Resistance Spot welded DP780 Advanced High-Strength Steel: Effect of Loading Conditions,” *Materiali in tehnologije*, vol. 48, no. 1, pp. 67–71, Apr. 2014.

[101] S. Dancette, V. Massardier, J. Merlin, D. Fabrègue, and T. Dupuy, “Investigations on the mechanical behavior of advanced high strength steels resistance spot welds in cross tension and tensile shear,” in *Advanced Materials Research,* Trans Tech Publications Ltd, 2010, pp. 130–135. doi: 10.4028/www.scientific.net/AMR.89-91.130.

[102] A. Pasarkar, A. Mane, N. Singh, A. Datarkar, and N. Raut, “A Review of fatigue behaviour of resistance spot welds,” *Research on Engineering Structures and Materials,* vol. 9, no. 1, pp. 181–194, Feb. 2023, doi: 10.17515/resm2022.509me0824tn.

[103] Y. J. Chad, “Failure of Spot Weld: A Competition Between Crack Mechanics and Plastic Collapse,” 2002.

[104] “https://www.twi-global.com/technical-knowledge/published-papers/the-resistance-spot-welding-of-high-and-ultra-high-strength-steels-november-2004.”

[105] BY D. J. RADAKOVIC and M. TUMULURU, “An Evaluation of the Cross-Tension Test of Resistance Spot Welds in High-Strength Dual-Phase Steels,” *Welding,* vol. 91, Jan. 2012.

[106] Y. J. Chao, “Ultimate strength and failure mechanism of resistance spot weld subjected to tensile, shear, or combined tensile/shear loads,” *J Eng Mater Technol,* vol. 125, no. 2, pp. 125–132, 2003, doi: 10.1115/1.1555648.

[107] A. Ghatei-Kalashami, S. Zhang, M. Shojaee, A. R. H. Midawi, F. Goodwin, and N. Y. Zhou, “Failure behavior of resistance spot welded advanced high strength steel: The role of surface condition and initial microstructure,” *J Mater Process Technol*, vol. 299, Jan. 2022, doi: 10.1016/j.jmatprotec.2021.117370.

[108] Z. Xu, C. Tian, L. Mao, H. Tian, B. Yi, and H. Ling, “A mechanical properties and failure mechanism study for resistance spot welded AHSSs under coach-peel and lap-shear loads,” *Eng Fract Mech*, vol. 290, Sep. 2023, doi: 10.1016/j.engfracmech.2023.109474.

[109] M. Stadler, R. Schnitzer, M. Gruber, K. Steineder, and C. Hofer, “Influence of the cooling time on the microstructural evolution and mechanical performance of a double pulse resistance spot welded medium-mn steel,” *Metal,* vol. 11, no. 2, pp. 1–11, 2021, doi: 10.3390/met11020270.

[110] P. Stavropoulos and K. Sabatakakis, “Quality Assurance in Resistance Spot Welding: State of Practice, State of the Art, and Prospects,” Feb. 01, 2024, *Multidisciplinary Digital Publishing Institute (MDPI)*. doi: 10.3390/met14020185.

[111] C. Summerville, P. Compston, and M. Doolan, “A comparison of resistance spot weld quality assessment techniques,” in *Procedia Manufacturing,* Elsevier B.V., 2019, pp. 305–312. doi: 10.1016/j.promfg.2019.02.142.

[112] Manfred Stadler, Ronald Schnitzer, Martin Gruber, and Christina Hofer, “Improving the mechanical performance of a resistance spot welded 1200 MPa TBF steel,” *International Journal of Materials Research,* vol. 112, no. 4, pp. 262–270, 2021, doi: 10.1515/ijmr-2020-7962.

[113] G. H. Farrahi, A. Ahmadi, and K. Reza Kasyzadeh, “Simulation of vehicle body spot weld failures due to fatigue by considering road roughness and vehicle velocity,” *Simul Model Pract Theory,* vol. 105, Dec. 2020, doi: 10.1016/j.simpat.2020.102168.

[114] J. A. Davidson, “A Review of the Fatigue Properties of Spot-Welded Sheet Steels,” 1983. [Online]. Available: https://www.jstor.org/stable/44644352

[115] M. Pouranvari and S. P. H. Marashi, “Critical review of automotive steels spot welding: Process, structure and properties,” *Science and Technology of Welding and Joining,* vol. 18, no. 5, pp. 361–403, 2013, doi: 10.1179/1362171813Y.0000000120.

[116] K. TOHGO *et al.*, “Influence of Strength Level of Steels on Fatigue Strength and Fatigue Fracture Mechanism of Spot Welded Joints,” *Journal of the Society of Materials Science, Japan,* vol. 55, no. 12, pp. 1095–1101, Dec. 2006, doi: 10.2472/jsms.55.1095.

[117] J. J. F. Bonnen *et al.*, “Fatigue of Advanced High Strength Steel Spot-Welds,” 2006.

[118] T. K. Pal and K. Bhowmick, “Resistance spot welding characteristics and high cycle fatigue behavior of DP 780 steel sheet,” *J Mater Eng Perform,* vol. 21, no. 2, pp. 280–285, Feb. 2012, doi: 10.1007/s11665-011-9850-2.

[119] Y. Uematsu, N. Kawabe, Y. Okita, H. Matsuda, T. Kakiuchi, and T. Igarashi, “Fatigue Behavior of Resistance Spot Welded Steel Sheets Fabricated Using Electrodes with Different Tip Diameters,” *ISIJ International,* vol. 63, no. 1, pp. 135–142, 2023, doi: 10.2355/isijinternational.ISIJINT-2022-278.

[120] X. Long and S. K. Khanna, “Fatigue properties and failure characterization of spot welded high strength steel sheet,” *Int J Fatigue,* vol. 29, no. 5, pp. 879–886, May 2007, doi: 10.1016/j.ijfatigue.2006.08.003.

[121] J. H. Ordoñez Lara, R. R. Ambriz, C. García, G. Plascencia, and D. Jaramillo, “Fatigue Life of Resistance Spot Welding on Dual-Phase Steels,” in *Proceedings of the 17th International Conference on New Trends in Fatigue and Fracture,* Springer International Publishing, 2018, pp. 225–236. doi: 10.1007/978-3-319-70365-7_26.

[122] K. Yamazaki, K. Satoh, and Y. Tokunaga, “Static and Fatigue Strength of Spot Welded Joints of Ultrahigh Strength Steel Sheets.”

[123] H. Oikawa, G. Murayama, T. Sakiyama, Y. Takahashi, and T. Ishikawa, “Resistance Spot Weldability of High Strength Steel (HSS) Sheets for Automobiles,” 2007.

[124] L. Xie, B. Shi, Z. Xiao, J. Ren, and D. Li, “Fatigue characteristics of DP780 steel spot welding joints with different static fracture modes,” *Mater Trans,* vol. 62, no. 2, pp. 191–197, Feb. 2021, doi: 10.2320/matertrans.MT-M2020214.

[125] R. Mohan Iyengar *et al.*, “Influence of geometric parameters and their variability on fatigue resistance of spot-weld joints,” 2009.

[126] A. Arumugam and A. Pramanik, “Review of Experimental and Finite Element Analyses of Spot Weld Failures in Automotive Metal Joints,” 2020. [Online]. Available: https://www.researchgate.net/publication/344897181

[127] C. Author, M. Rahman, A. Rosli, M. Noor, M. Sani, and J. Julie, “Effects of Spot Diameter and Sheets Thickness on Fatigue Life of Spot Welded Structure based on FEA Approach,” *Am J Appl Sci,* vol. 6, no. 1, pp. 137–142, 2009.

[128] A. H. Ertas and F. O. Sonmez, “A parametric study on fatigue strength of spot-weld joints,” *Fatigue Fract Eng Mater Struct*, vol. 31, no. 9, pp. 766–776, 2008, doi: 10.1111/j.1460-2695.2008.01263.x.

[129] B. Pal, M. Amirthalingam, and S. G. S. Raman, “An Experimental Investigation on the High Cycle Fatigue Behavior of Resistance Spot Welded Ultrahigh Strength Steel,” *J Mater Eng Perform*, Dec. 2023, doi: 10.1007/s11665-023-08914-1.

[130] D. Frómeta *et al.*, “Fracture Resistance of Advanced High-Strength Steel Sheets for Automotive Applications,” *Metall Mater Trans A Phys Metall Mater Sci*, vol. 52, no. 2, pp. 840–856, Feb. 2021, doi: 10.1007/s11661-020-06119-y.

[131] P. Xu and T. Böllinghaus, “Fatigue Testing for Spot Welds - Problems, Solutions and New Development,” 2003. [Online]. Available: https://www.jstor.org/stable/44699615

[132] Z. Yu, N. Ma, H. Murakawa, G. Watanabe, M. Liu, and Y. Ma, “Prediction of the fatigue curve of high-strength steel resistance spot welding joints by finite element analysis and machine learning,” *International Journal of Advanced Manufacturing Technology*, vol. 128, no. 5–6, pp. 2763–2779, Sep. 2023, doi: 10.1007/s00170-023-11993-y.

[133] C. Wei and H. T. Kang, “Fatigue life prediction of spot-welded joints with a notch stress approach,” *Theoretical and Applied Fracture Mechanics*, vol. 106, Apr. 2020, doi: 10.1016/j.tafmec.2020.102491.

[134] T. ~ Resourcefor, J. M. Barsom, J. A. Davidson, and E. J. Imholf, “Fatigue Behavior of Spot Welds under Variable-Amplitude Loading,” *SAE International*, pp. 96–105, 1985.

[135] H. Z. B. Yan, SH. Lalam, S. Baczkowski, and T. Coon, “Spot Weld Fatigue of Dual Phase Steels,” *SAE International*, 2004.

[136] A. H. Ertas, O. Vardar, F. O. Sonmez, and Z. Solim, “Measurement and assessment of fatigue life of spot-weld joints,” *J Eng Mater Technol*, vol. 131, no. 1, pp. 1–11, 2009, doi: 10.1115/1.3030941.

[137] S. Parareda, D. Frómeta, D. Casellas, H. Sieurin, and A. Mateo, “Understanding the Fatigue Notch Sensitivity of High-Strength Steels through Fracture Toughness,” *Metals (Basel)*, vol. 13, no. 6, Jun. 2023, doi: 10.3390/met13061117.

[138] S. Donders, M. Brughmans, L. Hermans, and N. Tzannetakis, “The Effect of Spot Weld Failure on Dynamic Vehicle Performance.”

[139] I. A. Soomro, S. R. Pedapati, and M. Awang, “A review of advances in resistance spot welding of automotive sheet steels: emerging methods to improve joint mechanical performance,” *International Journal of Advanced Manufacturing Technology*, vol. 118, no. 5–6, pp. 1335–1366, 2022, doi: 10.1007/s00170-021-08002-5.

[140] Dong Ho Bae, Il Seon Sohn, and Jeong K Hong, “Assessing the effects of residual stresses on the fatigue strength of spot welds,” *Welding Journal*, Jan. 2003.

[141] L. Shi, J. Kang, M. Gesing, X. Chen, A. S. Haselhuhn, and B. E. Carlson, “Effect of notch root angle on fatigue behavior of aluminum to steel resistance spot welds,” *Int J Fatigue*, vol. 141, Dec. 2020, doi: 10.1016/j.ijfatigue.2020.105866.

[142] H. Zhi-Zhongt and C. Shu-Zhen, “Relationship Between Fatigue Notch Factor and Strength,” *Eng Fract Mech*, vol. 48, no. 1, pp. 127–136, 1994.

[143] A. H. Ertas and M. Akbulut, “Experimental study on fatigue performance of resistance spot-welded sheet metals”, doi: 10.1007/s00170-021-06822-z/Published.

[144] S. Zhang, “Fracture mechanics solutions to spot welds,” 2001.

[145] L. Brasileiro, Z. Sun, C. Mabru, R. Chieragatti, G. Proust, and D. Retraint, “Experimental study of a CoCrMo alloy treated by SMAT under rotating bending fatigue,” 2021, doi: 10.1016/j.prostr.2022.03.029ï.

[146] Y. L. Lee and J. Pan, *Fatigue Testing and Analysis (Theory and Practice)*, vol. 106. Elsevier, 2005.

[147] Haidar Mobark, “Fatigue Strength and Fatigue Crack Propagation Design Curves for High Strength Steel Structural Elements,” University of Miskolc, Miskolc, 2020.

[148] H. Nakayasu and S. Kodama, “‘Statistical S–N Testing Method With 14 Specimens: JSME Standard Method for Determination of S–N Curves,’ in Statistical Research on Fatigue and Fracture,” *Elsevier Applied Science* , pp. 59–69, 1987.

[149] János Lukács, Török Imre, and A. Balogh, “Weldability and the Properties of Welded Joints,” *University of Miskolc, Miskolc*, 2015.

[150] K. W. Miller, Y. J. Chao, A. Martinez, X. Zhu, S. Liu, and P. C. Wang, “Quasi-Static and Impact Strength of Fatigue Damaged Spot Welds,” 2003.

[151] K.-M. W. Ewing, M. Cheresh, R. Thompson, and P. Kukuchek, “Static and Impact Strengths of Spot-Welded HSLA and Low Carbon Steel Joints,” 2018.

[152] R. S. Birch and M. Alves, “Dynamic failure of structural joint systems,” *Thin-Walled Structures*, vol. 36, no. 2, pp. 137–154, Feb. 2000, doi: 10.1016/S0263-8231(99)00040-3.

[153] S.-H. Lin, J. Pan, S. Wu, and T. Tyan, “Failure loads of spot weld specimens under impact opening and shear loading conditions,” *Exp Mech*, vol. 44, no. 2, pp. 147–157, Apr. 2004, doi: 10.1007/BF02428174.

[154] M. I. Khan, M. L. Kuntz, and Y. Zhou, “Effects of weld microstructure on static and impact performance of resistance spot welded joints in advanced high strength steels,” *Science and Technology of Welding and Joining*, vol. 13, no. 3, pp. 294–304, May 2008, doi: 10.1179/174329308X271733.

[155] Y. Xia, Q. Zhou, P. C. Wang, N. L. Johnson, X. Q. Gayden, and J. D. Fickes, “Development of a high-efficiency modeling technique for weld-bonded steel joints in vehicle structures, Part II: Dynamic experiments and simulations,” *Int J Adhes Adhes*, vol. 29, no. 4, pp. 427–433, Jun. 2009, doi: 10.1016/j.ijadhadh.2008.09.007.

[156] J. H. Song, J. W. Ha, H. Huh, J. H. Lim, and S. H. Park, “Dynamic Failure of A Spot Weld in Lap-Shear Tests Under Combined Loading Conditions,” *Int J Mod Phys B*, vol. 22, pp. 5527–5532, 2008, [Online]. Available: www.worldscientific.com

[157] J. H. Song, H. Huh, J. H. Lim, and S. H. Park, “Effect of Tensile Speed on The Failure Load of a Spot Weld Under Combined Loading Conditions,” *Int J Mod Phys B*, vol. 22, no. 09n11, pp. 1469–1474, Apr. 2008, doi: 10.1142/S0217979208046943.

[158] E. Bayraktar, D. Kaplan, F. Schmidt, H. Paqueton, and M. Grumbach, “State of art of impact tensile test (ITT): Its historical development as a simulated crash test of industrial materials and presentation of new ‘ductile/brittle’ transition diagrams,” *J Mater Process Technol*, vol. 204, no. 1–3, pp. 313–326, Aug. 2008, doi: 10.1016/j.jmatprotec.2007.11.044.

[159] R. Muscat and M. Mahfouf, “Predicting Charpy Impact Energy for Heat-Treated Steel using a Quantum-Membership-Function-based Fuzzy Model,” *IFAC-PapersOnLine*, vol. 49, no. 20, pp. 138–142, 2016, doi: 10.1016/j.ifacol.2016.10.110.

[160] M. Grumbach and G. Sanz, “Ductile–brittle tests by impact tensile test (ITT),” *J. Metall*, vol. 2, pp. 145–164, 1972.

[161] E. Bayraktara, D. Kaplan, C. Buirette, and M. Grumbach, “Application of impact tensile testing to welded thin sheets,” *Journal of Materials Processing Technology* , vol. 145, pp. 27–39, 2004.

[162] E. Bayraktar, J. Chevalier, F. Bonnet, D. Kaplan, and J. Claeys, “Impact tensile test: A new type of crash test for welded joints used in automotive applications,” EDP Sciences, 2009, pp. 235–241. doi: 10.1051/dymat/2009032.

[163] E. Bayraktar, D. Kaplan, and M. Grumbach, “Application of impact tensile testing to spot welded sheets,” *J Mater Process Technol*, vol. 153–154, pp. 80–86, Nov. 2004, doi: 10.1016/j.jmatprotec.2004.04.020.

[164] C. Jurewicz, A. Sobhani, J. Woolley, J. Dutschke, and B. Corben, “Exploration of Vehicle Impact Speed – Injury Severity Relationships for Application in Safer Road Design,” *Transportation Research Procedia,* vol. 14, pp. 4247–4256, 2016, doi: 10.1016/j.trpro.2016.05.396.

[165] Y. J. Chao, K. Wang, K. W. Miller, and X.-K. Zhu, “Dynamic Separation of Resistance Spot Welded Joints,” *Exp Mech,* vol. 50, no. 7, pp. 889–900, Sep. 2010, doi: 10.1007/s11340-009-9276-z.

[166] W. Noh, Y. Koh, K. Chung, J. H. Song, and M. G. Lee, “Influence of dynamic loading on failure behavior of spot welded automotive steel sheets,” *Int J Mech Sci,* vol. 144, pp. 407–426, Aug. 2018, doi: 10.1016/j.ijmecsci.2018.06.009.

[167] B. Langrand and E. Markiewicz, “Strain-rate dependence in spot welds: Non-linear behaviour and failure in pure and combined modes I/II,” *Int J Impact Eng,* vol. 37, no. 7, pp. 792–805, 2010, doi: 10.1016/j.ijimpeng.2010.01.004.

[168] M. Ali, D. Porter, J. Kömi, M. Eissa, H. El Faramawy, and T. Mattar, “Effect of cooling rate and composition on microstructure and mechanical properties of ultrahigh-strength steels,” *Journal of Iron and Steel Research International,* vol. 26, no. 12, pp. 1350–1365, Dec. 2019, doi: 10.1007/s42243-019-00276-0.

[169] M. Piott, A. Werber, L. Schleuss, N. Doynov, R. Ossenbrink, and V. G. Michailov, “A study of the heat transfer mechanism in resistance spot welding of aluminum alloys AA5182 and AA6014,” *International Journal of Advanced Manufacturing Technology,* vol. 111, no. 1–2, pp. 263–271, Nov. 2020, doi: 10.1007/s00170-020-05650-x.

[170] H. M. Mallaradhya, M. Vijay Kumar, R. Ranganatha, S. Darshan, and Lochan, “Resistance spot welding: A review,” Apr. 30, 2018, *Transstellar Journal Publications and Research Consultancy Private Limited (TJPRC).* doi: 10.24247/ijmperdapr201846.

[171] M. Kuo and J. Chiang, “Weldability Study of Resistance Spot Welds and Minimum Weld Button Size Methodology Development for DP Steel Ford Truck Frame Design & Release Reprinted From: Innovations in Steel Sheet and Bar Products and Processing, and Modeling and Testing of Steel Structures,” 2018.

[172] K. Prabitz *et al.*, “Validated multi-physical finite element modelling of the spot welding process of the advanced high strength steel dp1200hd,” *Materials,* vol. 14, no. 18, 2021, doi: 10.3390/ma14185411.

[173] S. Ren, W. Huang, N. Ma, G. Watanabe, Z. Zhang, and W. Deng, “Numerical modeling from process to residual stress induced in resistance spot welding of DP980 steel,” *International Journal of Advanced Manufacturing Technology,* vol. 125, no. 7–8, pp. 3563–3576, Apr. 2023, doi: 10.1007/s00170-023-10845-z.

[174] Jerry Gould, S.P. Khurana, and T. Li, “Predictions of microstructures when welding automotive advanced high-strength steels,” *Weld J,* vol. 85, pp. 111–116, 2006.

[175] Song, “General rights Testing and Modeling of Contact Problems in Resistance Welding.” [Online]. Available: http://www.ipl.dtu.dk/publikation/7793/dk/

[176] H. M. E. Ramos, S. M. O. Tavares, and P. M. S. T. de Castro, “Numerical modelling of welded T-joint configurations using SYSWELD,” *Science and Technology of Materials,* vol. 30, pp. 6–15, Dec. 2018, doi: 10.1016/j.stmat.2018.08.002.

[177] T. Dupuy and -Chainarong Srikunwong, “Resistance Welding Numerical Simulation A Promising Technique,” 2004.

[178] “SYSWELD Engineering Simulation Solution for Heat Treatment, Welding and Welding Assembly.” [Online]. Available: www.Iran-mavad.com

[179] D. Löveborn, “3D FE Simulations of Resistance Spot Welding SCHOOL OF ENGINEERING SCIENCES.” [Online]. Available: www.swereakimab.se

[180] E. Feulvarch, V. Robin, and J. M. Bergheau, “Resistance spot welding simulation: A general finite element formulation of electrothermal contact conditions,” *J Mater Process*

Technol, vol. 153–154, no. 1–3, pp. 436–441, Nov. 2004, doi: 10.1016/j.jmatprotec.2004.04.096.

[181] P. ; Govindan and S. Sankar, "Modeling of resistance spot welding process-a review," *BEST : International Journal of Management, Information Technology and Engineering*, vol. 1, no. 3, pp. 67–78, 2013.

[182] Z. Mikno, S. Kowieski, and W. Zhang, "Simulation and optimisation of resistance welding using the SORPAS® software programme," *Biuletyn Instytutu Spawalnictwa*, no. 4, 2016, doi: 10.17729/ebis.2016.4/2.

[183] "Hamedi, Pashazadeh - 2008 - Numerical study of nugget formation in resistance spot welding".

[184] V. Javaheri, A. Pohjonen, J. I. Asperheim, D. Ivanov, and D. Porter, "Physically based modeling, characterization and design of an induction hardening process for a new slurry pipeline steel," *Mater Des*, vol. 182, Nov. 2019, doi: 10.1016/j.matdes.2019.108047.

[185] Z. Han, J. Orozco, J. E. Indacochea, and C. H. Chen, "Resistance spot welding: a heat transfer study," *Welding Journal (Miami, Fla)*, vol. 68, no. 9, 1989.

[186] S. Beguš, J. Bojkovski, J. Drnovšek, and G. Geršak, "Magnetic effects on thermocouples," *Meas Sci Technol*, vol. 25, no. 3, 2014, doi: 10.1088/0957-0233/25/3/035006.

[187] *A reference for analog & digital signal conditioners & Pc-based data acquisition systems*. Measurement Computing Corporation, 2004.

[188] J. Stephen, "Spot Weld Examination using NDE Methods," 2019. [Online]. Available: http://www.ndt.net/?id=25726

[189] D. Ibáñez, E. García, J. Martos, and J. Soret, "Real-time electrode misalignment detection device for RSW basing on magnetic fields," in *ICINCO 2020 - Proceedings of the 17th International Conference on Informatics in Control, Automation and Robotics*, SciTePress, 2020, pp. 142–149. doi: 10.5220/0009820801420149.

[190] D. Ibáñez, E. García, J. Soret, and J. Martos, "Real-Time Condition Monitoring System for Electrode Alignment in Resistance Welding Electrodes," *Sensors*, vol. 22, no. 21, Nov. 2022, doi: 10.3390/s22218412.

[191] F. F. Reis, V. Furlanetto, and G. F. Batalha, "Resistance Spot weld in Vehicle Structures Using Dynamic Resistance Adaptive Control," in *SAE Technical Papers*, SAE International, Oct. 2016. doi: 10.4271/2016-36-0303.

[192] C. Mathiszik, J. Koal, J. Zschetzsche, U. Füssel, and H. C. Schmale, "Study on precise weld diameter validations by comparing destructive testing methods in resistance spot welding," *Welding in the World*, vol. 68, no. 7, pp. 1825–1835, Jul. 2024, doi: 10.1007/s40194-024-01747-z.

[193] P. S. Wei and T. H. Wu, "Numerical study of electrode geometry effects on resistance spot welding," *Science and Technology of Welding and Joining*, vol. 18, no. 8, pp. 661–670, Nov. 2013, doi: 10.1179/174329313X13759662488396.

[194] M. Zhou, S. J. Hu, and H. Zhang, "Critical specimen sizes for tensile-shear testing of steel sheets," *Weld J*, vol. 78, no. 9, 1999.

[195] N. Den Uijl and S. Smith, "The Influence of Electrode Geometry on Resistance Spot Welding of Advanced High Strength Steels for Automotive Applications," 2007. [Online]. Available: https://www.researchgate.net/publication/303259957

[196] I. K. Al Naimi, M. H. Al Saadi, K. M. Daws, and N. Bay, "Influence of surface pretreatment in resistance spot welding of aluminum AA1050," *Prod Manuf Res*, vol. 3, no. 1, pp. 185–200, Jan. 2015, doi: 10.1080/21693277.2015.1030795.

[197] H. Jo, D. Kim, M. Kang, J. Park, and Y. M. Kim, "Effects of surface roughness and force of electrode on resistance spot weldability of aluminum 6061 alloy," *Applied Sciences (Switzerland)*, vol. 9, no. 19, Oct. 2019, doi: 10.3390/app9193958.

[198] H. Moshayedi and I. Sattari-Far, “Resistance spot welding and the effects of welding time and current on residual stresses,” *J Mater Process Technol*, vol. 214, no. 11, pp. 2545–2552, 2014, doi: 10.1016/j.jmatprotec.2014.05.008.

[199] “Specimen dimensions and procedure for cross tension testing resistance spot and embossed projection welds.”

[200] M. Pouranvari and S. P. H. Marashi, “Critical sheet thickness for weld nugget growth during resistance spot welding of three-steel sheets,” *Science and Technology of Welding and Joining*, vol. 16, no. 2, pp. 162–165, Feb. 2011, doi: 10.1179/1362171810Y.0000000016.

[201] X. Liu, Y. Wei, H. Wu, and T. Zhang, “Factor analysis of deformation in resistance spot welding of complex steel sheets based on reverse engineering technology and direct finite element analysis,” *J Manuf Process*, vol. 57, pp. 72–90, Sep. 2020, doi: 10.1016/j.jmapro.2020.06.028.

[202] J. Kim, J. Park, S. Jeong, and B. Seo, “Evaluation of Welding Quality using Servo-Gun Displacement Data for Field Spot Welding,” *Journal of Welding and Joining*, vol. 38, no. 5, pp. 460–468, Oct. 2020, doi: 10.5781/jwj.2020.38.5.5.

[203] J. Hlavacek, M. Knenicky, and K. Draxler, “Calibration of unipolar high current impulses for resistance spot welding,” in *Proceedings - 2020 21st International Scientific Conference on Electric Power Engineering, EPE 2020*, Institute of Electrical and Electronics Engineers Inc., Oct. 2020. doi: 10.1109/EPE51172.2020.9269221.

[204] ENTRON Controls, *Resistance Welding Controls and Applications*. 2014. [Online]. Available: www.entroncontrols.com

[205] J. Dong, J. Hu, and Z. Luo, “Quality Monitoring of Resistance Spot Welding Based on a Digital Twin,” *Metals (Basel)*, vol. 13, no. 4, Apr. 2023, doi: 10.3390/met13040697.

[206] D. Zhao, N. Vdonin, M. Slobodyan, S. Butsykin, A. Kiselev, and A. Gordynets, “Assessing Electrode Characteristics in Continuous Resistance Spot Welding of BH 340 Steel Based on Dynamic Resistance,” *Journal of Manufacturing and Materials Processing*, vol. 7, no. 6, Dec. 2023, doi: 10.3390/jmmp7060218.

[207] M. Hamedi and H. Eisazadeh, “Numerical Simulation of Nugget Geometry and Temperature Distribution in Resistance Spot Welding,” 2015.

[208] L. Hassan and H. Lafta, “The Effect of Electrode Geometry and Pre-heating Treatment on Resistance Spot Welding Strength,” *Engineering and Technology Journal*, vol. 41, no. 7, pp. 1–9, Jul. 2023, doi: 10.30684/etj.2023.138070.1371.

[209] A. S. Kiselev and M. S. Slobodyan, “Effects of electrode degradation on properties of small-scale resistance spot welded joints of e110 alloy,” *Materials Science Forum*, vol. 970, pp. 227–235, 2019, doi: 10.4028/www.scientific.net/MSF.970.227.

[210] E. Zh. Akbolatov, A. S. Kiselev, and M. S. Slobodyan, “Prediction and stabilization of initial resistance between electrodes for small-scale resistance spot welding,” *Welding in the World*, vol. 63, no. 2, pp. 443–457, Mar. 2019, doi: 10.1007/s40194-018-0671-x.

[211] M. Gáspár, Á. Dobosy, M. Tisza, I. Török, Y. Dong, and K. Zheng, “Improving the properties of AA7075 resistance spot-welded joints by chemical oxide removal and post weld heat treating,” *Welding in the World*, vol. 64, no. 12, pp. 2119–2128, Dec. 2020, doi: 10.1007/s40194-020-00988-y.

[212] S. Keeler, M. Kimchi, and P. J. Mooney, “Advanced High-Strength Steels Guidelines Version 6.0,” *WorldAutoSteel*, no. September, p. 314, 2017, [Online]. Available: https://www.worldautosteel.org/projects/advanced-high-strength-steel-application-guidelines/

[213] H. T. Kang, A. Khosrovaneh, H. Hu, and U. De Souza, “A fatigue prediction method for spot welded joints,” in *SAE Technical Papers*, SAE International, 2013. doi: 10.4271/2013-01-1208.

[214] “Test Methods for Notched Bar Impact Testing of Metallic Materials,” Jun. 01, 2018, *ASTM International, West Conshohocken, PA*. doi: 10.1520/E0023-18.

[215] M. B. Ali, S. Abdullah, M. Z. Nuawi, and A. K. Ariffin, “Investigation of energy absorbed from an instrumented charpy impact on automotive specimens,” in *Applied Mechanics and Materials*, 2012, pp. 182–186. doi: 10.4028/www.scientific.net/AMM.165.182.

[216] C. N. McCowan, E. Lucon, and R. L. Santoyo, “Evaluation of Bias for Two Charpy Impact Machines with the Same Instrumented Striker,” *J ASTM Int*, vol. 8, no. 5, pp. 1–11, May 2011, doi: 10.1520/JAI103239.

[217] M. I. Khan, M. L. Kuntz, E. Biro, and Y. Zhou, “Microstructure and Mechanical Properties of Resistance Spot Welded Advanced High Strength Steels,” vol. 49, no. 7, pp. 1629–1637, 2008, doi: 10.2320/matertrans.MRA2008031.

[218] B. V. H. Hernandez, M. L. Kuntz, M. I. Khan, and Y. Zhou, “Influence of microstructure and weld size on the mechanical behaviour of dissimilar AHSS resistance spot welds,” *Science and Technology of Welding and Joining*, vol. 13, no. 8, pp. 769–776, Nov. 2008, doi: 10.1179/136217108X325470.

[219] M. Pouranvari, H. R. Asgari, S. M. Mosavizadch, P. H. Marashi, and M. Goodarzi, “Effect of weld nugget size on overload failure mode of resistance spot welds,” *Science and Technology of Welding and Joining*, vol. 12, no. 3, pp. 217–225, 2007, doi: 10.1179/174329307X164409.

[220] Prém L. and Balogh A., “Investigation of dynamic behaviour of resistance spot welded joints in ferrite-martensitic DP steels with a newly developed dynamic testing equipment,” *GÉP*, vol. 71, pp. 75–79, 2020.

[221] American Welding Society (AWS) D8 Committee on Automatic Welding, *Specification for Automotive Weld Quality-Resistance Spot Welding of Steel*. 2021.

[222] M. Brožek, “Resistance Spot Welding of Steel Sheets of Different Thickness,” in *in Proc. Engineering for Rural Development*, Jelgava, Latvia, May 2015, pp. 72–77.

[223] M. Tamizi, M. Pouranvari, and M. Movahedi, “Welding metallurgy of martensitic advanced high strength steels during resistance spot welding,” *Science and Technology of Welding and Joining*, vol. 22, no. 4, pp. 327–335, 2017, doi: 10.1080/13621718.2016.1240979.

[224] D. M. Field, K. R. Limmer, and B. C. Hornbuckle, “On the grain growth kinetics of a low density steel,” *Metals (Basel)*, vol. 9, no. 9, Sep. 2019, doi: 10.3390/met9090997.

[225] D. Zhao, Y. Wang, P. Zhang, and D. Liang, “Modeling and Experimental Research on Resistance Spot Welded Joints for Dual-Phase Steel,” *Materials*, vol. 12, no. 7, p. 1108, Apr. 2019, doi: 10.3390/ma12071108.

[226] A. J. DeArdo, C. I. Garcia, K. Cho, and M. Hua, “New method of characterizing and quantifying complex microstructures in steels,” Jan. 2010. doi: 10.1080/10426910903143415.

[227] J. WU, P. J. WRAY, C. I. GARCIA, M. HUA, and A. J. DEARDO, “Image Quality Analysis: A New Method of Characterizing Microstructures,” *ISIJ International*, vol. 45, no. 2, pp. 254–262, 2005, doi: 10.2355/isijinternational.45.254.

[228] M. Erdogan, “Effect of austenite dispersion on phase transformation in dual phase steel.” [Online]. Available: www.actamat-journals.com

[229] V. Javaheri, S. Pallaspuro, A. Kaijalainen, S. Sadeghpour, J. Kömi, and D. Porter, “Promising bending properties of a new as-rolled medium-carbon steel achieved with furnace-cooled bainitic microstructures,” *Materials Science and Engineering: A*, vol. 796, Oct. 2020, doi: 10.1016/j.msea.2020.140011.

[230] H. Tervo *et al.*, “Characterization of coarse-grained heat-affected zones in al and ti-deoxidized offshore steels,” *Metals (Basel)*, vol. 10, no. 8, pp. 1–18, Aug. 2020, doi: 10.3390/met10081096.

[231] S. I. Wright and M. M. Nowell, “EBSD image quality mapping,” *Microscopy and Microanalysis*, vol. 12, no. 1, pp. 72–84, Feb. 2006, doi: 10.1017/S1431927606060090.

[232] X. Tao and A. Eades, “Alternatives to Image Quality (IQ) Mapping in EBSD,” *Microscopy and Microanalysis*, vol. 8, no. S02, pp. 692–693, Aug. 2002, doi: 10.1017/S1431927602106465.

[233] S. Afkhami *et al.*, “Thermomechanical simulation of the heat-affected zones in welded ultra-high strength steels: Microstructure and mechanical properties,” *Mater Des*, vol. 213, p. 110336, 2022, doi: 10.1016/j.matdes.2021.110336.

[234] A. Mehta *et al.*, “Additive manufacturing and mechanical properties of the dense and crack free Zr-modified aluminum alloy 6061 fabricated by the laser-powder bed fusion,” *Addit Manuf*, vol. 41, May 2021, doi: 10.1016/j.addma.2021.101966.

LIST OF PUBLICATIONS RELATED TO THE TOPIC OF THE RESEARCH FIELD

IN ENGLISH

(1) S. Alden Abd Al Al, M. Gáspár, and Á. Meilinger, “Properties of Hybrid Aluminium-Steel Joints Made by Resistance Spot Welding,” Defect and Diffusion Forum, vol. 416. Trans Tech Publications, Ltd., pp. 131–138, May 27, 2022. doi: 10.4028/p-3099yq.

(2) S. alden Abd al al and Á. Meilinger, “Investigation of Resistance Spot Welded Joints Made on Ultra-high-Strength Steel Sheets,” Lecture Notes in Mechanical Engineering. Springer International Publishing, pp. 981–994, Sep. 10, 2022. doi: 10.1007/978-3-031-15211-5_82.

(3) S. alden Abd al al and Á. Meilinger, "Development of resistance spot welding technology on ultra-high strength steel sheets: Ellenállás-ponthegesztési technológia fejlesztése ultra-nagyszilárdságú acélokhoz," in XXXI. Nemzetközi Hegesztési Konferencia, J. Gáti, Ed. Budapest, Hungary: Hungarian Welding Association, 2022, pp. 113–123.

(4) S. Alden Abd al al, M. Fodorné Cserépi, M. Gáspár, and Á. Meilinger, “Optimizing Sample Preparation for Destructive Testing in Resistance Spot Welding,” Journal of Physics: Conference Series, vol. 2848, no. 1. IOP Publishing, p. 012005, Sep. 01, 2024. doi: 10.1088/1742-6596/2848/1/012005.

(5) S. Alden. Abd Al Al, Á. Meilinger, M. Gáspár, and J. Lukács, “High Cycle Fatigue Testing of Lap Shear RSW Joints from Martensitic MS1400 Steel Sheets,” Materials Science Forum, vol. 1095. Trans Tech Publications, Ltd., pp. 139–151, Aug. 18, 2023. doi: 10.4028/p-o9mwsq.

(6) S. Alden Abd Al Al, Á. Meilinger, and M. Gáspár, “Physical Heat Cycle Measurement of Resistance Spot Welding,” Key Engineering Materials, vol. 989. Trans Tech Publications, Ltd., pp. 65–75, Oct. 28, 2024. doi: 10.4028/p-tb0owj.

(7) Á. Meilinger, L. Prém, S. A. Abd Al Al, and M. Gáspár, “Comparison of RSW technologies on DP steels with modified instrumented Charpy impact test,” Welding in the World, vol. 67, no. 8. Springer Science and Business Media LLC, pp. 1911–1922, Apr. 24, 2023. doi: 10.1007/s40194-023-01526-2.

(8) S. Alden Abd Al Al and M. Gáspár, "The impact of geometrical deviation on specimen testing for MS1400 martensitic steel in RSW," in XXXII. Nemzetközi Hegesztési Konferencia: Konferencia Kiadvány, J. Gáti and M. Gáspár, Eds., 2024, pp. 67–87.

(9) S. Alden Abd Al Al, C. M. Fodorné, M. Gáspár, and Á. Meilinger, "Resistance spot welding and dissimilar joining of automotive high-strength steels and aluminium alloys," GÉP, vol. 74, no. 4, pp. 73–76, 2023.

(10) S. alden Abd al al and Á. Meilinger, "Thermal Simulation of Resistance Spot Welding in Case of DP600 Steel," in Kutatási eredmények a Miskolci Egyetem Gépészmérnöki és Informatikai Karának Anyagszerkezettani és Anyagtechnológiai Intézetében, J. Kovács and

J. Lukács, Eds. Miskolc, Hungary: Miskolci Egyetem, Gépészmérnöki és Informatikai Kar, Anyagszerkezettani és Anyagtechnológiai Intézet, 2024, pp. 131–142.

(11) N. Tanuj, R. P. S. Sisodia, and S. alden Abd al al, "Experimental investigation of CMT welding parameters for DP1000 butt joints," Diáktudomány: A Miskolci Egyetem Tudományos Diákköri Munkáiból, vol. 17, pp. 79–87, 2024.

(12) M. Alhafadhi, M. Alsigar, Z. A. Oudah, Z. Bézi, S. alden Abd al al, and P. R. Reddy, "Influence of heat input and preheating on residual stresses in pipe weld," Pollack Periodica: An International Journal for Engineering and Information Sciences, vol. 19, no. 2, pp. 42–47, 2024.

IN HUNGARIAN

(13) M. Gáspár, S. alden Abd al al, and L. Gyura, "Lángegyengetési hőciklusok hatása az S1100M acél tulajdonságaira," in Kutatási eredmények a Miskolci Egyetem Gépészmérnöki és Informatikai Karának Anyagszerkezettani és Anyagtechnológiai Intézetében, J. Kovács and J. Lukács, Eds. Miskolc, Hungary: Miskolci Egyetem, Gépészmérnöki és Informatikai Kar, Anyagszerkezettani és Anyagtechnológiai Intézet, 2024, pp. 119–130.

(14) S. alden Abd al al and Á. Meilinger, "Hegesztési hőciklusok mérése különböző ellenállás-ponthegesztési technológiák esetén," in Kutatási eredmények a Miskolci Egyetem Gépészmérnöki és Informatikai Karának Anyagszerkezettani és Anyagtechnológiai Intézetében, Zs. Koncsik and J. Lukács, Eds. Miskolc, Hungary: Miskolci Egyetem, Gépészmérnöki és Informatikai Kar, Anyagszerkezettani és Anyagtechnológiai Intézet, 2023, pp. 95–106.

(15) S. Alden Abd Al Al. and Á. Meilinger, "Az impulzustechnika hatása az MS1400 alapanyagon végzett ellenállás-ponthegesztett kötések szövetszerkezetére," in Kutatási eredmények a Miskolci Egyetem Gépészmérnöki és Informatikai Karának Anyagszerkezettani és Anyagtechnológiai Intézetében, J. Kovács and J. Lukács, Eds. Miskolc, Hungary: Miskolci Egyetem, Gépészmérnöki és Informatikai Kar, Anyagszerkezettani és Anyagtechnológiai Intézet, 2024, pp. 85–94.

(16) S. Alden Abd Al Al, Á. Meilinger, M. Gáspár, and J. Lukács, "Martenzites és kettős-fázisú acéllemezek ellenállás-ponthegesztett kötéseinek nagyciklusú fárasztóvizsgálatai," in Kutatási eredmények a Miskolci Egyetem Gépészmérnöki és Informatikai Karának Anyagszerkezettani és Anyagtechnológiai Intézetében, J. Kovács and J. Lukács, Eds., Miskolc, Hungary: Miskolci Egyetem, Gépészmérnöki és Informatikai Kar, Anyagszerkezettani és Anyagtechnológiai Intézet, 2024, pp. 107–118.

(17) Á. Meilinger and S. alden Abd al al, "Ellenállás-ponthegesztési technológia fejlesztése ultra-nagyszilárdságú acélokhoz," Hegesztéstechnika, vol. 35, no. 1, pp. 35–41, 2024.

PRESENTATIONS

(18) Á. Meilinger, S. alden Abd al al , P. Kovács, J. Lukács, and M. Fodorné Cserépi, "The behavior of RSW and clinched joints from similar and dissimilar automotive materials under different loading conditions," Paper: III-2114-23, 2023.

APPENDICES

A1	Geometrical deviation and sample preparation for RSW
A2	RSW welding parameter optimisation for AHSS
A3	HCF test results of DP and MS steels
A4	Instrumented impact test of DP steel
A5	Thermocouple placement for HCM in HAZ subzones
A6	Welding procedure specification (WPS)

Note on Appendices

The appendices related to this dissertation are available for download and review through the following link:

https://drive.google.com/file/d/1AMycOZ5IhK3WSmeZFvo8aym3vfsl3N_d/view?usp=sharing

These supplementary materials include detailed data, figures, experimental results, and additional documentation referenced in the main body of the dissertation.